2011-06-14

Experimental Characterization of Baffle Plate Influence on Turbulent and Cavitation Induced Vibrations in Pipe Flow

Gavin J. Holt
Brigham Young University - Provo

Experimental Characterization of Baffle Plate Influence on Turbulent and Cavitation Induced Vibrations in Pipe Flow

Gavin J. Holt

A thesis submitted to the faculty of
Brigham Young University
in partial fulfillment of the requirements for the degree of

Master of Science

R. Daniel Maynes, Chair
Jonathan D. Blotter
Steven L. Gorrell

Department of Mechanical Engineering

Brigham Young University

June 2011

ABSTRACT

Experimental Characterization of Baffle Plate Influence
on Turbulent and Cavitation Induced
Vibrations in Pipe Flow

Gavin J. Holt
Department of Mechanical Engineering
Master of Science

Turbulent and cavitation induced pipe vibration is a large problem in industry often resulting in pipe failures. This thesis provides an experimental investigation on turbulent flow and cavitation induced pipe vibration caused by sharp edged baffle plates. Due to large pressure losses across a baffle plate, cavitation can result. Cavitation can be destructive to pipe flow in the form of induced pipe wall vibration and cavitation inception. Incipient and critical cavitation numbers are design points that are often used in designing baffle plate type geometries. This investigation presents how these design limits vary with the influencing parameters by exploring a range of different baffle plate geometries. The baffle plates explored contained varying hole sizes that ranged from 0.159 cm to 2.54 cm, with the total through area, or openness, of each baffle plate ranging between 11% and 60%. Plate thickness varied from 0.32-0.635 cm. Reynolds numbers ranged from 5×10^4-85×10^4.

The results show that the cavitation design limits are function of size scale effects and the loss coefficient only. The results also show that the loss coefficient for a baffle plate varies not only with total through area ratio, but also due with the plate thickness to baffle hole diameter ratio. Pipe wall vibrations were shown to decrease with increased through area ratio and increased thickness to diameter ratios.

An investigation was also performed to characterize the attenuation of vibration in the streamwise direction of a baffle plate. It was show that the attenuation was largely effected by the presence of cavitation. Attenuation was shown to be a function of the geometry of the baffle plate.

This work resulted in empirical models that can be used for predicting pipe vibration levels, the point of cavitation inception, and the streamwise distance where the attenuation of vibration levels caused by a baffle plate occurs.

Keywords: Gavin Holt, flow, fluids, vibration, vibrations, cavitation, flow, induced, pipes, pipe, fluid structure, inception, attenuation, loss coefficient, baffle plate, multi-hole orifice, flow rate, pipe flow, turbulence, turbulent, discharge coefficient, size scaling

ACKNOWLEDGMENTS

I would first like to thank Dr. Daniel Maynes for his time, insight, and guidance. The time that he sacrificed and provided has not only given me increased confidence and knowledge but gave the needed guidance to produce the results of this thesis. The knowledge I gained working alongside this man was priceless.

I would also like to thank Dr. Jonathan Blotter for his time and guidance given. Without his interest in the project and his insight, this work would not have been able to move forward.

This work was funded by Control Components Inc. Their interest in this work has provided the funding for my education and means for this work to go forth.

Finally I would like to thank my family for the time they sacrificed and their patience with me. I would especially like to thank my wife Shauna for enduring with me and her motivational love and support.

TABLE OF CONTENTS

LIST OF TABLES

LIST OF FIGURES

NOMENCLATURE

A' RMS of pipe wall acceleration (m/s^2)

$A_c^{'}$ RMS of pipe wall acceleration at critical cavitation (m/s^2)

$A_i^{'}$ RMS of pipe wall acceleration at inception (m/s^2)

A'^* Non-dimensionalized A', $\frac{A'd}{v_H^2}$ (-)

$A_2^{'*}$ Non-dimensionalized A', $\frac{A^{'}D}{v_p^2}$ (-)

$A_c^{'*}$ Non-dimensionalized A' at critical cavitation, $\frac{A_c^{'}d}{v_{H_c}^2}$ (-)

$A_i^{'*}$ Non-dimensionalized A' at inception, $\frac{A_i^{'}d}{v_{H_i}^2}$ (-)

A_H Total baffle hole area, $\frac{\pi n d^2}{4}$ (m^2)

A_j Total area made from the jets of the vena-contracta (m^2)

A_p Pipe area (m^2)

c_d Discharge coefficient (-)

D Pipe diameter (m)

d Baffle hole diameter (m)

K_{LH} Loss coefficient based on baffle hole velocity, $\frac{P_1-P_2}{1/2\rho v_H^2}$ (-)

K_{Lp} Loss coefficient based on the pipe velocity, $\frac{P_1-P_2}{1/2\rho v_p^2}$ (-)

K_{LA} Theoretical loss coefficient for a thick plate (-)

K_{LD} Theoretical loss coefficient for a thin (-)

m Slope of the non-cavitating regime for $A^{'}$ vs. cavitation number with log-log scale (-)

l_e length of the developing section (m)

$_2m$ Slope of the incipient regime for $A^{'}$ vs. cavitation number with log-log scale (-)

$m*$ A normalized slope value, $\frac{m}{2\,ln\left(\frac{A_H}{A_p}\right)-0.4}$ (-)

n Number of baffle holes (-)

P_1 Upstream pressure (Pa)

P_2 Downstream pressure (Pa)

P_j Jet pressure (Pa)

P_v Vapor pressure (Pa)

Re_D Reynolds number, $\frac{\rho v_p D}{\mu}$ (-)

SSE Size scale effects for the cavitation number, $\left(\frac{D}{d}\right)^Y$ (-)

t Baffle plate thickness (m)

v_H Average baffle hole fluid velocity (m/s)

v_{Hc} Average baffle hole fluid velocity at critical cavitation (m/s)

v_{Hi} Average baffle hole fluid velocity at cavitation inception (m/s)

v_j Average jet velocity (m/s)

v_p Average pipe fluid velocity (m/s)

v_{pc} Average pipe fluid velocity at critical cavitation (m/s)

v_{pi} Average pipe fluid velocity at cavitation inception (m/s)

x Streamwise distanced from baffle plate (m)

Y A scaling factor used for, $0.3K_{L_p}^{-0.25}$ (-)

α Vena-contracta contraction ratio, $\frac{A_j}{A_H}$ (-)

β_i A non-dimensional number, $\sigma_i \left(\frac{t}{d}\right)^{1.8} \left(\frac{A_H}{A_p}\right)^{-0.6}$ (-)

β_c A non-dimensional number, $\sigma_c \left(\frac{t}{d}\right)^{1.8} \left(\frac{A_H}{A_p}\right)^{-0.6}$ (-)

ϵ A non-dimensional number, $\left(\frac{d}{D}\right)\left(\frac{t}{d}\right)^{0.4} \left(\frac{A_H}{A_p}\right)^{2.5}$ (-)

μ Fluid dynamic viscosity (N s/m^2)

ϕ $\left(\frac{t}{d}\right)\left(\frac{A_H}{A_p}\right)^{1/5}$ (-)

ψ $c_d\left(\frac{t}{d}\right)^{0.15}$ (-)

ρ Fluid density (kg/m^3)

σ Cavitation number, $\frac{P_2-P_v}{P_1-P_2}$ (-)

σ_c Critical cavitation number (-)

σ_{ch} Choked cavitation number (-)

σ_i Incipient cavitation number (-)

σ_c^* $\sigma_c SSE$ (-)

σ_i^* $\sigma_i SSE$ (-)

1 INTRODUCTION

Many industries rely heavily upon pipe systems. These systems may result in vibration induced fatigue failure if prolonged vibration loading prevails. Vibration fatigue of a pipe can be a result of fluid induced vibrations or mechanical induced vibrations. Fluid induced vibrations are the result of large pressure surges (such as water hammer), cavitation, and turbulent flows. The focus of this work is turbulence and cavitation induced vibrations that result from multi-holed baffle plates in a pipe system. A baffle plate is a thin metal plate with multiple holes, with the number of holes varying depending on the desired flow rates through the system. Figure 1 is an image of a baffle plate that was used in this study. Baffle plates can be used to model high pressure drop valve systems that often have similar geometries and are used to control pressure drop in the system. Due to the intrusive nature of the baffle plates, high levels of turbulence and, when high flow rates are achieved, cavitation can occur.

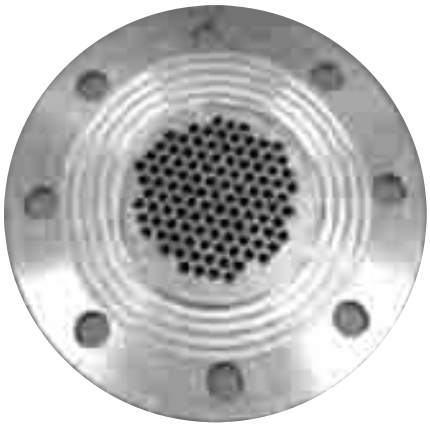

Figure 1: Typical baffle plate used

Cavitation is the generation of small vapor bubbles within a liquid system, similar to boiling. It results due to the local static pressure dropping below the vapor pressure. In the case of a baffle plate, as the fluid approaches the baffle hole it accelerates causing the pressure to drop. If the pressure drops below the vapor pressure, vapor bubbles then form and convect downstream where the pressure then increases. With this increase in pressure the vapor bubbles are forced to collapse upon themselves releasing high amounts of acoustical energy that cause pipe vibrations. The vibrations caused by cavitation can be orders of magnitudes greater than the vibration level that exists when cavitation is not present.

In Figure 2 an illustration of the physical occurrence through a baffle plate is shown. As the flow passes through the baffle plate it forms what is referred to as a vena-contracta. As the fluid exits the baffle plate it forms multiple turbulent liquid jets and shear layers where high levels of turbulence production is occurring. When cavitation is present vapor regions occur within the liquid jets. As is depicted in the illustration, the jets interact with each other whether or not cavitation is present. For this reason the geometric dimensions of the baffle plate have a large effect on the level of turbulence and cavitation that is produced.

As was mentioned above, industrial systems may fail due to the turbulent and cavitation induced vibrations. The result of such failures may result in tremendous cost in both time and money. At present, the needed information and tools necessary for a designer to take in account the loading caused by cavitation and turbulence induced vibrations for flow through multi-holed baffle plates are not available.

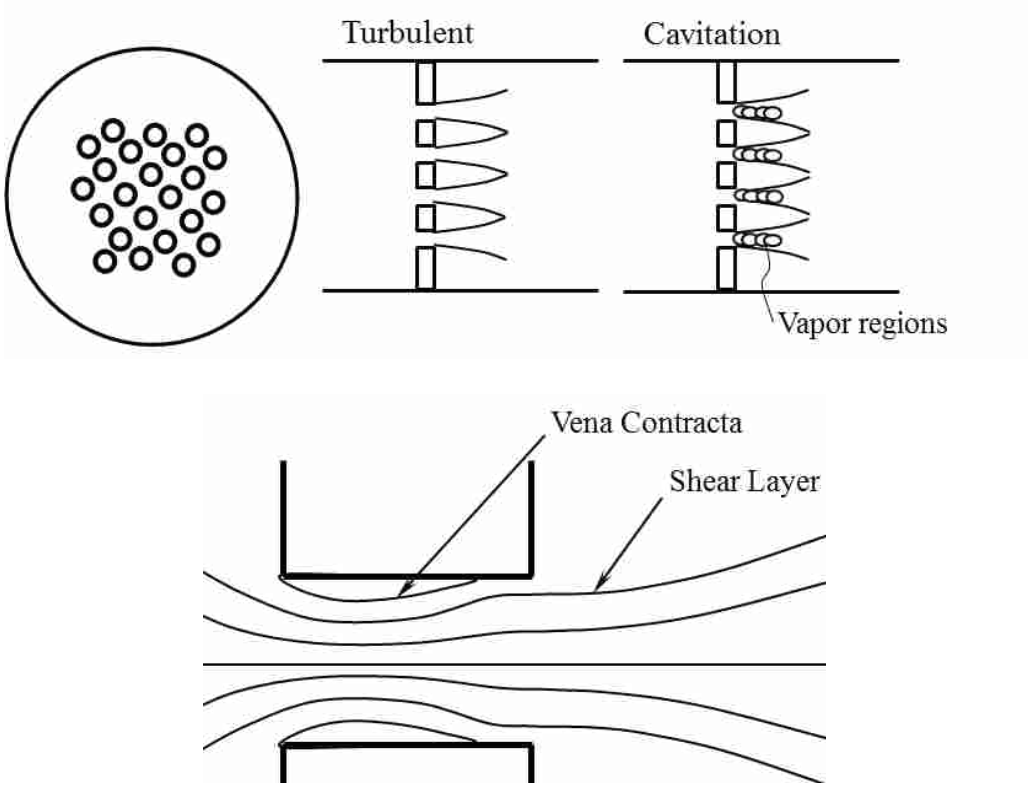

Figure 2: Illustration of Turbulent and cavitatating flow through a baffle plate. An illustration of the vena-contracta through one hole in a baffle plate is also depicted.

Within the nuclear industry vibration induced fatigue is one of the predominate failures of pipe systems [1]. In a nuclear power plant in Daya Bay China, within only eight years of operations, the plant launched a research project because vibration induced fatigue was occurring. The outcome of the research showed that cavitation, which occurred from the pressure drop over an orifice plate, was the source to the vibration induced fatigue failures [2].

In Cohasset Minnesota on July 4, 2002 a pipe ruptured due to vibration induced fatigue, releasing three thousand barrels of crude oil. The repair and cleanup costs were about $5.6 million [3]. Figure 3 shows the oil spilled from the failed pipe system illustrating the impact of this event.

Figure 3: Rupture due to vibration induced fatigue caused an oil spill in Cohasset, Minnesota. The top image shows an image of the area of the oil spill and the bottom image shows the one mile smoke plume. [3]

The focus of this work is to produce the needed information and predictive tools necessary for the design and maintenance of valve and pipe systems where baffle plate type geometries are encountered. Such tools will lead to improved future designs of industrial pipe systems, leading to reduced failures and saving millions of dollars.

1.1 **Research Objectives**

Four main objectives of this research are outlined below:

1. Perform experiments that characterize the inception of cavitation in terms of baffle plate variables, such as baffle hole diameter, baffle plate thickness, through area ratio, baffle hole spacing, fluid velocity, etc.
2. Conduct experiments that characterize the concomitant pipe acceleration as a function of the influencing parameters.
3. Conduct experiments that characterize the streamwise distance downstream where the attenuation of pipe wall vibrations caused by a baffle plate occurs, as a function of baffle hole diameter, through area ratio, hole spacing, plate thickness, fluid velocity, etc.
4. Produce predicted models that can be used in design and modification of industrial systems.

1.2 **Project Scope**

The scope of this research was to investigate experimentally the influence of sharp-edged baffle plates on pipe vibration and to produce predictive models that characterize the experimental results. The primary parameters of significance that were studied were: baffle hole diameter, number of baffle holes, fluid kinetic energy in the baffle holes, bulk fluid flow rate, baffle plate thickness, and baffle plate pressure loss coefficient.

This work was limited to flow through a pipe diameter of 10.16 cm. The range of baffle plate geometries was limed to baffle hole diameters ranging from 0.16-2.54 cm and through area ratios ranging from 10.9%-60.9%. The range of baffle fluid velocities was limited to flow speeds below 20.2 m/s.

1.3 **Overview**

Chapter 2 provides a detailed background into turbulent and cavitation induced pipe vibrations including a section on a review of the relevant literature and the current state of the art. Concluding Chapter 2 is a discussion of the contributions this work provides relative to the current state of the art. Chapter 3 gives a detailed description of the flow facilities used to perform experimentation. This chapter will also discuss the specific geometries of the baffle plates used for this work. Chapter 3 will concluded with a discussion of the instrumentation that was used. Chapter 4 describes the experimental procedures carried out. It also discusses the methods used for data analysis and provides uncertainty analysis of all measured parameters. Chapter 5 presents the results from the experimental investigation. Discussing the general turbulent and cavitation induced pipe vibration behavior, and the attenuation of the pipe vibrations with downstream distance will be discussed. Chapter 6 will present and discuss the predictive models that were developed. Chapter 7 provides a summary of the work performed and summarizes the conclusions of the research. Chapter 7 concludes with a section on recommendations for future work in this area.

2 BACKGROUND

This section provides background and a literature review of previous work on flow induced vibrations and cavitating flow in multi-holed baffle plates. First, characterization of turbulent induced vibrations will be discussed. Second, a discussion on the influences of the loss coefficient will be provided. This is important because the loss coefficient strongly relates to cavitation inception and pipe vibrations. Lastly, a discussion of cavitation and its effects on pipe vibrations will be given.

2.1 Turbulence Induced Vibrations

Turbulence is defined by Von Karman as "…an irregular motion [4]." Turbulence is caused by a fluid reaching high enough Reynolds numbers that the viscous stresses are overcome by the fluid inertia. Fluctuating pressure and velocities then prevail and the motion becomes inherently three dimensional and unsteady [4].

Within the boundary layer fluid structures called eddies, or vortices, are generated. Eddies are defined as local swirling motion [4]. These structures have a large range of sizes and carry large amounts of energy [4]. As the flow rate increases so does the turbulence or generation of these vortices. Due to the no-slip condition, as the vortices approach the wall of the pipe, the kinetic energy that they are carrying must be converted to some other energy source according to the first law of thermodynamics. This energy is converted to heat and pressure fluctuations [5].

For turbulent induced pipe vibrations that occur under fully-developed turbulent flow conditions without a baffle plate, it has been shown experimentally and analytically that both the pressure fluctuations and the pipe wall acceleration scale with the square of the average pipe fluid velocity [6,7,8,5].

Figure 4 is an illustration of two turbulent jets interacting. Where the shear layers of the two jets interact the velocity of the rotational flow in the dominant turbulent eddies of the two jets are opposite. This can cause suppression to the levels of turbulence [9]. Because of this it is believed that with increased amounts of interacting jets the pipe wall vibrations will decrease.

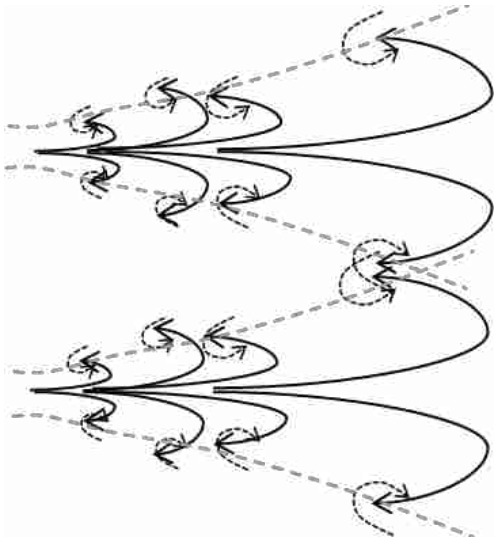

Figure 4: Turbulent jets interacting

2.2 Baffle Plate Loss Coefficient

Ball stated that the pressure drop across an orifice plate is caused by the pressure head on the plate, the losses due to friction, and the losses due to turbulence disturbances [10]. It was shown in a study performed by Kolodzie et. al. that loss, when considering multi-hole orifice

plates, was influenced by the hole diameter, through area ratio, and the pitch to diameter ratio [11].

The loss coefficient for baffle plate can be defined as the ratio of the upstream pressure minus the downstream pressure all divided by the dynamic pressure as shown in equation (2.1)-(2.2) [12]. Equation (2.2) is defined with the average fluid pipe velocity, v_p, and equation (2.2) is defined with the average fluid baffle hole velocity, v_H. By using conservation of mass these two equations can be related by the through area ratio, A_H/A_p, as shown in equation (2.3). A_H is the total area of all the baffle holes and A_p is the pipe cross-sectional area.

$$K_{Lp} = \frac{P_1 - P_2}{1/2\rho v_p^2} \tag{2.1}$$

$$K_{LH} = \frac{P_1 - P_2}{1/2\rho v_H^2} \tag{2.2}$$

$$K_{LH} = K_{Lp}\left(\frac{A_H}{A_p}\right)^2 \tag{2.3}$$

For sharp edge baffle hole or orifice, the flow through the hole creates a jet of liquid surrounded by a region of relatively stagnant fluid forming a vena-contracta [13]. Testud et. al. showed that two theoretical models could be developed for the loss coefficient dependent upon whether the flow reattaches inside of the hole or not after the vena-contracta [13]. Whether or not the flow reattaches is dependent upon the thickness to hole diameter ratio, *t/d*. These models are developed from an integral analysis of a sudden contraction followed by a sudden expansion, and are derived below.

For steady incompressible flow through a baffle plate the conservation of mass equation is shown in equation (2.4), where the average pipe velocity, v_p, multiplied by the pipe area, A_p, and equals the average jet velocity, v_j, times the total jet area, A_j, comprising all the liquid jets. Both of these must also equal the average baffle hole velocity, v_H, multiplied by the total area of the baffle holes, A_H. A_j and A_H can be seen in Figure 5 where v_j and v_H are the velocities of these respected areas.

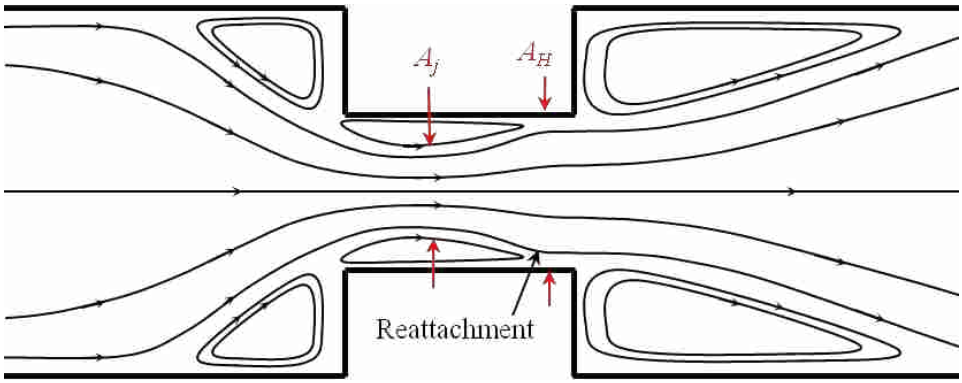

Figure 5: Illustration of a single baffle hole showing the vena-contracta region within the baffle hole.

$$v_p A_p = v_j A_j = v_H A_H \tag{2.4}$$

2.2.1 Detached Model (Thin Baffle Plate)

If the fluid passing through the vena-contracta portion of a baffle plate does not reattach to the walls of the baffle holes the flow is said to be detached. This is illustrated in Figure 6. The following analysis discusses a theoretical model for the loss coefficient when the flow is in this state by the use of an integral analysis.

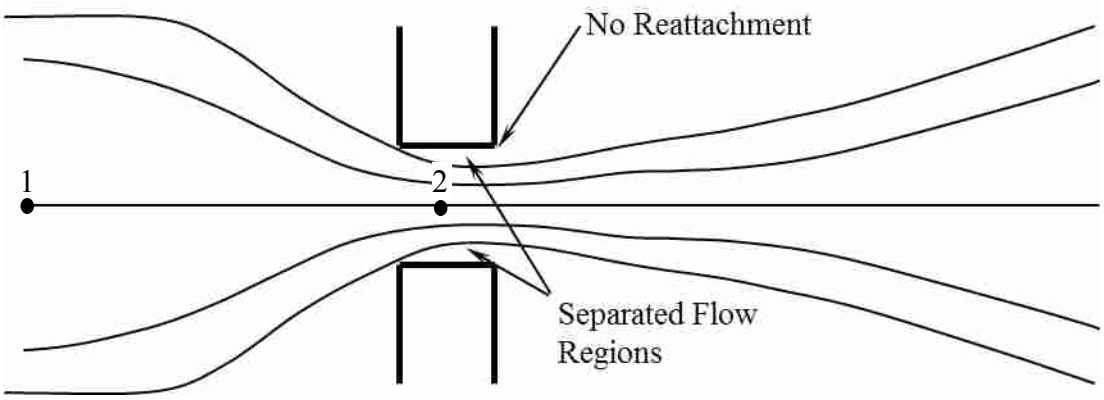

Figure 6: Illustration of a flow through a thin baffle hole when flow does not reattach after the vena-contracta (detached flow).

Considering the sudden contraction region, and assuming the flow is inviscid and steady, equation (2.5) is formed from Bernoulli's equation, where P_1 is the upstream pressure, P_j is the jet pressure, v_j is the average jet velocity, and v_p is the upstream fluid pipe velocity.

$$P_1 + \frac{1}{2}\rho v_p^2 = P_j + \frac{1}{2}\rho v_j^2 \tag{2.5}$$

An integral momentum analysis in the streamwise direction for a sudden expansion area, is now performed for the control volume depicted in Figure 7 where the incoming flow is detached and at a velocity v_j with an effective flow area of A_j.

The equation of momentum for a steady flow is

$$\sum F_x = \int_{cs} \rho u(\vec{u} \cdot \vec{n}) dA \tag{2.6}$$

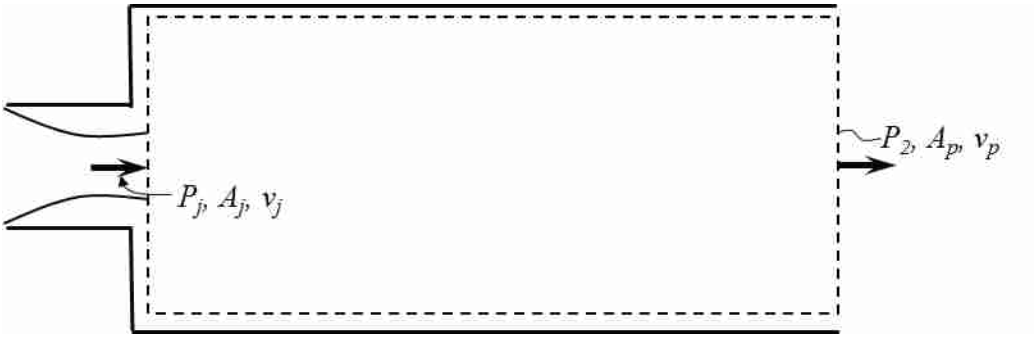

Figure 7: Control volume for sudden contraction for a detached jet

Where u is the velocity in the streamwise direction. The only forces on the control volume are pressure forces and the velocities at the inlet and exit of the control volume are assumed to be uniform. Thus, equation (2.6) simplifies to

$$P_j A_p - P_2 A_p = \rho(v_p^2 A_p - v_j^2 A_j) \tag{2.7}$$

Dividing both sides by the dynamic pressure yields

$$\frac{P_j - P_2}{1/2\rho v_p^2} = 2 - 2\frac{A_p}{A_j} \tag{2.8}$$

Combining equations (2.5) and (2.8) and using equation (2.4), an equation for the pipe loss coefficient can be produced as shown in equation (2.9).

$$K_{Lp} = \frac{P_1 - P_2}{1/2\rho v_p^2} = \left(\frac{A_p}{A_j}\right)^2 - 1 + 2 - 2\frac{A_p}{A_j} \tag{2.9}$$

After introducing the total baffle hole area, A_H, an equation for the detached loss coefficient equation is obtained as shown in equation (2.10)

$$K_{Lp} = \frac{P_1 - P_2}{1/2\rho v_p^2} = \left(\left(\frac{A_p}{A_H}\right)\frac{1}{\alpha} - 1\right)^2 \tag{2.10}$$

where

$$\alpha = \frac{A_j}{A_H} \tag{2.11}$$

2.2.2 Attached Model (Thick Plate)

For a thick baffle plate the same upstream assumptions and equations can be assumed as the thin plate discussed above and shown in equation (2.5). However, the conditions downstream of the plate are now different. Because the flow reattaches itself inside of the hole, there will be loss due to the turbulent mixing and frictional resistance within each of the baffle holes. To account for this a momentum integral analysis is performed in the baffle holes from the point of the throat in the vena-contracta to the hole exits shown in Figure 8. The result is an expression for the pressure at the exit of the baffle holes. A_H is the total baffle hole area and P_H is the baffle hole pressure at the exit of the baffle hole

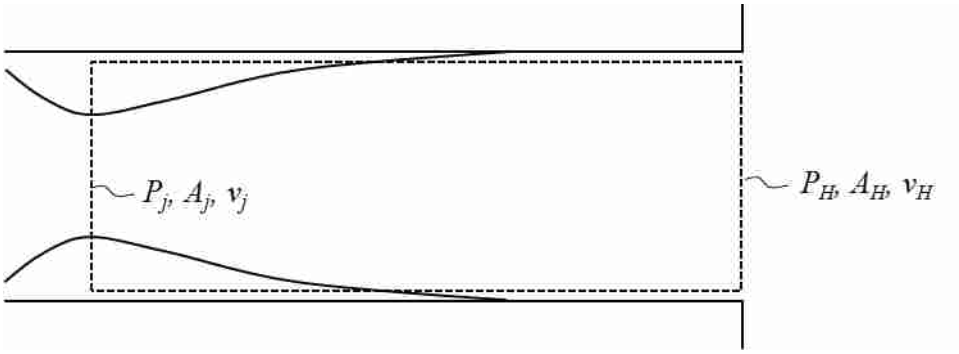

Figure 8: Control volume within baffle hole with attached jet.

Apply equation (2.6) to the control volume of Figure 8 one obtains

$$A_H P_j - P_H A_H = \rho(v_H^2 A_H - v_j^2 A_j) \tag{2.12}$$

And after rearrangement of equation (2.12) results

$$\frac{P_j - P_H}{1/2\rho v_p^2} = 2\left(\frac{A_p}{A_H} - \frac{A_H}{A_j}\right) \tag{2.13}$$

By again performing a momentum integral analysis using equation (2.6) on the sudden expansion, but now for the thick plate scenario equation (2.14) is obtained. Figure 9 shows the control volume used in the analysis.

Figure 9: Control volume for a sudden contraction area when the flow reattaches within the baffle plate

$$P_H A_p - P_2 A_p = \rho(v_p^2 A_p - v_H^2 A_H) \tag{2.14}$$

Combining equations (2.5), (2.13), and (2.14) and using equation (2.4), an equation for the loss coefficient across the plate can be produced and is shown in equation (2.15).

$$K_{Lp} = \frac{P_1 - P_2}{1/2\rho v_p^2} = 1 - 2\frac{A_P}{A_H} + 2\left(\frac{A_P}{A_H}\right)^2\left(1 - \frac{1}{\alpha} + \frac{1}{2\alpha^2}\right) \tag{2.15}$$

2.3 Cavitation and Cavitation Induced Vibrations

Cavitation is a process in which a liquid vaporizes and condenses. This process occurs due to the pressure dropping to or below the vapor pressure while the temperature is held constant. For cavitation to occur there must be a liquid/gas interface. These are typically found at nucleation sites on surfaces on where tiny gas bubbles are trapped or in the flow where absorbed air exists [14].

Turbulent eddies, when present, can play a large role in cavitation production. Because of the high rotational speed of an eddy the pressure inside is significantly lower than the surrounding pressure. If a nucleation site is found within the eddy (as in microscopic dissolved gases bubbles) and the pressure drops to the vapor pressure, cavitation bubbles can form within these eddies. As they grow these cavitation bubbles cause the eddy to weaken until it is dissipated. When this occurs the pressure at the center of the eddy rises which causes the vapor bubble to collapse upon itself [15]. Figure 10 provides an example of this where a vapor bubble can be seen growing and stretching within the shear layer of a jet flow.

For a baffle plate, as the flow approaches the baffle hole it is forced to accelerate, as illustrated schematically in Figure 11, causing the pressure to drop. When this pressure drops below the vapor pressure, P_v, vapor bubbles form at nucleation sites. These bubbles are then carried downstream to a point where the pressure begins to rise, causing the bubbles to collapse on themselves. At bubble collapse a large amount of energy is released, resulting in heating, pipe degradation, sound, and pipe vibrations.

To characterize the intensity of cavitation the cavitation number, σ, is often used. σ is defined as the ratio of the downstream pressure, P_2, minus the vapor pressure, P_v, over the pressure drop across the plate, as shown in equation (2.16).

$$\sigma = \frac{P_2 - P_v}{P_1 - P_2} \tag{2.16}$$

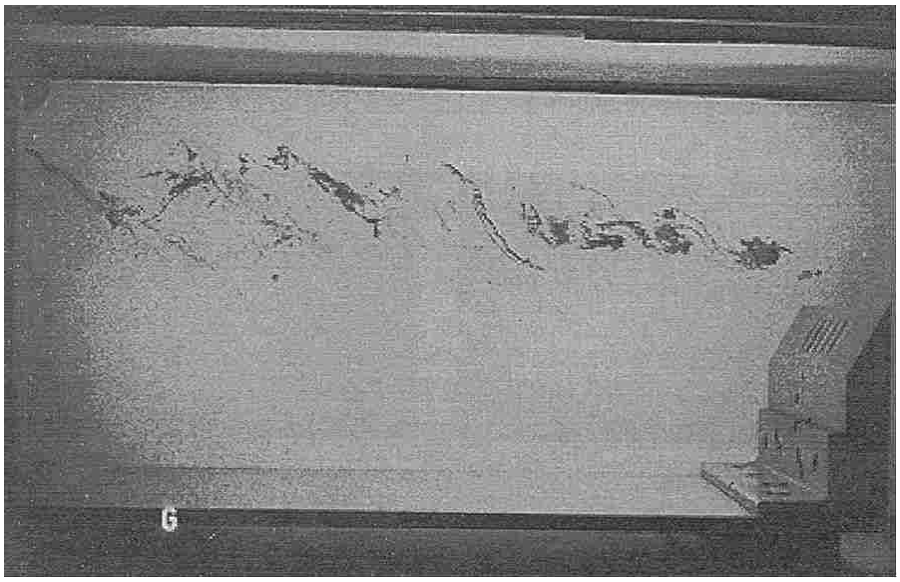

Figure 10: Example of cavitation bubble formation within the shear layer from a baffle plate within a pipe section from [16].

A cavitation number based off of the upstream pressure is also often used as shown in equation (2.17). These two cavitation numbers can be related by equation (2.18).

$$\sigma_2 = \frac{P_1 - P_v}{P_1 - P_2} \tag{2.17}$$

$$\sigma = \sigma_2 - 1 \tag{2.18}$$

A cavitation number based off of the dynamic pressure rather than the pressure drop can also be used and is defined in equation (2.19). σ and σ_v can be related to each other, with the pipe loss coefficient, as show in equation (2.20).

$$\sigma_v = \frac{P_2 - P_v}{1/2\rho v_p^2} \tag{2.19}$$

$$\sigma = \frac{\sigma_v}{K_{Lp}} \tag{2.20}$$

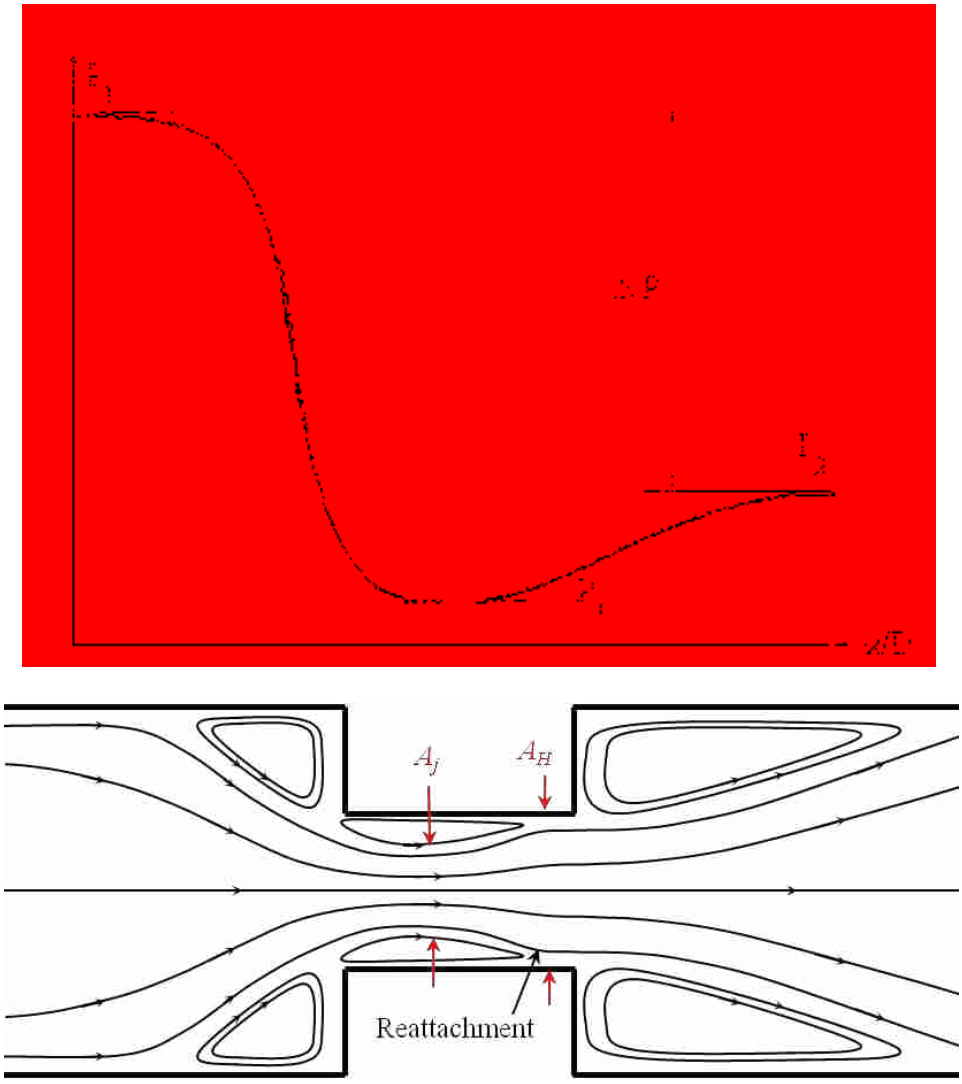

Figure 11: (Top) Illustration of the pressure variation across a sudden contraction and then sudden expansion. (Bottom) A schematic illustration of the vena-contracta section of a sudden contraction/sudden expansion (baffle plate) with reattachment of the flow occuring after the vena-contracta.

Because of the noise and vibrations that are produced when cavitation is occurring, These two measures are often used to characterize cavitation levels [17]. Figure 12 shows the typical behavior of the pipe wall acceleration as a function of cavitation number, σ, for a typical baffle plate. Shown is the root mean square (RMS) of the pipe wall acceleration, A', plotted with respect to the cavitation number. The data reveal the existence of four distinct cavitation regimes. The first (black line) is the turbulent regime where cavitation has not occurred and the vibrations are due entirely to the turbulent jets. The second (red line) is where the acceleration levels dramatically increase over a short span of cavitation numbers. This regime represents where cavitation has onset, although the cavitation in this regime is only intermittent. The third (blue line) is the regime where the flow is fully cavitating. The fourth (green line) is where choking has occurred and the vibration levels decrease. The points where the lines intersect are all critical cavitation numbers and are defined as [18]:

- The inception cavitation number (σ_i)
- The critical cavitation number (σ_c)
- The choking cavitation number (σ_{ch}).

The incipient cavitation number, σ_i, is the point where cavitation first occurs and where small vapor bubbles are formed irregularly [10]. The noise sounds like light intermittent popping that can barely be heard over the turbulent flow generated noise [18]. This point is a design limit that is often used when no cavitation is desired within a system [18].

The critical cavitation number, σ_c, is where the flow is fully cavitating, or there is a constant generation of vapor bubbles [15]. The noise that occurs at this point sounds like bacon crackling [18]. This is a design limit that is used when some cavitation can be permitted. Many systems that operate continuously are often run to this limit [18].

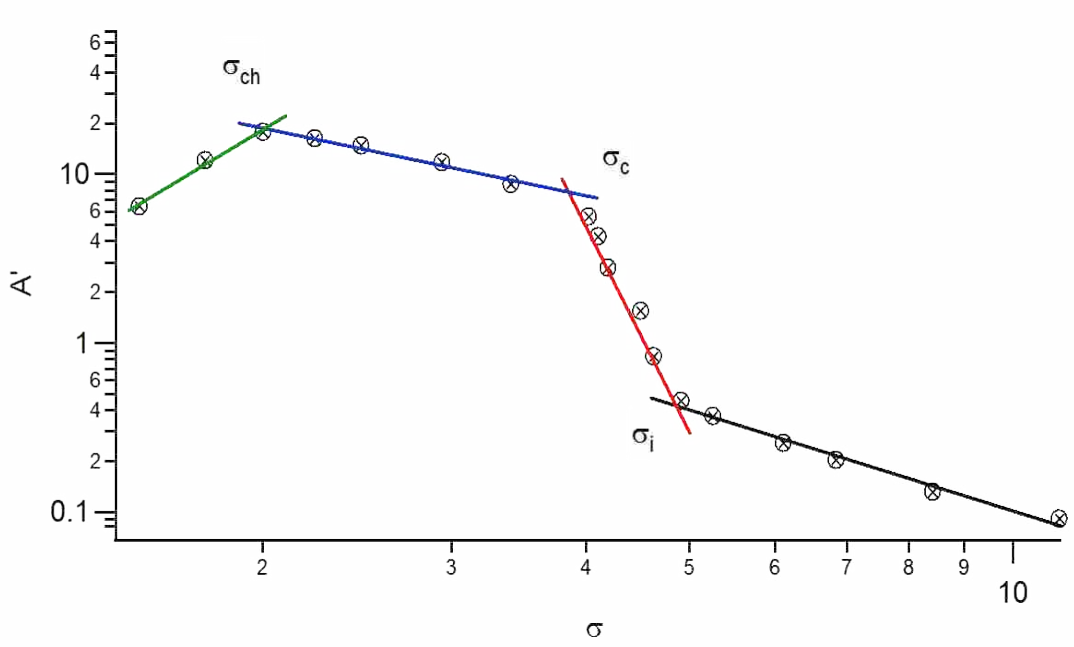

Figure 12: A representative plot of A' vs. the cavitation number, σ, showing four different cavitation regimes. The black line is the non-cavitating regime, the red line is the incipient cavitation regime, the blue line is the fully cavitating regime, and the green line is the choked cavitating regime. The intersection of the red and black lines is the incipient cavitation design limit, σ_i, the intersection of the blue and red lines is the critical cavitation design limit, σ_c. and the intersection of the green and blue lines is the chocked cavitation design limit , σ_{ch}.

The choking cavitation number (σ_{ch}), which is not explored in this research, is the point where choked flow, due to the amount of cavitation bubbles in the flow, is occurring. This is the point when the flow has reached a maximum mass flow rate and can no longer increase with increased pressure drop.

It has been shown that the cavitation number, although non-dimensional, is not free from scaling effects like other non-dimensional numbers are. A scaling effect is when the changing of size or pressure variations from application to application has effects on the parameter. This has made it difficult to model cavitation. The cavitation number is affected by both size scale effects and also pressure scale effects [16]. Tullis stated, however, that in the cases of obtaining

inception and critical cavitation values the uses of pressure scale effects are not needed when using an orifice plate or sudden enlargement [15].

The size scale effect that is currently used in industry is shown in equations (2.21)-(2.22). [18,15,16] As can be seen, the size scale effect is dependent upon the pipe diameter, *D*, the baffle hole diameter, *d*, and the pipe loss coefficient, K_{Lp}. These equations are developed empirically by studies conducted by Tullis with single hole orifice plates [15].

$$SSE = \left(\frac{D}{d}\right)^{Y} \tag{2.21}$$

$$Y = 0.25K_{LP}^{-0.3} \tag{2.22}$$

As shown in equations (2.23)-(2.24) to obtain the adjusted cavitation inception and critical number, σ_i^* and σ_c^*, the actual cavitation number at inception, or critical value, (σ_i and σ_c) must be multiplied by the size scale effect, *SSE,* described above. σ_i^* and σ_c^* are cavitation numbers adjusted for size scale effects.

$$\sigma_i^* = SSE\sigma_i \tag{2.23}$$

$$\sigma_c^* = SSE\sigma_c \tag{2.24}$$

2.4 Literature Review

The following discusses literature that defines the current state of turbulence and cavitation induced pipe vibrations for liquid flow through baffle plates. They are divided into two sections those describing turbulence induced vibrations and those addressing cavitation induced vibrations.

2.4.1 Turbulent Induced Pipe Vibrations

In a study performed by Qing et. al. [19], wall pressure fluctuations caused by water flow through single hole orifices were explored experimentally. Two orifices with through area ratios of A_H/A_p= 0.255 and 0.335 were used in the investigation with flow rates of 15, 20, 25 m^3/h. It was shown that the majority of the pressure fluctuations occurred right after the orifice plate. This was believed to be due to the large circulating flow that is produced outside of the shear layer of the jet. The RMS of the pressure fluctuations and the peak frequency of the pressure density, decreased with increased distance in the streamwise direction from the orifice plate. It was also observed that the smaller the through area ratio the higher the RMS of the pressure fluctuations were. The investigation also looked into the pipe vibrations that were occurring so as to observe the strength of the fluid-structure interactions. The results revealed that the lower frequency vibrations that occurred were at about the pipe natural frequencies showing that the system was a weakly coupled fluid-structured system.

Thompson [7] conducted a preliminary experimental investigation of baffle plate influence on pipe vibrations. The experiments were conducted using five baffle plates of varying baffle hole diameters ranging from 0.159 -2.54 cm with a pipe section that was 10.16 cm diameter PVC pipe. The total through area ratio, A_H/A_p, for all plates was nominally 0.438. Pipe

wall acceleration data were acquired over a range of average pipe fluid velocities ranging from 0-7 m/s. The root mean square (RMS) of the acceleration data were acquired, defined as A', and compared to the flow velocities and the streamwise distance from the baffle plate, x/D. The investigation showed that the measured vibration levels within the turbulent regime increase with increased baffle hole size, while holding A_H/A_p constant. It was also shown that the magnitude of the vibration levels decreases with increasing distance downstream of the baffle plate normalized by the pipe diameter, x/D, as illustrated in Figure 13 [7]. For the case of no baffle plate, there is essentially no variation in the observed A' level with change in measurement location, x/D, on the pipe. When a baffle plate is present, however the vibration levels are strongly dependent upon the measurement location. This result shows that at small x/D the acceleration of the pipe is greater, as expected. With increasing x/D, the vibrations decay and eventually merge with the no baffle plate levels. The location where the vibrations have attenuated was observed to increase with increased baffle hole size.

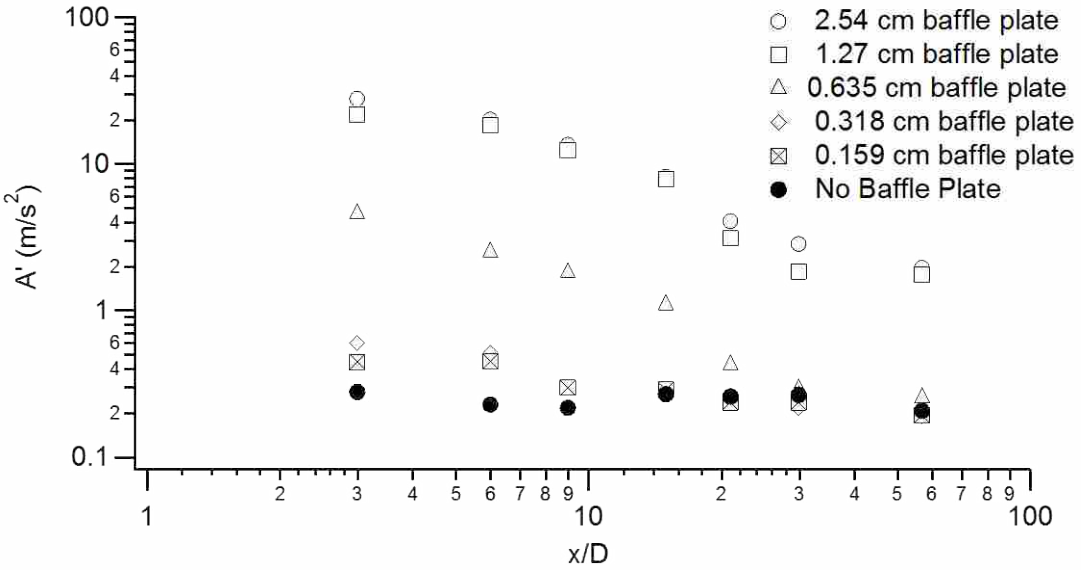

Figure 13: Pipe wall acceleration vs. downstream distance normalized by the pipe diameter, x/D, for 5 baffle plates with varying hole diameters and a no baffle plate case as measured by Thompson as shown in the legend [7].

It was also shown that when a baffle plate was present, A' scaled approximately with the pipe fluid velocity to a power that varied with baffle hole size. This power approached the power of two (for no baffle plate case) with decreased hole size [7].

2.4.2 Cavitation Induced Pipe Vibrations

A study was performed on noise generated from a single-hole orifice plate and one multi-hole orifice plate by Testud et. al. [13]. The experiments conducted were in an open water loop made of smooth steel pipe with an inner diameter of 7.4 cm and a pipe wall thickness of 0.8 cm. Only two plates were tested, a single hole orifice plate with orifice diameter of 2.2 cm and thickness of 1.4 cm, and a multi-hole orifice plate with plate thickness of 1.4 cm and 47 sharp-edged holes of a diameter of 0.3 cm. The Reynolds number based on the average pipe fluid velocity and pipe diameter varied from 2×10^5 to 5×10^5. The results showed that cavitation inception occurred at a cavitation number of $\sigma \cong 7.4$ for both plates. It was observed that sound levels were much higher for the single-hole orifice plate compared to the multi-hole plate with the same through area ratio. Whistling was observed for the single-hole orifice plate only, and it was concluded that the whistling phenomenon is a function of the plate thickness ratio. It was also shown that the loss coefficient of the plate is a function of the plate thickness ratio and was estimated using the Borda-Carnot model. In a comparison between cavitation noise from the single hole orifice and standard turbulent noise from a non-cavitating plate there was good agreement within the low frequency range.

Thompson [7] performed a preliminary study on liquid flow through baffle plates, as was discussed in section 2.1. Over the range of flow rates that were explored, for three of the five

baffle plates that were employed cavitation was present. It was observed that by increasing the size of the baffle plate holes, cavitation occurred at lower flow rates. This can be seen in Figure 14 [7], where cavitation was not seen to be present until the hole size was increased to 0.635 cm at an average pipe fluid velocity of nominally 5.8 m/s. As the hole size was increased, cavitation occurred at lower flow velocities and for the baffle plate with hole sizes of 2.54 cm cavitation occurred at a flow rate of about 2.7 m/s. It was shown that the A' level was about an order of magnitude greater for flows where cavitation was present as compared to when it was not. Figure 15 shows the power spectral density (PSD), $\hat{A}$, for the five baffle plates used at an average pipe fluid velocity of 5.63 m/s and measured at 0.305 m downstream of the baffle plates. This data shows that the peak frequencies in the pipe vibrations were not resolved in these experiments due to the low sample frequencies. This can be seen with the 0.159 and the 0.635 where at a frequency of 25 kHz $\hat{A}$ is still increasing and the maximum $\hat{A}$ is not fully resolved.

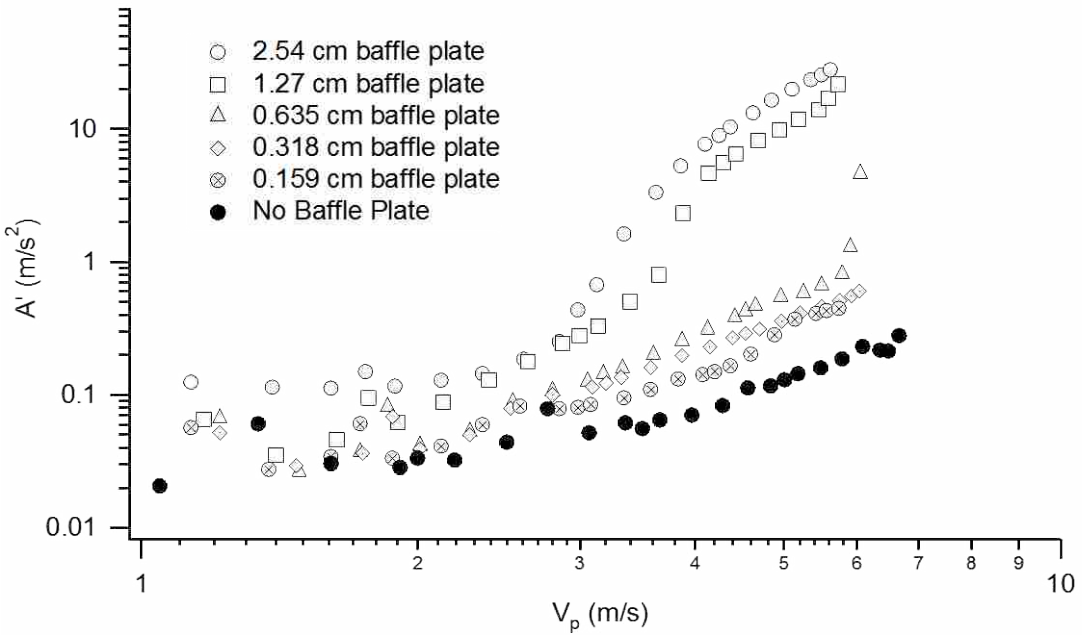

Figure 14: A plot of the pipe wall acceleration, A', vs. the average pipe fluid velocity, v_p, for 5 baffle plates with varying baffle hole diameters that were used by Thompson as shown in the legend [7].

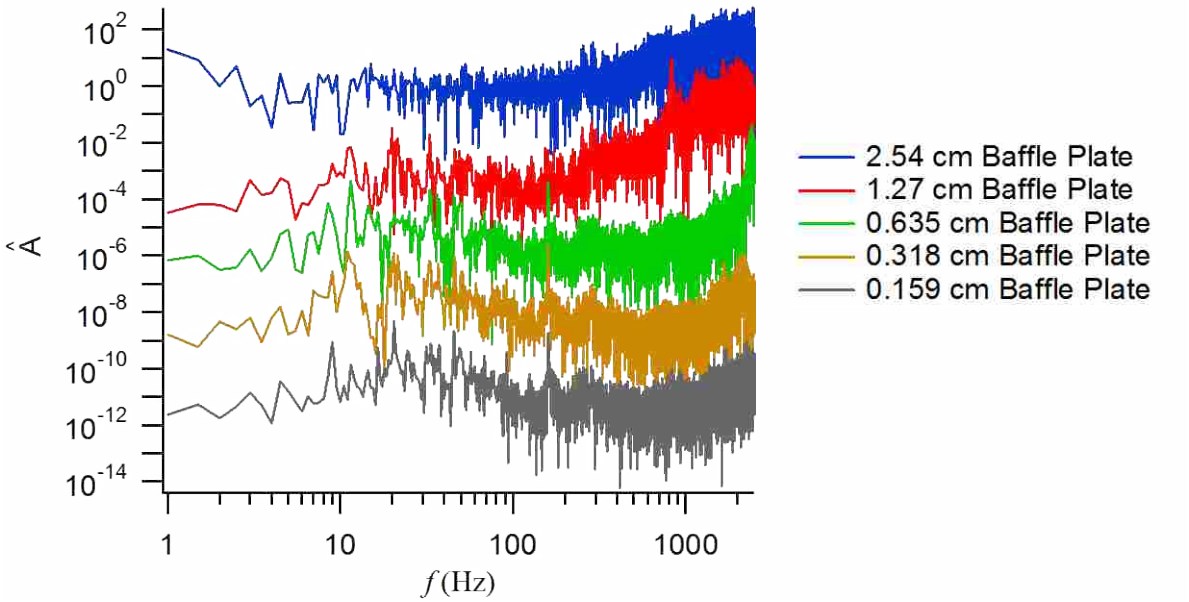

Figure 15: Power spectral density, $\hat{A}$, vs. frequency, f, for five baffle plates with varying baffle hole diameters studied by Thompson [7], as shown in the legend, at a flow speed of 5.63 m/s measured at 0.305 m downstream from the baffle plate.

Tullis et. al. [9] conducted an experimental study on flow through perforated orifice plates and discussed how they are used as energy dissipaters. The study was performed on six plates, all of a thickness of 2.54 cm that varied in number of holes from 19-121 holes. The perforated hole diameter for each plate was 2.54 cm with a large rounding radius of 0.95 cm for the inlet of each hole. Flow through 25.4 cm, 40.64 cm, and 50.8 cm pipes was considered. Through this study it was shown that the inception cavitation number, σ_i, for multi-hole orifice plates is dependent upon the coefficient of discharge, c_d, defined in equation (2.25). Figure 16 reveals the results of cavitation as a function of the discharge coefficient. The data shows that with decreased discharge coefficient the onset of cavitation occurs at lower cavitation numbers. The study also revealed that the suppression of cavitation, caused by the interacting jets, is lessened with decreased pipe size. It was believed that with a small enough pipe diameter the

flow would behave like a single hole orifice plate. Through the entire flow regime that was investigated, no cavitation erosion damage was observed on the pipe wall for any of the orifice plates used.

$$c_d = \frac{v_p}{\sqrt{\frac{2(P_1 - P_2)}{\rho} + v_p^2}} \tag{2.25}$$

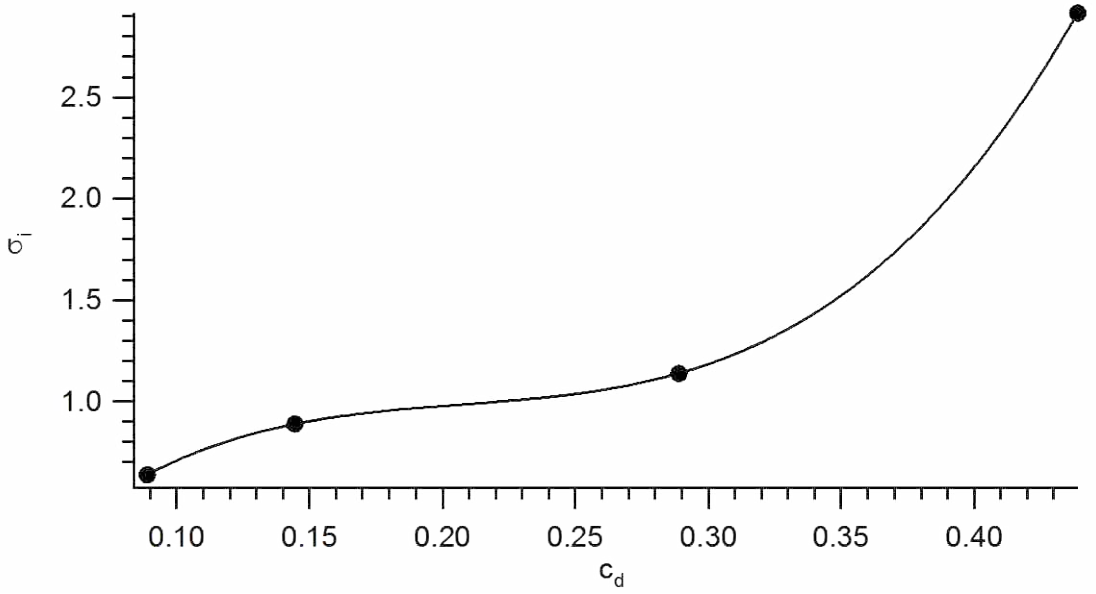

Figure 16: A plot of inception cavitation number vs. discharge coefficient for 4 multi-hole orifice plates used by Tullis et. al. [9]

2.5 **Current State of the Art**

The current state on cavitation and turbulent induced vibrations caused by baffle plates is limited in understanding and is summarized as follows:

- Characterization of cavitation inception for baffle plates is limited to the study done by Tullis et. al. [9] which was incomplete in that it did not investigate the effects of hole diameter and plate thickness and only considered rounded holes.
- The exploration of cavitation inception for sharp edged baffle plates has not been explored by any previous study to the author's knowledge.
- The characterization of A' levels for turbulent induced vibrations for baffle plate induced turbulent jets is limited and the influence of plate thickness and through area ratio has not been explored, parametrically.
- The characterization of the attenuation of A' level with downstream distance is limited to the study done by Thompson [7]. However in his study the pipe length and scenarios considered were insufficient to obtain robust results in the cavitation regime.
- Models for predicting the loss coefficient is restricted to the Borda-Carnot model explained in section 2.2 and does not adequately account for variation in the baffle plate thickness.
- No robust models for prediction of cavitation inception for baffle plates have been produced due to lack of experiments performed.

2.6 **Research Contributions**

This work explores experimentally the effects of turbulent and cavitation induced vibrations. This work investigates the dependences of the problem over a larger range of the expected variables than the current state of the art. A total of sixteen sharp edged baffle plates

were used with through area ratios ranging from 0.109-0.609, hole diameters ranging from 0.159 cm-2.54 cm, thickness ratios ranging from 0.32-0.64, and average pipe fluid velocities ranging from 0.35-8.5 m/s. This large parameter range allows for characterization to the influence of baffle plate thickness, baffle hole diameter, and number of baffle holes. Further, empirical models for predicting inception and critical cavitation have been produced. In addition, empirical models for predicting A' levels as a function of the influencing variables have also been developed.

3 EXPERIMENT SETUP

The test facilities that were used to conduct all experiments consisted of the same large water flow loop that was used by Thompson [7]. A total of 16 baffle plates (shown in Figure 21) were used with varying baffle hole diameters, through area ratios, and plate thickness. The following sections give a detailed description and explanation of each section of the flow loop. A description of the baffle plates that were used is also provided. Lastly, a discussion of the instrumentation that was used to obtain measurements will be discussed.

3.1 **Flow Loop**

Shown in Figure 17 is a schematic drawing of the flow loop facility. A photograph of a portion of the flow loop is shown in Figure 18. Flow is delivered by a Bell and Gossett centrifugal pump, driven by a 75 hp Marathon Electric 365T motor shown in Figure 18. The inlet and outlet pipes to the pump are 20.3 cm and 10.2 cm Schedule 80 PVC pipe. Downstream of the pump is a flow conditioner within an expanded pipe of 20.32 cm diameter Schedule 80 PVC pipe. This can also be seen in Figure 18. The flow conditioner consists of a 7.6 cm thick piece of aluminum honeycomb and three mesh screens all held together by aluminum rings to keep it from being forced downstream. The flow conditioner is used to straighten the flow and eliminate eddies formed by the pump. Following the flow conditioner is a reducer to 10.2 cm Schedule 80 pipe. After the reduction a Proco Series 310 rubber coupler is mounted. This is

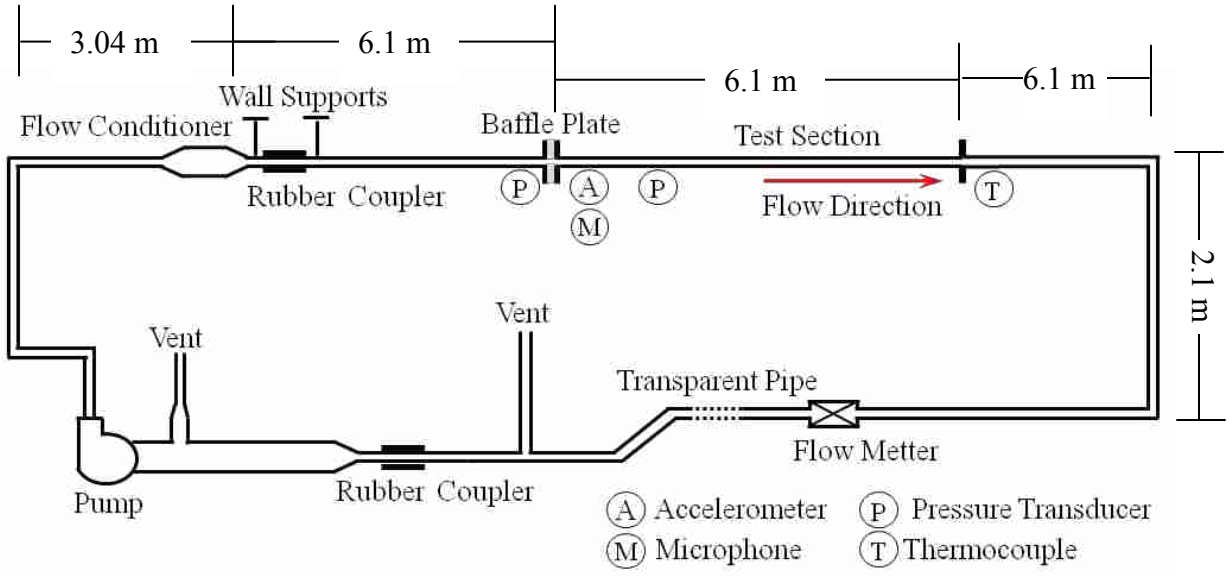

Figure 17: Schematic drawing of the flow loop facility used for all experiments.

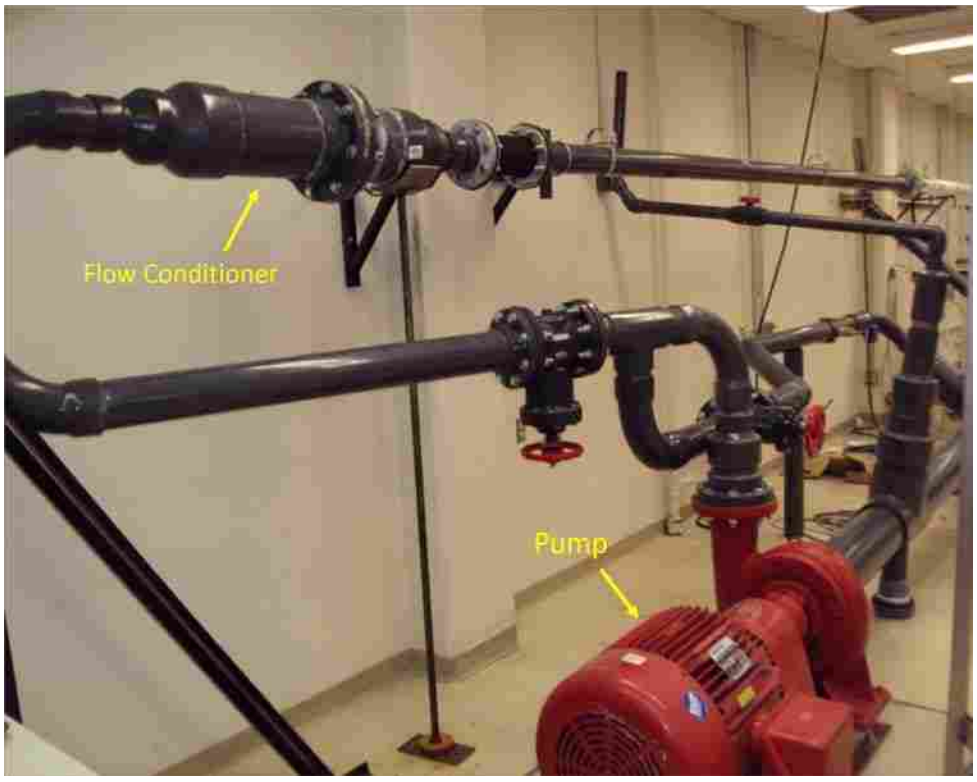

Figure 18: Photograph of the centrifugal pump and flow conditioner used in flow loop facility. Downstream of the flow conditioner the rubber coupler and developing region can be seen.

used to reduce the upstream structural vibrations caused by the pump and the flow through the pipe bends. The pipe is mounted to the wall both before and after the rubber coupler to also reduce the structural vibrations. After the rubber coupler is the developing region of the flow loop which allows the flow to become fully developed before the test section, or region where measurements are acquired. The developing region consists of a 6.1 m long 10.2 cm diameter Schedule 80 PVC pipe. Using the Schlichting-Gersten equation [12], shown in equation (3.1), the length of the pipe was verified to be long enough to allow for fully developed flow. The, l_e, is the length of the developing section, D, is the pipe diameter, and, Re_D, is the Reynolds number based upon the pipe Diameter.

$$\frac{l_e}{D} \approx 4.4 Re_D^{1/6} \tag{3.1}$$

Connected to the developing region is the pipe test section, which is made up of two 6.1 m long, 10.16 cm diameter schedule 40 PVC pipes. A photograph of the test section is shown in Figure 19. The baffle plates, as shown and discussed in section 3.2, are inserted between the test section and the developing region, as shown in Figure 20. Following the test section, the pipe eventually bends 180^o and connects to a control valve that is used to release the water from the flow loop if needed. Following the valve is a section of transparent pipe. This is used to visually inspect the flow for air bubbles. A vertical chimney vent that extends above the elevation of the entire flow loop is located after the transparent pipe. This chimney is used to fill the flow loop and also allows all the air in the system to escape. A Proco Series 310 rubber coupler follows the chimney vent and connects to an expansion that increases the pipe diameter to 20.32 cm before the pipe connects to the inlet of the pump.

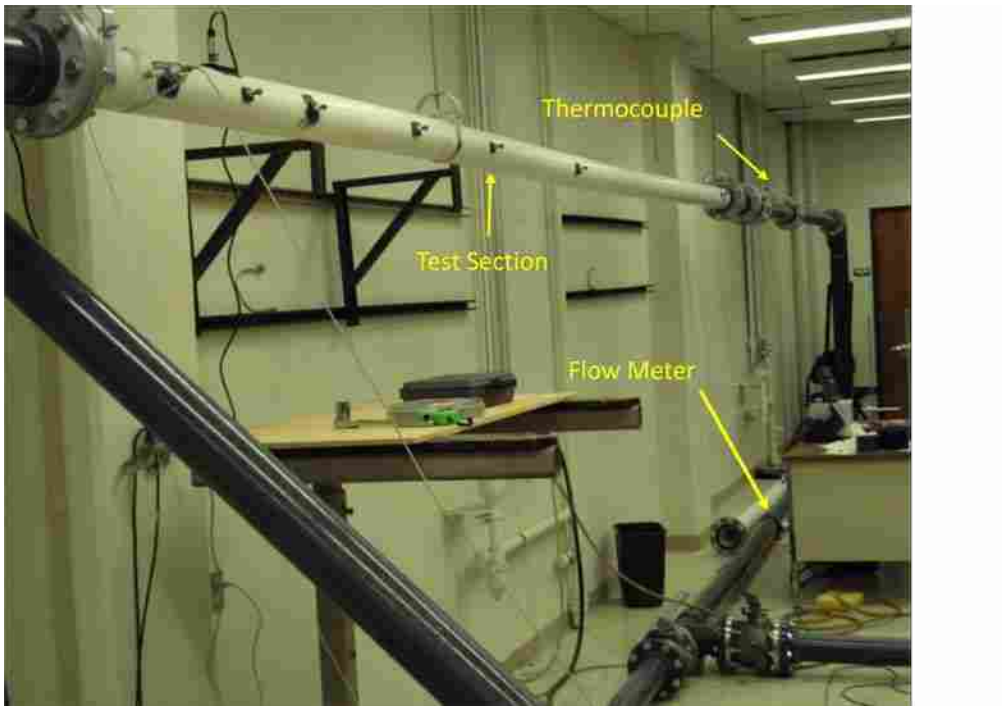

Figure 19: Photograph of the pipe test section showing the location of the thermocouple and flow meter relative to the test section.

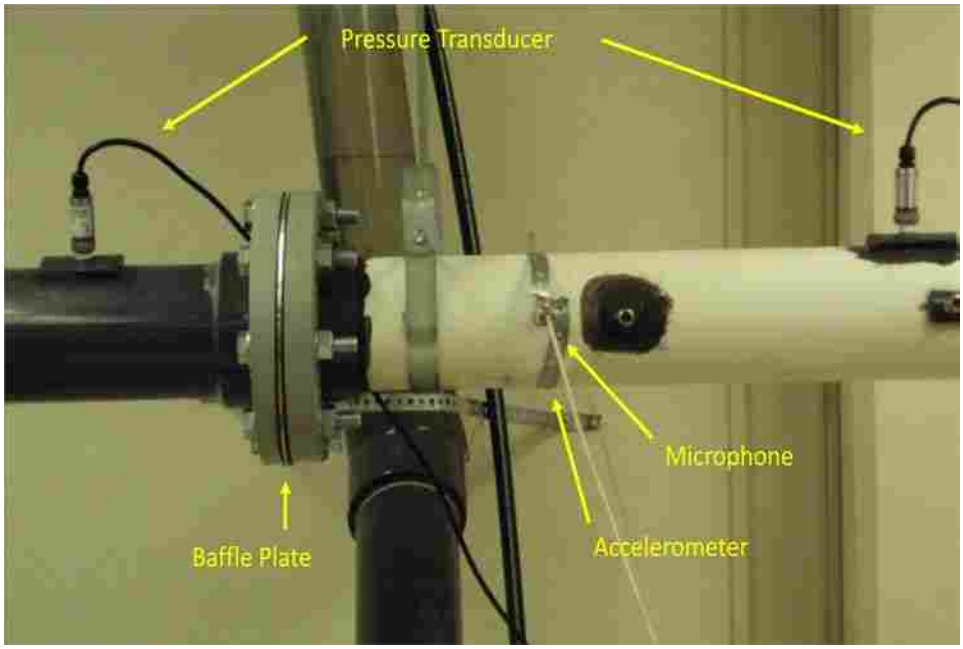

Figure 20: Photograph of a baffle plate mounted between the developing region and test section. The locations of the upstream and downstream pressure transducers along with microphone and accelerometer are also shown.

3.2 **Baffle Plates**

All baffle plates were made of aluminum and had a diameter of 22.9 cm. The baffle plates have nominal hole diameters of 2.54 cm, 1.27 cm, 0.64 cm, 0.32 cm, and 0.16 cm. All baffle plates exhibited sharp edge holes except the 0.16 cm diameter hole with 896 holes. The percent openness of each baffle plate was nominally 10.9%, 21.9%, 43.8%, and 60.9%. The thicknesses of the plates were nominally 0.31 cm, 0.51 cm, or 0.65 cm. Table 1 provides a detailed list of the baffle plates employed and their associated characteristics. Figure 21 shows an image of each of the baffle plates.

Table 1: Baffle plates used in the study with baffle hole diameter, number of baffle holes, and baffle plate thickness shown.

Plate Label	Baffle Hole Diameter (cm)	Baffle Plate Thickness (cm)	Number of Baffle Holes	Through Area Ratio A_H/A_p
A1	2.53	0.66	7	0.434
A2	2.54	0.65	4	0.211
B1	1.27	0.66	28	0.435
B2	1.26	0.66	14	0.217
B3	1.27	0.31	7	0.109
B4	1.27	0.64	7	0.109
C1	0.64	0.65	156	0.611
C2	0.64	0.67	112	0.438
C3	0.65	0.65	57	0.233
C4	0.63	0.65	28	0.109
D1	0.32	0.51	624	0.607
D2	0.32	0.51	448	0.451
D3	0.32	0.56	224	0.225
D4	0.31	0.52	112	0.108
E1	0.16	0.50	1793	0.435
E2	0.16	0.54	896	0.220

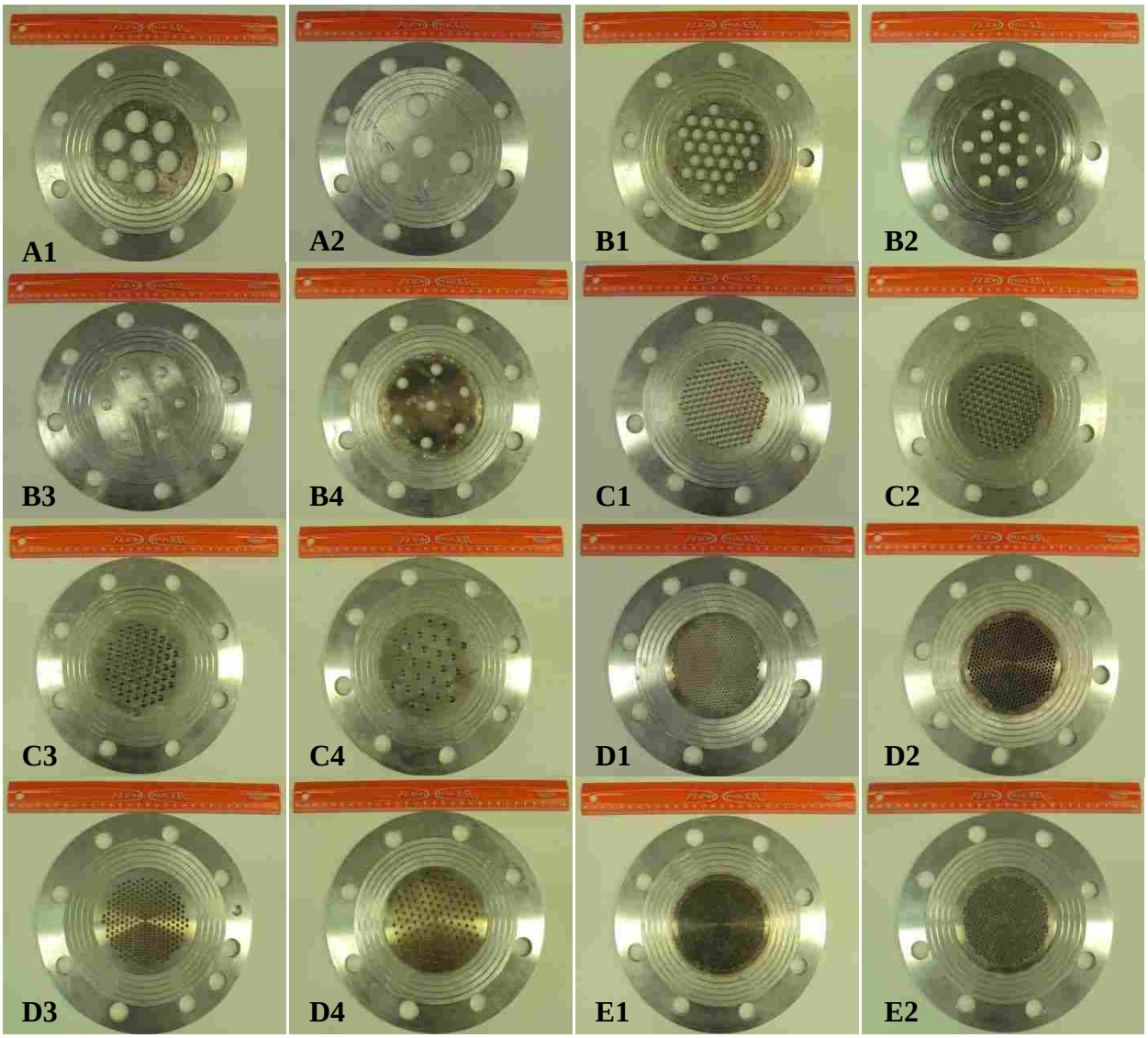

Figure 21: Photographs of the sixteen baffle plates used in the study, showing arranged in the same order as Table 1 from left to right and top to bottom.

3.3 **Instrumentation**

A single PCB Piezotronics ICP 352C68 accelerometer was used to measure the pipe wall acceleration. The sensitivity of the accelerometer was 10.2 mV/(m/s^2), the range was +/- 491 m/s^2, and the resolution was 1.5 x 10^{-3} m/s^2. The accelerometer was placed on the side of the

pipe test section three diameters downstream, for the experiment used to characterize cavitation inception and vibrations; and from three to 110 diameters downstream of the of the baffle plate, for the experiment used to characterize the attenuation of vibrations. An LD 2551 microphone and PRM 426 preamp having a sensitivity of 50 mV/Pa, with a range up to 139 dB, were used to measure sound levels. The microphone was placed three diameters downstream of the baffle plate on the side of the pipe opposite of the accelerometer.

Two Omega PX 309 static pressure transducers with ranges from 0-100 psi, and accuracy of +/- 0.25%, were placed three diameters upstream and six diameters downstream of the baffle plate. The pressure transducers were used to measure the pressure drop across the baffle plate.

Downstream of the pipe test section, an Omega FP6500 series paddlewheel with a range of 0.1-9m/s and accuracy of ±1.5%, was used to measure the flow rate in the test section. Also downstream of the test section a K-type thermocouple with accuracy of ±0.05 ^{o}C was used to measure the fluid temperature so as to determine the vapor pressure and water properties.

4 EXPERIMENTAL PROCEDURES

Two types of experiments were performed in this research. The first were experiments that characterized cavitation inception and pipe vibrations immediately downstream of the baffle plates. The second were experiments conducted to characterize the attenuation of pipe vibrations with streamwise distance. The following will discuss the measurements conducted by each experiment, followed by a discussion of the data analysis. Lastly, a section addressing the uncertainty analysis is provided.

4.1 Measurements of Cavitation Inception and Pipe Vibrations

Experiments were conducted in the cavitating and non-cavitating regimes to characterize the initiation of cavitation and the pipe wall acceleration over a range of average pipe fluid velocities from 0.35-8.5 m/s. An accelerometer and microphone were placed three diameters downstream of the baffle plate. These were used to measure the pipe wall acceleration and sound levels emitted from the pipe. Two pressure transducers were placed respectfully two and six diameters upstream and downstream of the baffle plate to measure the static pressure drop across the baffle plate, P_1-P_2. A paddle wheel was placed far downstream of the pipe test section to measure the bulk fluid flow rate. A thermocouple was placed downstream of the test section to measure the fluid temperature. The location of these instruments can be seen in Figure 17-Figure 20.

The accelerometer, pressure, noise, and flow rate data were acquired at a sample rate of 50 kHz for 5 seconds for each pipe velocity considered. A 2 Hz high pass filter and a 20 kHz low pass filter were used to filter the acceleration and microphone data. The filters were used to filter the low frequency noise that was occurring due to low frequency pipe swaying at the lower end and the resonant frequencies of the measurement devices at the high frequencies. These measurements were acquired for each of the 16 baffle plates over as large of flow speed as possible for each plate. Two independent tests were conducted for every scenario and the results were averaged. Table 2 shows the maximum variation of all the scenarios of σ, σ_v, v_H, and K_{Lp} at incipient and critical cavitation between the two independent tests that were conducted.

Table 2: The maximum variation in the two different independent tests that were conducted for every scenario for the variables that was determined at both incipient and critical cavitation as seen below.

	Incipient Cavitation	Critical Cavitation
σ_v	6.8%	4.4%
σ	4.0%	10.0%
v_H	4.6%	4.8%
K_{Lp}	7.5%	5.7%

4.2 **Data Analysis of Cavitation and Pipe Vibrations**

The measurement data collected, as described in section 4.1, were post-processed to obtain the RMS of the sound and acceleration data (A' and S') for each velocity measurement. The time averages of the pressure and flow rate measurements were also acquired for each velocity measurement.

To obtain the cavitation numbers, average baffle fluid velocity, A', and the loss coefficients at the incipient and critical points, the process that was discussed in section 2.3 and shown in Figure 12 was used and will be described here.

To determine the point of cavitation inception and critical cavitation, the rms of pipe wall acceleration, A', was plotted as a function of σ, σ_v, and v_H. Where σ is defined in equation (4.6), σ_v is defined in equation (4.10), and v_H is the baffle hole velocity.

$$\sigma = \frac{P_2 - P_v}{P_1 - P_2} \tag{4.1}$$

$$\sigma_v = \frac{P_2 - P_v}{1/2\rho v_p^2} \tag{4.2}$$

The natural logarithm of each variable was determined and the data were plotted, as illustrated for each variable in Figure 22-Figure 24. Figure 22- Figure 24 are plots that show A' versus σ, σ_v, or v_H. From plots of these nature the incipient and critical cavitation points can be determined. To do this a linear regression analysis ($y=mx+b$) was performed for each of the three linear sections of data evident in the figures, these linear sections correspond to the non-cavitating, incipient and fully cavitating regimes as discussed in section 2.3 and shown in Figure 12. The points of intersection of the three linear sections were determined to be the points of cavitation inception and critical cavitation. This method was performed for each of the two sets of data obtained for each baffle plate and the results were averaged.

The plate loss coefficient based off the average pipe velocity, K_{Lp}, (defined in equation (4.3)) was calculated at the incipient cavitation design limit using equation (4.4). σ_i is the

incipient cavitation number and σ_{vi} is also an incipient cavitation number but based off of the dynamic pressure and is defined in equation (4.5).

$$K_{Lp} = \frac{P_1 - P_2}{1/2\rho v_p^2} \tag{4.3}$$

$$K_{Lp} = \frac{\sigma_{vi}}{\sigma_i} \tag{4.4}$$

$$\sigma_v = \frac{P_2 - P_v}{1/2\rho v_{pi}^2} \tag{4.5}$$

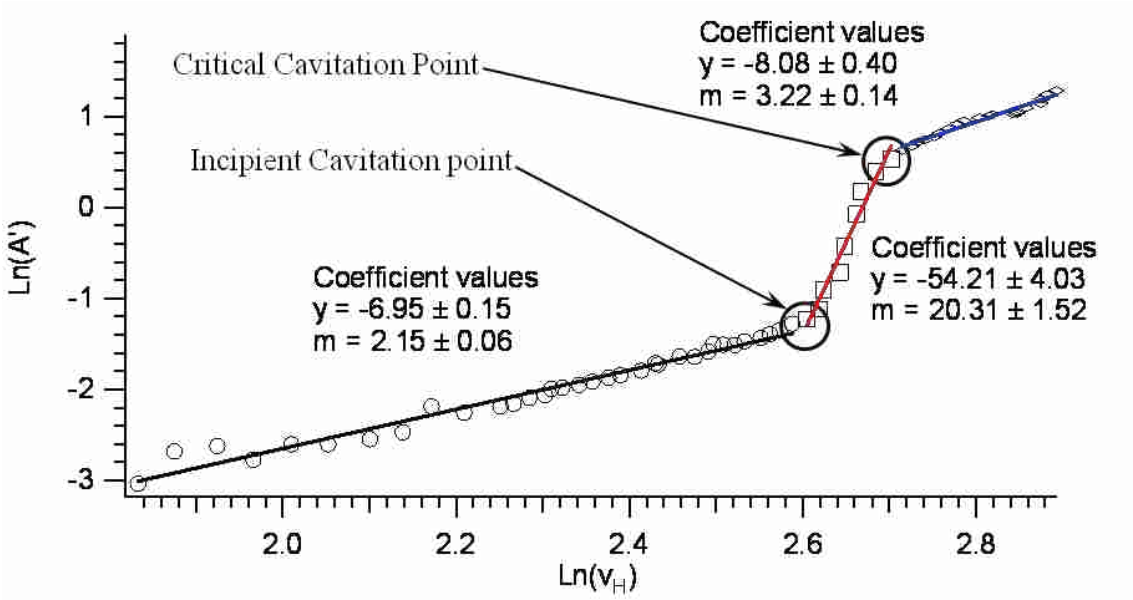

Figure 22: Ln(A') vs. Ln(v_H) used to obtain inception and critical cavitation values. Values of the coefficients *m* and *b* for the linear form *y=mx+b* are shown for each of the three linear regimes.

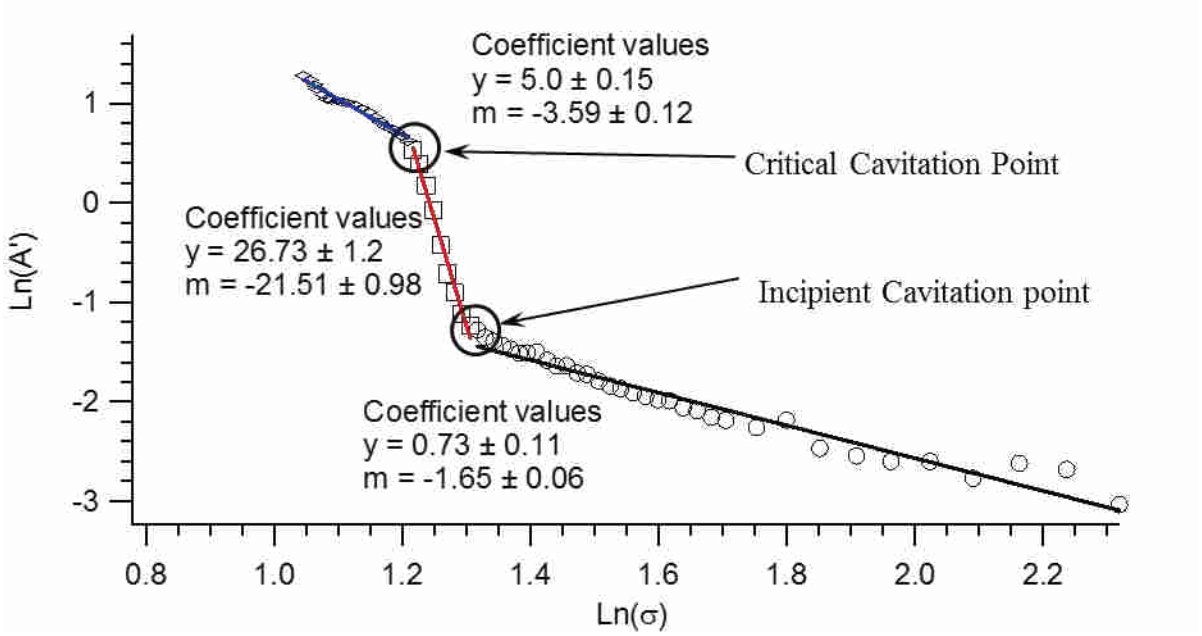

Figure 23: Ln(*A'*) vs. Ln(σ) used to obtain inception and critical cavitation values. Values of the coefficients *m* and *b* for the linear form *y=mx+b* are shown for each of the three linear regimes.

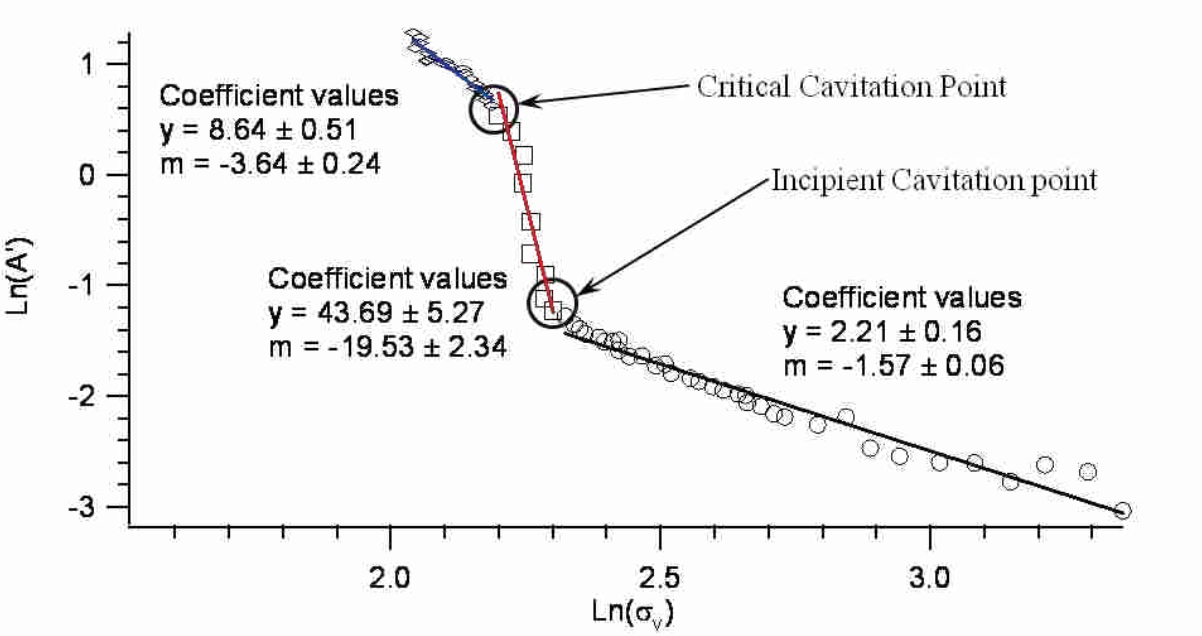

Figure 24: Ln(*A'*) vs. Ln(σ_v) used to obtain inception and critical cavitation values. Values of the coefficients *m* and *b* for the linear form *y=mx+b* are shown for each of the three linear regimes.

The inception and critical cavitation number were normalized by the size scale effect discussed in section 2.3 and were compared to the discharge coefficient as was done by Tullis [9]. The A' values at inception and critical cavitation were also normalized as shown in equation (4.6), where again d is the baffle hole diameter and v_H is the baffle hole velocity. The non-dimensionalized A', A'^*, was compared to the thickness to baffle hole diameter, t/d, the through area ratio, A_H/A_p, and the cavitation number, σ. Empirical models were then developed for the cavitation number and A', at the points of inception and critical cavitation.

$$A'^* = \frac{A' d}{v_H^2} \tag{4.6}$$

The loss coefficient based on the baffle hole velocity (K_{LH}), as shown in equation (4.7) and can be calculated from K_{Lp} as shown in equation (4.3) and is determined from equation (4.8), was normalized by the theoretical attached loss coefficient model as was developed in 2.2.2 and shown in equation (4.9). This ratio (K_L/K_{LA}) was then evaluated as a function of the plate thickness to diameter ratio, t/d, and the through area ratio, A_H/A_p. An empirical model to predict the loss coefficient based upon geometric variables was then developed.

$$K_{LH} = \frac{P_1 - P_2}{1/2 \rho v_H^2} \tag{4.7}$$

$$K_{LH} = K_{Lp} \left(\frac{A_H}{A_p} \right)^2 \tag{4.8}$$

$$K_{LA} = \left(1 - 2\left(\frac{A_p}{A_H}\right) + 2\left(\frac{A_p}{A_H}\right)^2\left(1 - \frac{1}{\alpha} + \frac{1}{2\alpha^2}\right)\right)\left(\frac{A_H}{A_p}\right)^2 \quad (4.9)$$

4.3 **Measurements of Attenuation of Pipe Vibrations**

Experiments were also conducted in both the cavitating and non-cavitating regimes to characterize the attenuation downstream of the baffle plates. A total of 14 baffle plates were tested for this part of the study. Due to the limitations on length of pipe, two 6.1 m long, 10.16 cm diameter, pipes were flanged together to make up the entire test section.

Accelerometers were mounted on the wall of the pipe at locations ranging from 3-110 diameters downstream, *x/D*, of the baffle plate. The pressure drop across the baffle plate was measured using two pressure transducers that were placed three and six diameters up and downstream of the baffle plate. A paddle wheel was placed far downstream of the pipe test section to measure the liquid flow rate.

The pipe wall acceleration (at 26 *x/D* locations from 3-110), pressure drop, and average pipe fluid velocity measurements were taken for 2-4 average pipe velocities ranging from 0.6-6.6 m/s. The variation of velocity measurement was to allow for measurements in both non-cavitating and cavitating regimes. The data were collected at a sample rate of 50 kHz for 5 seconds for each pipe velocity measurement and *x*/D location. A 2 Hz high pass filter and a 20 kHz low pass filter were used to filter the acceleration and microphone data. The filters were used to filter the low frequency noise that was occurring due to pipe swaying and the resonant frequencies of the measurement devices.

4.4 **Data Analysis of Attenuation of Pipe Vibrations**

The attenuation measurement data were post-processed to obtain the RMS of the acceleration data (A') for each velocity measurement. The time averages of the flow rate measurements were also taken for each velocity measurement.

A non-dimensionalized A' value, $A_2'^*$, as shown in equation (4.10), was plotted versus x/D and a double exponential form of a curve fitting function was applied to the data. When the value $A_2'^*$ decreased to 1.5 times the no baffle plate value of $A_2'^*$ this point was determined to be the point when the vibrations had attenuated or decayed.

$$A_2'^* = \frac{A' D}{v_p^2} \tag{4.10}$$

Figure 25 illustrates $A_2'^*$ versus x/D for a representative baffle plate at four different velocities. From plots of this nature the point of attenuation of vibrations can be illustrated. The **x** markings show the attenuation point for these curves, determined by $A_2'^*$ reaching 1.5 times the no baffle plate $A_2'^*$. As can be seen at a $x/D = 3$ the vibrations decreases to an asymptotic value, which is the non-baffle plate vibration levels.

4.5 **Uncertainty Analysis**

Uncertainties in the measurements and variables described in section 4.3 are now discussed. Several sources of uncertainty exists which include the uncertainty in the regression analysis (to find σ_i, σ_c, σ_{vi}, σ_{vc}, v_{Hi}, and v_{Hc}), in the calculation of K_{Lp}, A_H/A_p, and t/d and the measurements taken. First the uncertainty in the regression analysis to find σ_i, σ_c, σ_{vi}, σ_{vc}, v_{Hi},

and v_{Hc} will be discussed. The measurement uncertainty will then be discussed. Concluding this section will be a discussion of the uncertainty in the calculation of K_{Lp}, A_H/A_p, and t/d.

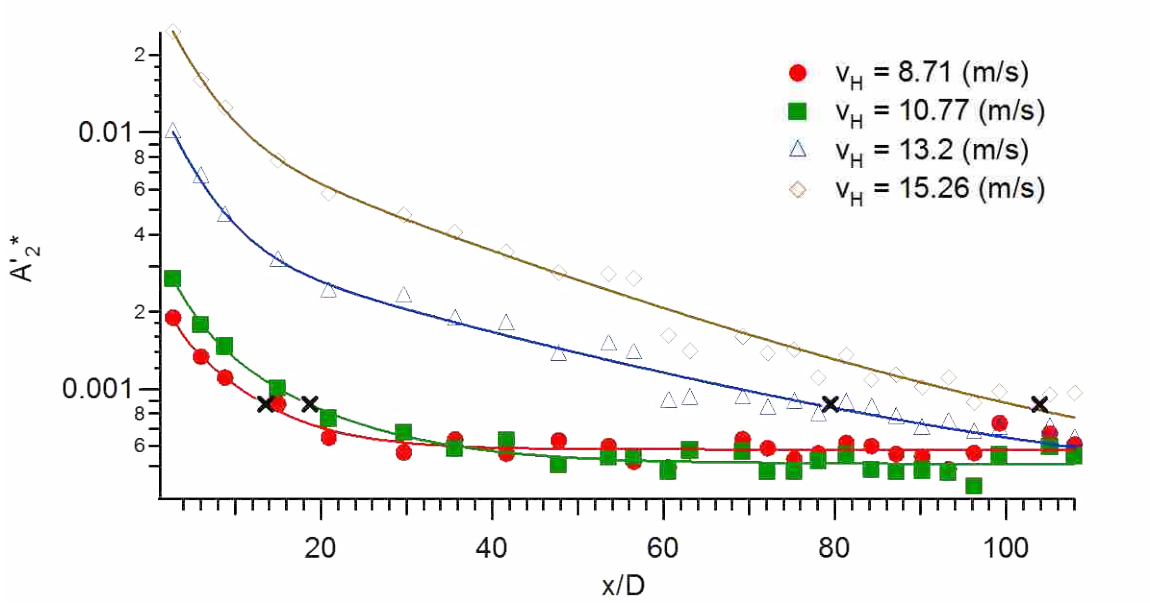

Figure 25: A representative plot of $A_2^{'*}$ vs. x/D for four different baffle hole velocities for one baffle plate. The x markings indicate 1.5 time the no baffle plate vibrations.

4.5.1 Regression Analysis Uncertainty

The uncertainty of the points, σ_i, σ_c, σ_{vi}, σ_{vc}, v_{Hi}, and v_{Hc}, obtained from the regression analysis (discussed in section 4.2) is calculated from equation (4.11) [20]. This is the error associated with the x-axis variable (being σ_i, σ_c, σ_{vi}, σ_{vc}, v_{Hi}, or v_{Hc}) that was used to create the regression line, where $\hat{X}$ is the regression value for a given A' value and X is the measured value at that point. The i and j's represent the two different lines used to find the intersecting point. The variables N and M are the respected number of data points used in the regression analysis for each line [20]. The number of data points is subtracted by two because there are two constants that were used to produce the regression line, m and b ($mx+b$).

$$u_x = \pm\sqrt{\frac{\sum_{i=1}^{N}\left(X_i - \hat{X}_i\right)^2}{N-2} + \frac{\sum_{j=1}^{M}\left(X_j - \hat{X}_j\right)^2}{M-2}} \tag{4.11}$$

Table 3 shows the uncertainty determined using the above method for the cavitation numbers and baffle hole fluid velocity at incipient and critical cavitation. This lists the maximum, minimum, and average uncertainties calculated. This shows that from the regression analysis all uncertainties are below 25%, where all the average uncertainties of all the variables are below 12%.

Table 3: Uncertainty in determining design limits

	Average Incipient Cavitation	Min. Incipient Cavitation	Max. Incipient Cavitation	Average Critical Cavitation	Min. Critical Cavitation	Max. Critical Cavitation
v_H	3.6%	2%	8.3%	1.9%	1%	2.5%
σ	10.4%	5.3%	18.4%	3.3%	1.6%	6.2%
σ_v	11.1%	5.3%	22.3%	3.4%	2.4%	4.8%

4.5.2 Measurement Uncertainty

Measurements were acquired for the pressure, pipe wall acceleration, flow rate, temperature, plate thickness, and baffle hole diameter. Each of these measurements had uncertainty associated with it cause by the accuracy of the measurement devices. The uncertainty in the pressure measurements was limited to the instrument accuracy of ±0.25%. The accuracy of the accelerometer was ±7.5 x 10^{-4} m/s^2. The baffle hole diameter and plate thickness

uncertainty was ±5 x 10^{-5} m. The Uncertainty of the thermocouple was ±5 x 10^{-2} ^{o}C. The uncertainty of the flow meter was ±1.5%.

4.5.3 Calculated Variables Uncertainty

The uncertainty in a calculated variable *R* is a function of the uncertainty of the variables that *R* is a function of as can be seen in equations (4.12) and (4.13), where u_R is the uncertainty of *R* and u_x is the uncertainty of *x* [21]. To find the total uncertainty in *R*, equations (4.14) and (4.15) where used [21]. This method was used in finding the overall uncertainty of K_{Lp}, A_H/A_p, and *t/d* and will be discussed below.

$$R = f(x_1, x_2, \dots, x_L) \tag{4.12}$$

$$u_R = f(u_{x_1}, u_{x_2}, \dots, u_{x_L}) \tag{4.13}$$

$$\theta_i = \frac{\partial R}{\partial x_i} \quad i = 1,2, \dots, L \tag{4.14}$$

$$u_R = \pm \sqrt{\sum_{i=1}^{L} \left(\theta_i u_{x_i}\right)^2} \tag{4.15}$$

The value of K_{Lp} is a function of P_1, P_2, v_p, and ρ as shown in equation (4.16). Using both equation (4.14) and (4.15) an equation for finding $u_{K_{Lp}}$ can be obtained and is shown in equation (4.17). Note that in equation (4.17) there is an additional term u_E. This is the standard deviation of K_{Lp} for the non-cavitating regime. This was an average of ±2.4% for all the baffle plates. The total uncertainty of K_L was an average of ±4.1% for all the baffle plates used with a maximum and minimum uncertainty of ±5.6% and ±3.3%.

$$K_{Lp} = \frac{P_1 - P_2}{1/2\rho v_p^2} \tag{4.16}$$

$$\begin{aligned} u_{K_{Lp}} &= \pm\sqrt{\left(\frac{\partial K_{Lp}}{\partial P_1}u_{P_1}\right)^2 + \left(\frac{\partial K_{Lp}}{\partial P_2}u_{P_2}\right)^2 + \left(\frac{\partial K_{Lp}}{\partial v_p}u_{v_p}\right)^2 + \left(\frac{\partial K_{Lp}}{\partial \rho}u_\rho\right)^2 + u_E^2} \\ &= \pm 2\sqrt{\frac{u_{P_1}}{\rho^2 v_p^4} + \frac{u_{P_2}}{\rho^2 v_p^4} + \left(\frac{2(P_1 - P_2)u_{v_p}}{\rho\, v_p^3}\right)^2 + \left(\frac{(P_1 - P_2)u_\rho}{\rho^2\, v_p^2}\right)^2 + u_E^2} \end{aligned} \tag{4.17}$$

The uncertainty of A_H/A_p is a function of the uncertainty of the baffle hole diameter, d, and the diameter of the pipe, D. Using both equations (4.14) and (4.15) an equation for finding $u_{AH/Ap}$ can be obtained and is shown in equation (4.18). The average uncertainty of all the baffle plates for A_H/A_p is about ±0.1%.

$$u_{AH/Ap} = \pm\sqrt{\left(\frac{\partial \frac{A_H}{A_p}}{\partial d}u_d\right)^2 + \left(\frac{\partial \frac{A_H}{A_p}}{\partial D}u_D\right)^2} = \pm 2\sqrt{\left(\frac{dnu_d}{D^2}\right)^2 + \left(\frac{d^2 n u_D}{D^3}\right)^2} \tag{4.18}$$

The uncertainty of *t/d* is a function of the uncertainty of the baffle hole diameter, *d*, and the baffle plate thickness, *t*. Using both equations (4.14) and (4.15) an equation for finding $u_{t/d}$ can be obtained and is shown in equation (4.19). The average uncertainty of all the baffle plates for *t/d* is about ±0.015%.

$$u_{t/d} = \pm\sqrt{\left(\frac{\partial \frac{t}{d}}{\partial t}u_t\right)^2 + \left(\frac{\partial \frac{t}{d}}{\partial d}u_d\right)^2} = \pm\sqrt{\left(\frac{u_t}{d}\right)^2 + \left(\frac{tu_d}{d^2}\right)^2} \tag{4.19}$$

5 CHARACTERIZED RESULTS

This chapter discusses the characterized results of the experiments that were performed and discussed in chapter 4. The results are divided into four sections. The first three sections will discuss the general trends that occur due to the influencing variables. Specifically, these sections will address the loss coefficient, cavitation inception, A' levels, and attenuation of vibrations. The last section provides a summary of the results that are presented in the previous sections.

5.1 Baffle Loss Coefficient

The loss coefficient is a significant variable when considering cavitation and flow induced pipe vibrations. This is because the loss of pressure across a baffle plate is due to energy being converted into other forms. These other forms of energy are thermal, acoustical, internal (change of phase, from liquid to vapor for cavitation), and kinetic energy of the pipe wall (vibrations). For this reason the baffle plate loss coefficient was explored in this work and the results are discussed below.

Plotted in Figure 26 is the loss coefficient, K_{LH}, versus the through area ratio (openness) for the 16 baffle plates utilized. Data from Testud et. al. [13] are also shown for comparison. Also plotted are two theoretical models that were developed from an integral analysis of a sudden contraction followed by a sudden expansion as presented in section 2.2. The K_{LH} data shown corresponds to a flow velocity just prior to the point of cavitation inception, although K_{LH}

is nominally constant prior this point. The two baffle plates that had through area ratios, A_H/A_p = 60.9% (C4 and D4 in Table 1) did not cavitate at any speed so the K_{LH} values for these plates correspond to the maximum flow rate measured. K_{LA} was discussed in section 2.2.2 and is given again in equation (5.1). This is a model that assumes that the baffle plate is thick enough for the flow to reattach after the formation of the vena-contracta. K_{LD} was discussed in section 2.2.1 and is given again in equation (5.2). It is based on a model that assumes the baffle plate is thin so that the flow does not reattach. It can be seen from Figure 26 that the data follow the trends of the two models and are bound by them as was expected. α is a the ratio of the jet from the vena-contracta, v_j, over the baffle hole velocity, v_H. For K_{LA}, $\alpha = 0.72$ and for K_{LD}, $\alpha = 0.61$. The value 0.61 is the theoretical value for a sharp edge orifice for a gas to a free space exit [13]. For a sudden contraction area the α value varies from 0.62 to a value of 1, which would be valid for a thick plate. The value of 0.72 was selected due to it being the best fit to the lower limit of the data.

$$K_{LA} = \left(1 - 2\left(\frac{A_p}{A_H}\right) + 2\left(\frac{A_p}{A_H}\right)^2\left(1 - \frac{1}{\alpha} + \frac{1}{2\alpha^2}\right)\right)\left(\frac{A_H}{A_p}\right)^2 \tag{5.1}$$

$$K_{LD} = \left(\left(\frac{A_p}{A_H}\right)\frac{1}{\alpha} - 1\right)^2\left(\frac{A_H}{A_p}\right)^2 \tag{5.2}$$

The spread between the two models is further illustrated in Figure 27 where K_{LH} as a function of the thickness to baffle hole diameter ratio, *t/d*, is shown. This data shows that for a given through area ratio, K_{LH} decreases with increased *t/d* until *t*/d ≈ 1.5-2.0 where K_{LH} then slightly increases with increasing *t/d*. The large decrease of K_{LH} in the *t/d* < 1 range illustrates

that the loss coefficient is approaching the theoretical thick plate model and this shows that with baffle plates of *t/d* ratios greater than one the theoretical thick plate model accurately predicts the loss coefficient. The slight increase in K_{LH} above *t/d*=1.5-2.0 is believed to be due to frictional losses within the baffle holes.

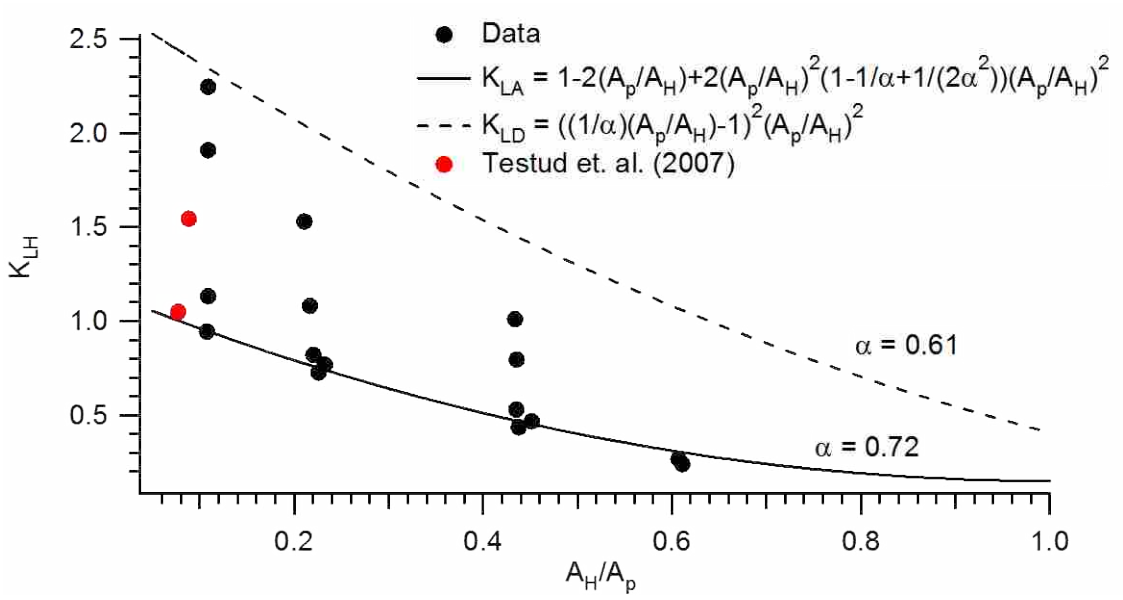

Figure 26: Loss coefficient, K_{LH}, vs. the total through area ratio, A_H/A_p, for 16 baffle plates. Included is a theoretical attached model, K_{LA}, and a theoretical detached model, K_{LD}. Data from Testud et. al. is also included for comparison.

The two figures together show that the loss coefficient is dependent upon the through area ratio as was expected but also upon the ratio of thickness of the baffle plate to the diameter of the baffle hole. It also shows that the two theoretical models are only accurate for a range of plate thicknesses. It is also worth noting that by holding A_H/A_p constant, the plates with larger *t/d* ratios exhibit a larger numbers of baffle holes. This fact illustrates that increased number of baffle holes causes a suppression of the pressure loss that is occurring even when the total flow area remains constant.

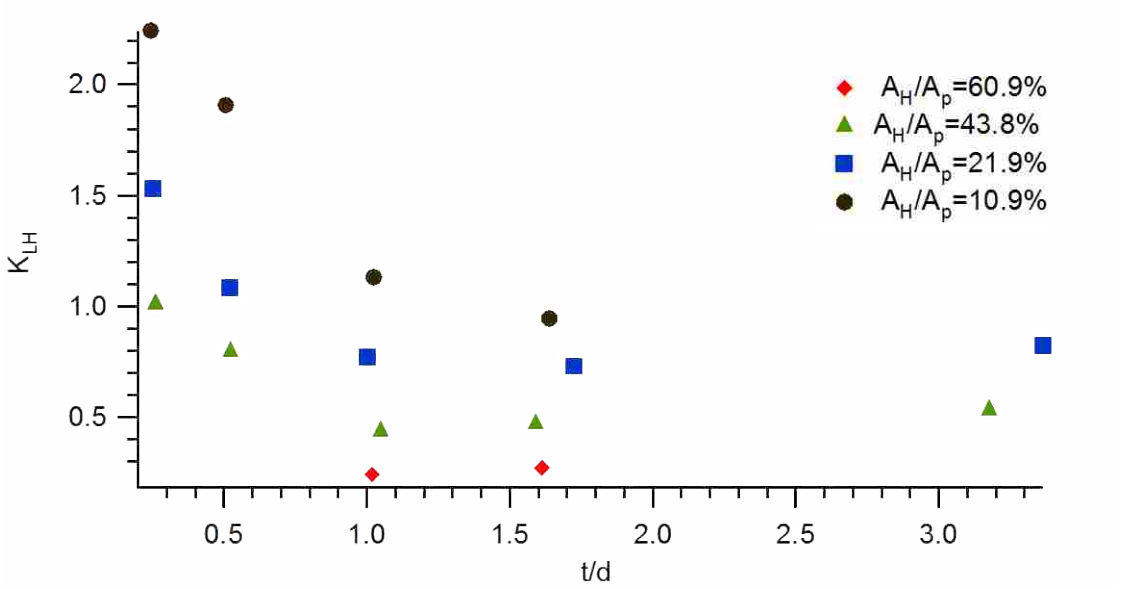

Figure 27: Loss coefficient, K_{LH}, vs. the thickness ratio, *t/d*, for 16 baffle plates and four area ratios as shown in the legend.

5.2 Characterization of Vibrations and Incipient Cavitation

Figure 28 provides a representative plot of the pipe wall acceleration, characterized by A', versus the average baffle hole velocity for five different baffle plates with varying thickness to diameter ratios, *t/d*, and a fixed through area ratio of nominally 43.8%. These measurements of acceleration were obtained at three pipe diameters downstream from the baffle plate. It can be seen that from this figure that each baffle plate has similar trends. The A' levels gradually increase in a power-law form with the baffle hole velocity, v_H, until a definite change in slope occurs. This initial regime is where the flow is non-cavitating and the pipe wall vibration is caused by the turbulence in the flow. The slopes of these lines are similar for all baffle plates. From the first influx point the A' levels increase dramatically with increasing v_H until a second inflection point occurs. This essentially linear region is when the flow is starting to cavitate. The amount of cavitation increases with v_H causing A' to also increase. From the second

inflection point and above, the flow is fully cavitating and the A' levels again increase gradually with a power-law dependence on v_H. The slope in this region is similar for all baffle plates.

The two inflection points observed in the data correspond to the inception and critical cavitation values. The data of Figure 28 also reveals that in general the A' level increases with decreasing *t/d*, both within the turbulent regime and the cavitating regime. It is also observed that cavitation inception also occurs at higher average baffle hole velocities with increased *t/d*. The velocity at cavitation inception for t/d=0.25 is about an order of magnitude greater than the velocity at inception for t/d=3.3.

Figure 29 is a plot of A' versus the average baffle hole velocity for 5 different thickness to diameter ratios, *t/d*, and a fixed through area ratio, A_H/A_p, of nominally 21.9%. The slight variation in A_H/A_p is due to it being impossible to create plates of constant A_H/A_p for small numbers of baffle holes. The data of this figure reveals that for increasing in *t/d*, the A' levels decrease and that cavitation inception occurs at higher velocities.

Comparing the results of both Figure 28 and Figure 29 to that of the previous section which addressed the loss coefficient reveals that decreasing *t/d* yields increases in both the loss coefficient and the A'. Thus, the A' levels and the loss coefficient show similar dependence on the flow and geometric variables. The added loss that occurs at smaller *t/d* results in enhanced energy transfer to the pipe wall in the form of vibrations. Cavitation is also suppressed with increasing *t/d* such that the inception point is shifted to higher velocities by nominally 48% between smallest and largest *t/d*. Again, this can be attributed to these plates having lower loss coefficients which result in smaller pressure drops.

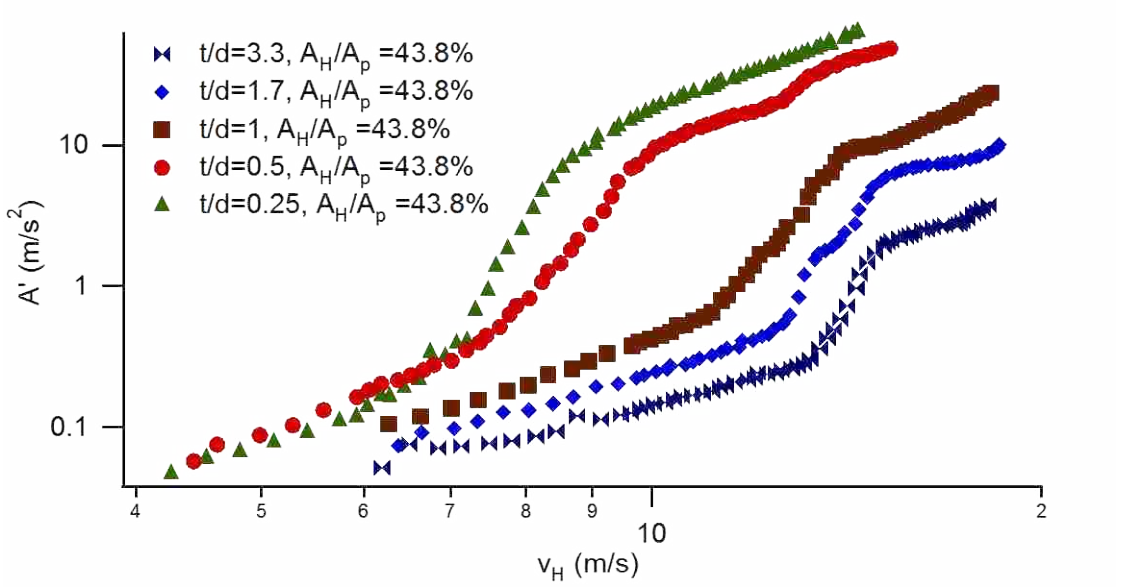

Figure 28: *A′* vs. average baffle hole velocity, v_H, for five baffle plates of constant through area (A_H/A_p=0.438) and five different *t/d* ratios as shown in the legend.

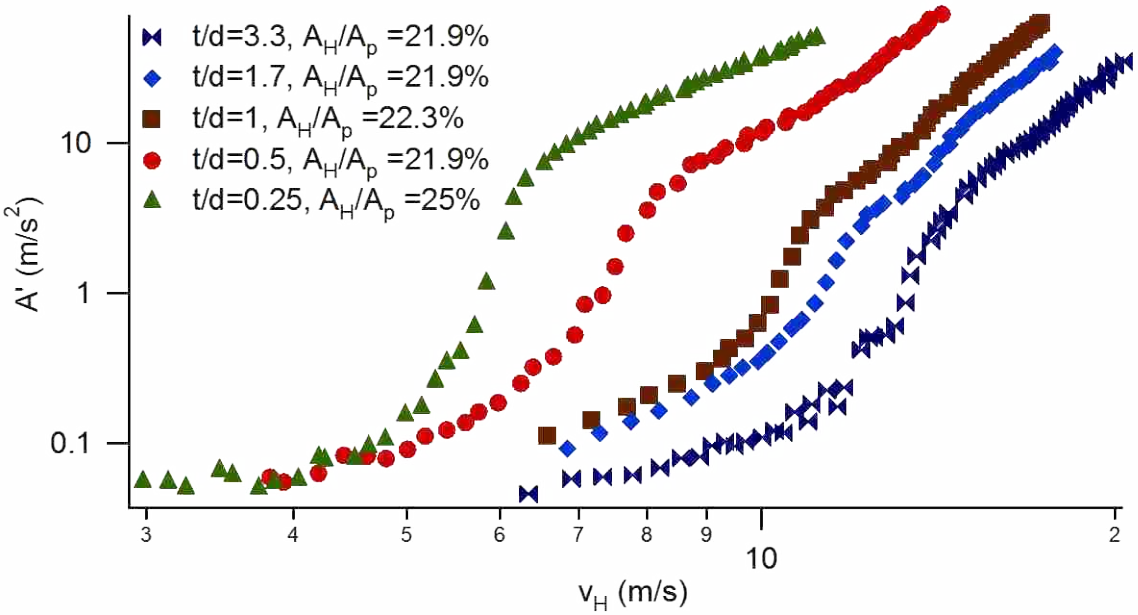

Figure 29: *A′* vs. average baffle hole velocity, v_H, for five baffle plates of nominally constant through area (A_H/A_p=0.219) and five different *t/d* ratios as shown in the legend.

Figure 30 provides a representative plot of A' versus the average baffle hole velocity for four different baffle plates through area ratios of A_H/A_p = 10.9, 21.9, 43.8, and 60.9%, and at a fixed thickness to diameter ratio of t/d = 1.7. These data show that the vibration levels increase with decreased through area ratio, and this is most pronounced in the cavitation regime. Between the smallest to largest through area ratio the vibration levels have an order of magnitude difference. It is also shown that cavitation inception occurs at higher velocities with increased through area ratios to where cavitation occurs at a velocity nominally 18% higher for A_H/A_p = 43.8% compared to A_H/A_p = 10.9% . The A_H/A_p = 60.9% baffle plate was never observed to experience cavitation.

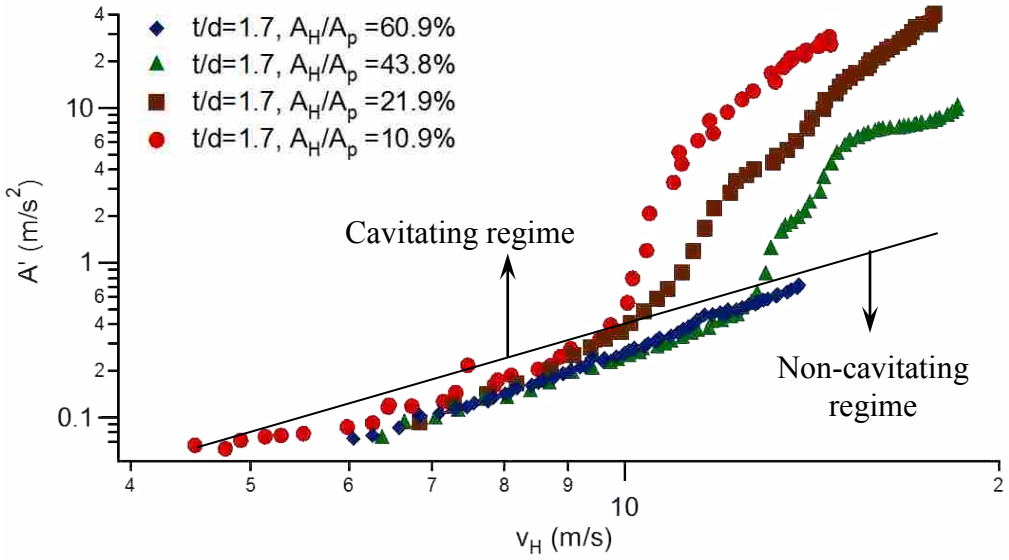

Figure 30: A' vs. average baffle hole velocity, v_H, for four baffle plates of constant thickness ratio (t/d=1.7) and four different through areas (A_H/A_p) as shown in the legend.

Figure 31 is a plot of A' versus the average baffle hole velocity for four different baffle plates with a constant t/d = 1 and varying A_H/A_p. This plot reveals that again with decreased through area ratio vibration levels increase and cavitation inception occurs at lower velocities.

Comparing the results of Figure 30 and Figure 31 to that of the loss coefficient data, where the loss coefficient decreased with increased through area ratio, shows that the A' levels again are correlated with this. Namely, with decreased loss the vibration levels also decrease, and cavitation suppression also correlates with the loss coefficient decreasing.

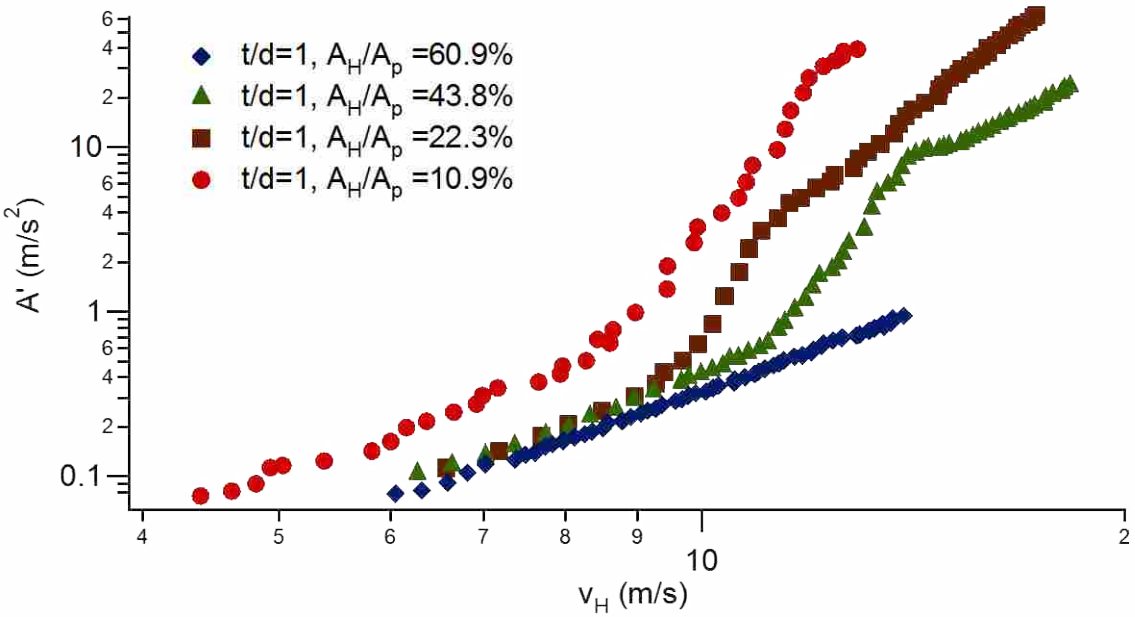

Figure 31: A' vs. average baffle hole velocity, v_H, for four baffle plates of constant thickness ratio (t/d=1) and four different through areas (A_H/A_p) as shown in the legend.

Figure 32 provides a representative plot of A' as a function of the cavitation number, σ, for five baffle plates with constant through area ratio, A_H/A_p, of 21.9% and at varying thickness ratios. σ is defined and discussed in section 2.3 and is shown again in equation (5.3). Due to the nature in which σ is defined, it decreases with increased flow rates. Thus, the cavitation intensity increases with decreased σ. As can be seen from the data of Figure 32, it appears very similar to Figure 29, except it is nearly a mirror image of it. Starting at high σ values, A' levels increase gradually with decreasing σ until the point of cavitation inception. This is the non-cavitating

regime where the pipe vibration is dominated by turbulent flow. As can be seen, the slopes of the A' versus σ data in this regions for each baffle plate are nearly the same. As σ decreases farther up to the point of critical cavitation is the region where cavitation is developing. In this region A' levels are dramatically increasing with decreased σ. The large changes in A' are due to cavitation enhancement, which causes much greater vibration then the non-cavitating turbulent dominated regime. From the point of critical cavitation, as σ decreases, the A' levels again only increasing gradually with decreasing σ. This is the fully cavitating regime. The slope of the A' versus σ data in this region for all baffle plates is almost the same. The incipient cavitation number ranges from 3.5 at a high end down to 2 at the low end.

$$\sigma = \frac{P_2 - P_v}{P_1 - P_2} \tag{5.3}$$

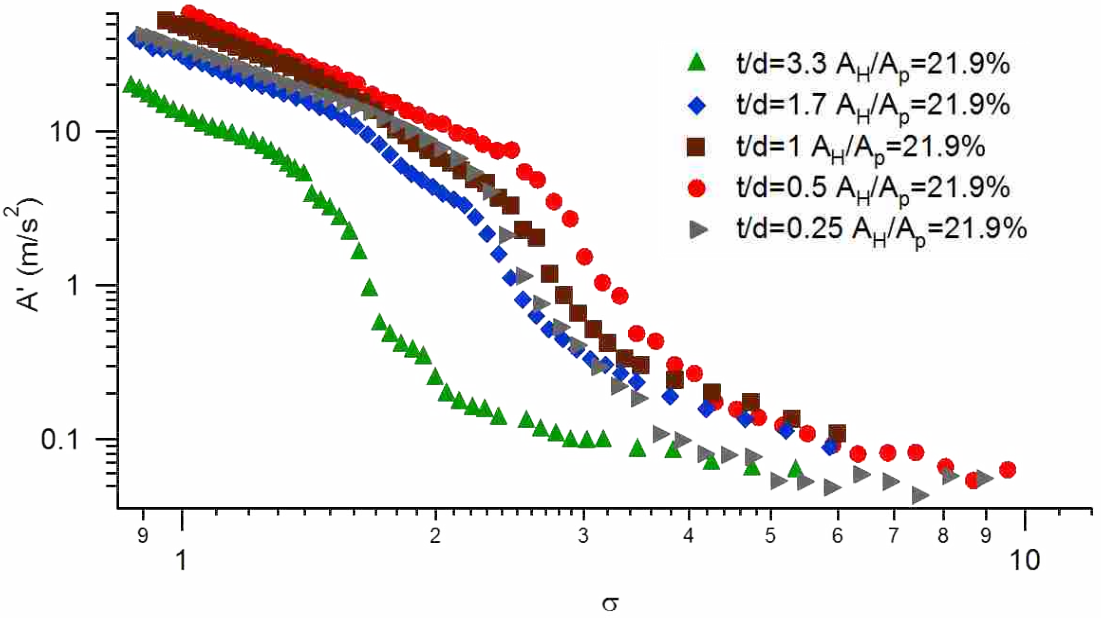

Figure 32: A' vs. the cavitation number, σ, for five baffle plates of constant through area (A_H/A_p=0.219) and five different thickness ratios as shown in the legend.

Consistent with Figure 28, the data of Figure 32 shows that A' levels generally increase with decreasing t/d ratio at fixed A_H/A_p and σ, with exception of the plate with $t/d = 0.25$. The variation with this plate is cause by the size scaling effect of the cavitation number σ. Figures of this nature were generated for all scenarios considered and the data shown is representative of the overall behaviors observed.

In Figure 33 the cavitation number at the point of cavitation inception, σ_i, is plotted versus t/d for the 14 different baffle plates where cavitation was occurring. The data are denoted by different markers for the three different area ratios (10.9%, 21.9%, and 43.8%). This figure reveals that for increased A_H/A_p cavitation inception occurs at increased cavitation numbers. This illustrates that with increased A_H/A_p cavitation is suppressed and occurs at higher cavitation numbers. This data also shows that σ_i increases with increased t/d up to about $t/d \approx 0.5$-1.0, where σ_i then decreases. Thus, the data shows the point of cavitation inception is dependent upon both A_H/A_p and t/d.

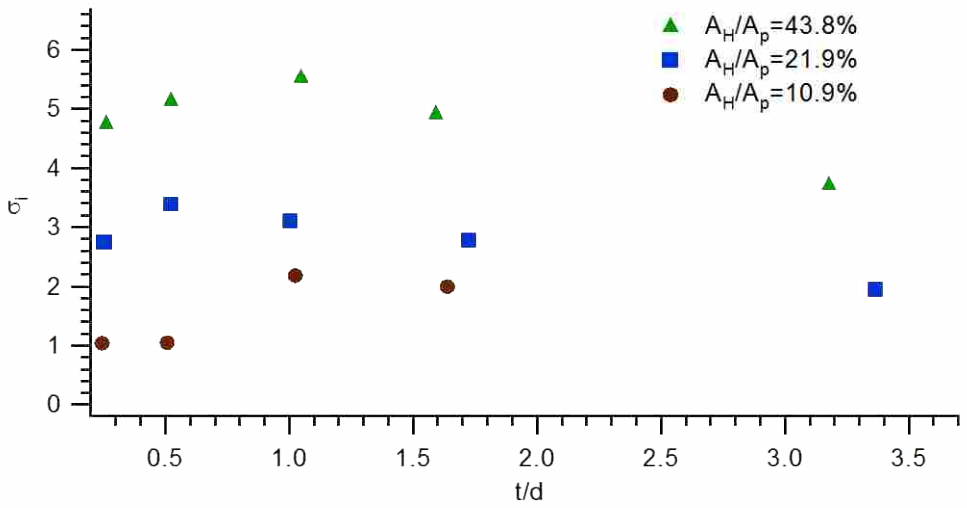

Figure 33: Incipient cavitation number vs. *t/d* for 14 baffle plates and three different through area ratios.

Figure 34 is a plot of the incipient cavitation number, σ_i, versus the through area ratio, A_H/A_p, for 14 baffle plates with five varying thickness to diameter ratios, *t/d*. This data shows that the relationship between the cavitation number at inception is nearly linear with through area ratio. For all *t/d* ratios, increased through area ratio results in the onset of cavitation occurring at higher cavitation numbers.

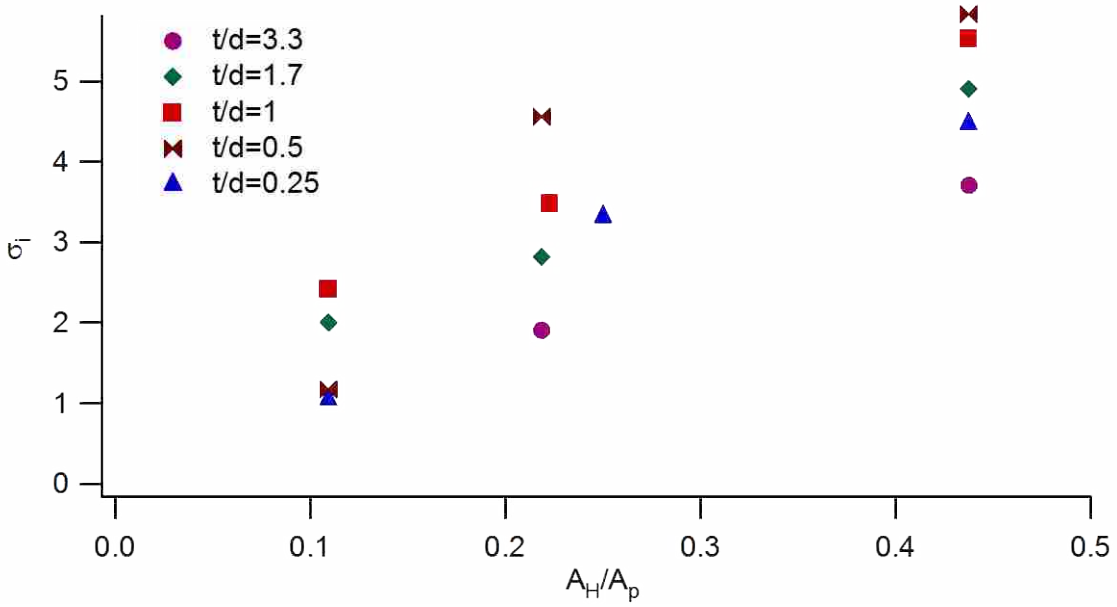

Figure 34: Incipient cavitation number vs. A_H/A_p for 14 baffle plates and five different *t/d* ratios.

Comparing the results of Figure 33 and Figure 34 with that of the loss coefficient (Figure 26 and Figure 27) reveals that σ_i exhibits an inverse relation to the loss coefficient. The loss coefficient decreased with increasing *t*/d until $t/d \approx 1$, after which it then slightly increased with increasing *t*/d due to friction. Conversely, the point of cavitation inception occurs at increasing cavitation numbers with increasing *t*/d, until $t/d \approx 1$, where σ_i then decreases with further increases in *t/d*. The loss coefficient also decreases with increasing A_H/A_p, whereas the point of

cavitation inception occurs at increasing cavitation numbers with increasing A_H/A_p. This shows that cavitation inception exhibits strong dependence upon the loss coefficient.

5.3 **Characterized Attenuated Vibrations**

The measurements and results discussed above for the A' levels were all obtained at a measurement location three diameters downstream of the baffle plate. Because the vibrations caused from the turbulent and cavitation effects of the baffle plate are greater near the plate, the vibration levels will decrease with increased distance from the plate. The vibration levels eventually attenuate to a no baffle plate level, which is caused by only fully-developed turbulent flow through a pipe. It has been shown that the no baffle plate A' level scales with the pipe velocity squared [8,7,6,5]. To understand how the pipe wall vibration levels attenuate with downstream distance, experiments were performed to characterize the A' levels with increased distanced to pipe diameters, *x/D*, in the streamwise direction. Details of this were given in section 4.3 and 4.4. The results from this portion of the experimental program are presented below.

Figure 35 shows the decay of $A_2'^*$ (defined in equation (5.4)) as a function of *x/D* for the baffle plate C4 (see Table 1). The baffle plate had 28 holes with diameters of 0.634 cm. Results are shown at four different average baffle hole velocities, v_H, as shown in the legend. Open markers indicate that cavitation is occurring for the corresponding velocity and closed markers correspond to the non-cavitation regime. From this data it can be seen that when cavitation is not occurring, the $A_2'^*$ values attenuate to the no baffle plate level at about 20 diameters downstream. However, when cavitation is occurring, $A_2'^*$ attenuates at increasing *x/D* locations with increasing

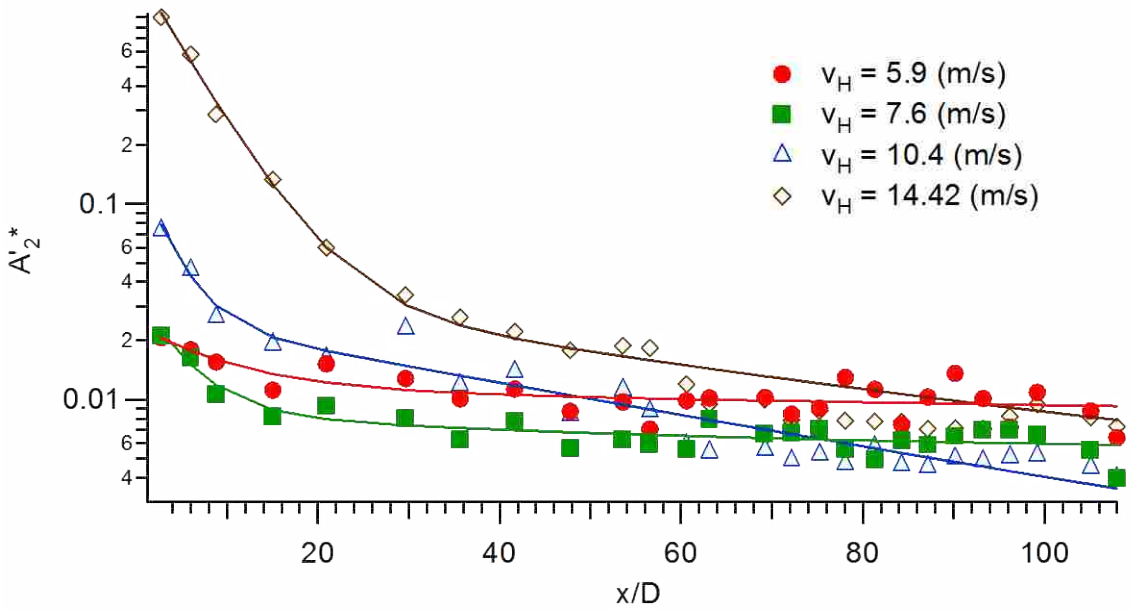

Figure 35: $A_2^{'*}$ vs. *x/D* for the baffle plate with a hole diameter of 0.634 cm and 28 holes and at four different average baffle hole velocities as shown in the legend. Open markers indicate that cavitation is occurring, and closed markers correspond to the non-cavitating regime.

v_H as was expected. This is because with increased flow rate the pressure recovery takes longer to occur so the cavitation bubbles carry farther downstream before they collapse. This causes the vibrations, caused by cavitation, to carry farther downstream.

$$A_2^{'*} = \frac{A^{'} D}{v_p^2} \tag{5.4}$$

Figure 36 provides $A_2^{'*}$ as a function of *x/D* for a baffle plate with 112 holes of 0.634 cm diameter (defined as C2 in Table 1) at four different baffle hole velocities, v_H. Again, the closed markings indicate non-cavitating flow and the open markings indicate the flow is cavitating. Similar to baffle plate C4, shows that when cavitation is not occurring, $A_2^{'*}$ values attenuate at nominally 20 diameters downstream. However, when cavitation is occurring, $A_2^{'*}$ again

attenuates at increasing *x/D* locations with increasing v_H. Data of this nature was obtained for all baffle plates and the data of Figure 35 and Figure 36 is representative of the generally observed behavior.

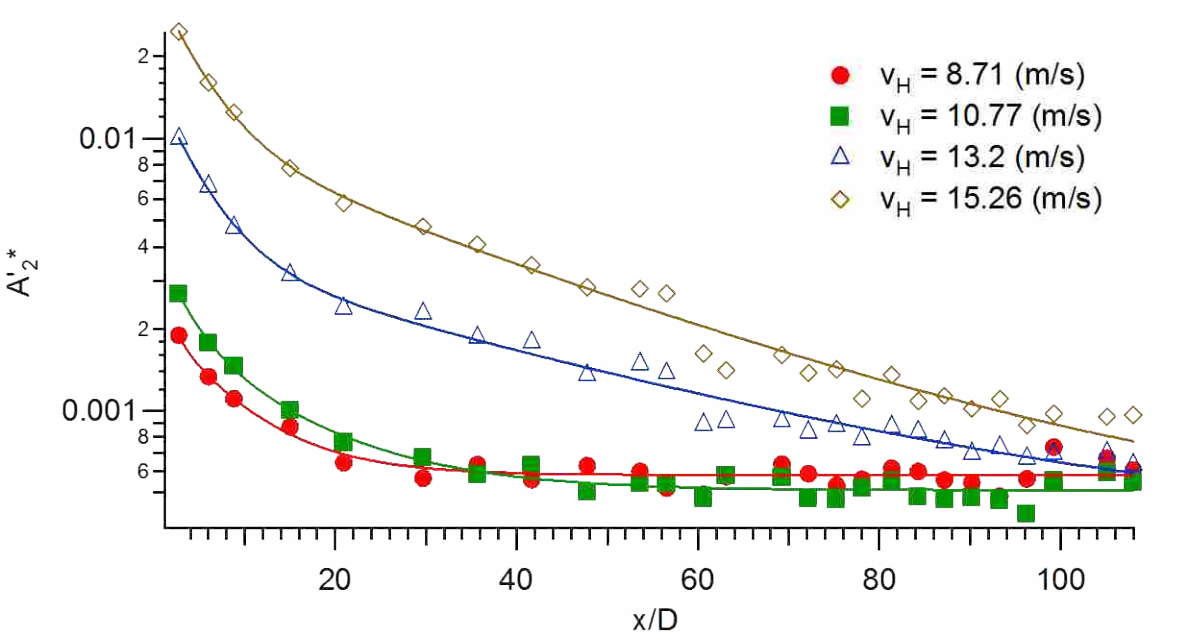

Figure 36: $A_2^{'*}$ vs. *x/D* for the baffle plate with a hole diameter of 0.634 cm and 112 holes and at four different average baffle hole velocities as shown in the legend. Open markers indicate that cavitation is occurring, and closed markers correspond to the non-cavitating regime.

Figure 37 is a plot of $A_2^{'*}$ versus *x/D* for five baffle plates (being A1, B1, C2, D2, and E1 of Table 1) at a nominal baffle hole velocity of v_H = 10.7 m/s all with a through area ratio of A_H/A_p = 43.8%. The closed markings indicate the flow is not cavitating and the open markings indicate cavitation is present. This figure reveals that as the baffle hole diameter increases, the attenuation of vibrations occur at increased normalized distance, *x/D*. This is likely due to the fact that for decreased baffle hole diameter the number of holes increases, which in turn allows for more interacting of the jets. As was discussed in section 2.1, if the number of interacting jets increases the amount of turbulence from the jets is suppressed. The cavitation bubbles that form

within the turbulent eddies is forced to collapse at lower *x/D* locations because the eddies (that are carrying the cavitation bubbles) rotational velocity is suppressed and the eddies die out.

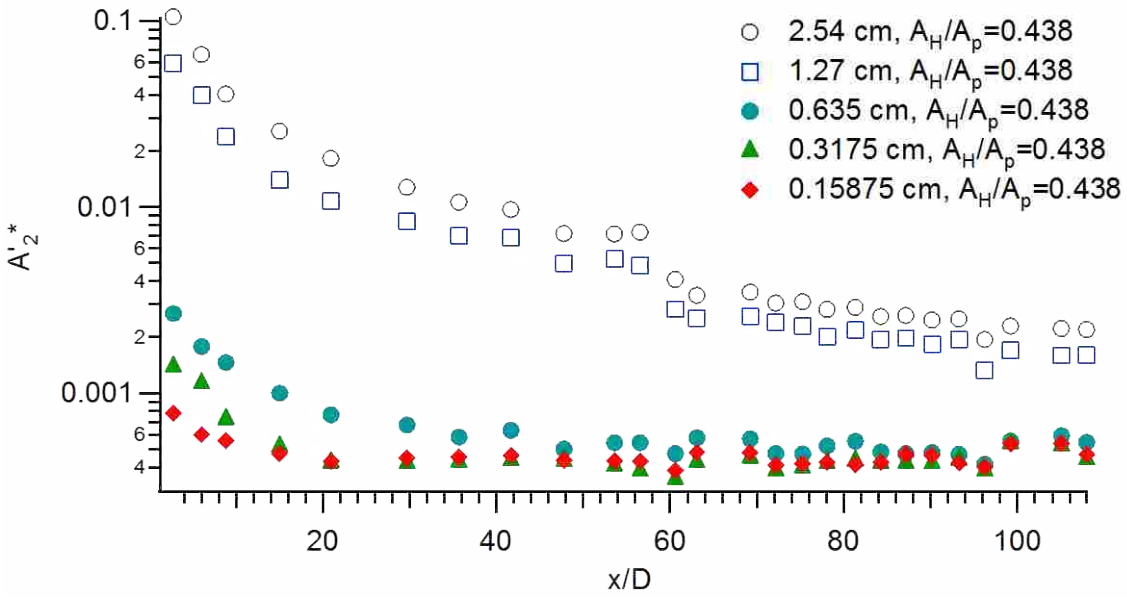

Figure 37: $A_2^{'*}$ vs. *x/D* for five baffle plates with varying baffle hole diameter, *d*, with constant through area ratio (A_H/A_p=0.438) and constant baffle hole velocity(v_H = 10.7 m/s). Open markers indicate that cavitation is occurring, and closed markers correspond to the non-cavitating regime.

When cavitation is not present the data of Figure 37 again shows that the attenuation distance occurs between 20 and 30 diameters, with the location increasing with increased baffle hole diameter. Between an *x/D* location of 56 and 60 was where the two pipes were joined with a flange.

The results discussed above show that the attenuation distance of pipe wall vibrations to the no baffle plate level increases dramatically with the appearance of cavitation. It is also discussed that the attenuation distance is highly dependent upon the baffle hole velocity, v_H, and the baffle hole diameter.

5.4 **Summary of Observations from the Results**

The following points summarize the important observations made in this chapter:

- The baffle plate loss coefficient was determined to be a function of both the through area ratio and thickness to diameter ratio, with the loss increasing as A_H/A_p decreases.
- Cavitation inception occurs at higher fluid velocities for increasing thickness to diameter ratio and increasing through area ratio. This point is very dependent upon the magnitude of the loss coefficient.
- Vibration levels increase with decreased thickness to diameter ratio, and decreased through area ratio for both the cavitating and non-cavitating regime, and are also related to the loss coefficient.
- The attenuation distance of vibration levels when the flow is non-cavitating occurs at nominally 20-30 diameters regardless of the flow velocity.
- The attenuation distance of vibration levels downstream of the baffle plate increases dramatically when cavitation is present.
- The attenuation distance of vibration levels also increases with increased baffle hole diameter and baffle hole velocity.

6 DEVELOPED MODELS

This chapter presents and gives a detailed discussion about the models that where produced from the empirical data. A total of ten models have been produced from this work. The use of these models will allow a designer to design for the pressure gradient loading caused by turbulence and cavitation induced pipe vibrations. The purpose of the models is to 1) Predict the cavitation design limits, 2) Predict the magnitude of A' in the non-cavitation regime and up to the critical cavitation design limit, and 3) Predict the streamwise distance from the baffle plate when the vibration levels attenuate. Figure 38 is a representative plot of A' vs. the cavitation number, σ, which will be referred to throughout this chapter to describe the models that were developed. Appendix A gives a description of how to use the models described in this section to predict the critical values in a design application.

This chapter will first discuss the loss coefficient model produced in section 6.1. It will then discuss the models produced for predicting the incipient and critical cavitation points in section 6.2. The model for predicting the A' levels at the incipient and critical cavitation points will then be discussed in section 6.3. Following this a discussion on the models produced to predict the pipe velocity at critical and incipient cavitation points in section 6.4. Section 6.5 will discuss the model developed for predicting the slope of the non-cavitating regime (the black line in Figure 38). Finally a discussion on the model developed for the attenuation data will be presented in section 6.6.

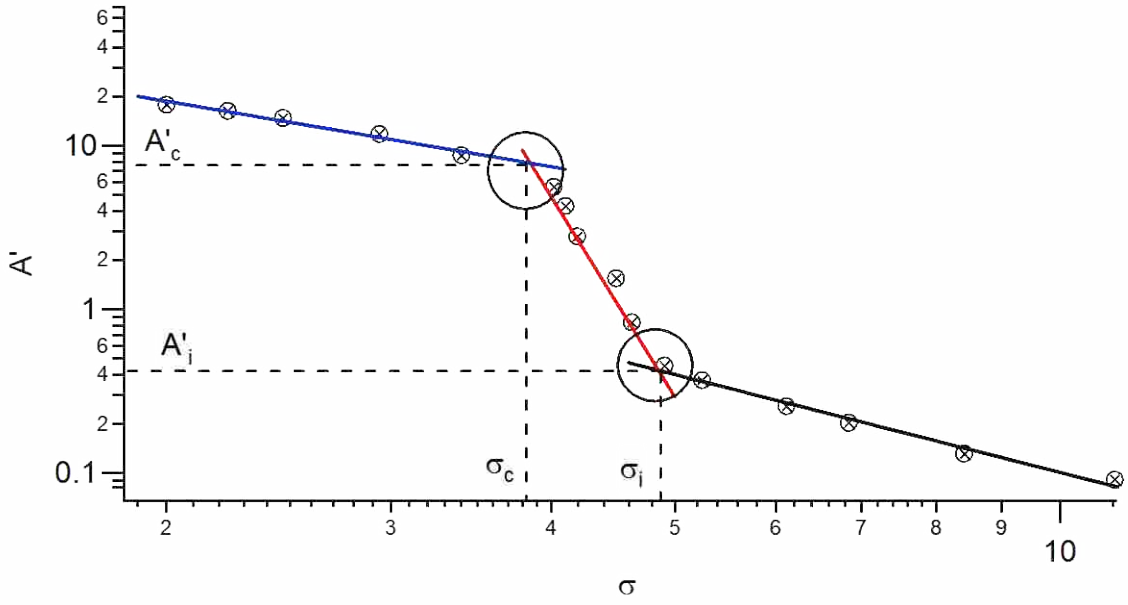

Figure 38: A representative plot of *A'* vs. the cavitation number, σ. The intersection of the red and black lines is the incipient cavitation design limit, σ_i, and the intersection of the blue and red lines is the critical cavitation design limit, σ_c.

6.1 Loss Coefficient

The loss coefficient is a very important parameter, due to the fact that cavitation inception and vibration levels are a function of it as was revealed in chapter 5. Equation (6.1) is a piecewise model that was produced to predict the loss coefficient based on all of the data at the point of cavitation inception. It should be noted that the loss coefficient only varied by about 5% before inception occurred. Thus, the model is useful in predicting K_L during the entire range of operation prior to cavitation. ϕ is defined in equation (6.2) and is a parameter that includes both A_H/A_p and t/d influences. This variable was developed from a multi-variable regression analysis. The theoretical loss coefficient model, K_{LA}, was discussed earlier and is defined in equation (6.3). The α value is defined in equation (6.4) where A_j is the jet velocity from the vena-contracta. This

value is assumed in the models here to remain at a constant value of 0.72. This is because this value created the best fit to the lower limit of the loss coefficient data as discussed in section 5.1. This model was developed by a statistical analysis of the data and by modifying the K_{LA} model with the empirical results that were obtained to account for the variation of the loss coefficient as a function of both the thickness to diameter ratio, *t/d,* and the through area ratio, A_H/A_p.

$$K_{LH} = \begin{cases} (2.9 - 3.79\phi + 1.79\phi^2)K_{L_A}, & \phi < 0.9 \\ (0.876 + 0.069\phi)K_{L_A}, & \phi \geq 0.9 \end{cases} \tag{6.1}$$

$$\phi = \left(\frac{t}{d}\right)\left(\frac{A_H}{A_p}\right)^{1/5} \tag{6.2}$$

$$K_{LA} = \left(1 - 2\left(\frac{A_p}{A_H}\right) + 2\left(\frac{A_p}{A_H}\right)^2\left(1 - \frac{1}{\alpha} + \frac{1}{2\alpha^2}\right)\right)\left(\frac{A_H}{A_p}\right)^2 \tag{6.3}$$

$$\alpha = \frac{A_j}{A_H} = 0.72 \tag{6.4}$$

Figure 39 provides a plot of K_{LH}/K_{LA} versus ϕ for all 14 plates where cavitation was observed (the $A_H/A_p = 0.609$ baffle plate did not cavitate at the speeds explored). Data acquired by Testud et. al. [13] are also shown in the figure for comparison. These two data points are for both a single hole orifice (ϕ =0.48) plate and a multi-hole orifice plate (ϕ = 2.56). As illustrated the data of Testud show excellent agreement with the present data and proposed model. The model is divided by two functions that represent thin baffle plates ($\phi \leq 0.9$) and a thick baffle plate ($\phi \geq 0.9$). Again, the thin baffle plate is for the plates where the flow does not reattach

within the baffle hole after the vena-contracta. The differences in the two functions of the model are caused by dominating effect of the losses. For the thick plate the increased loss coefficient with increased ϕ is attributed to the friction within the baffle hole. For a thin plate the increased losses with decreased ϕ is attributed to the increased turbulence effected by the flow not reattaching. In general the model follows the trend of acquired data over the entire range of baffle plates explored.

Figure 40 is a plot that shows the goodness of the model, where the measured loss coefficient is shown versus the modeled loss coefficient. A linear regression analysis yields an R^2 value of 0.967 and demonstrates that this is a robust model that can be used to accurately predict the loss coefficient based upon only geometry for sharp edge baffle plates only.

The implication of this model is that it allows for the prediction of the loss coefficient, which will then subsequently allow for the prediction of cavitation inception as discussed in the next section.

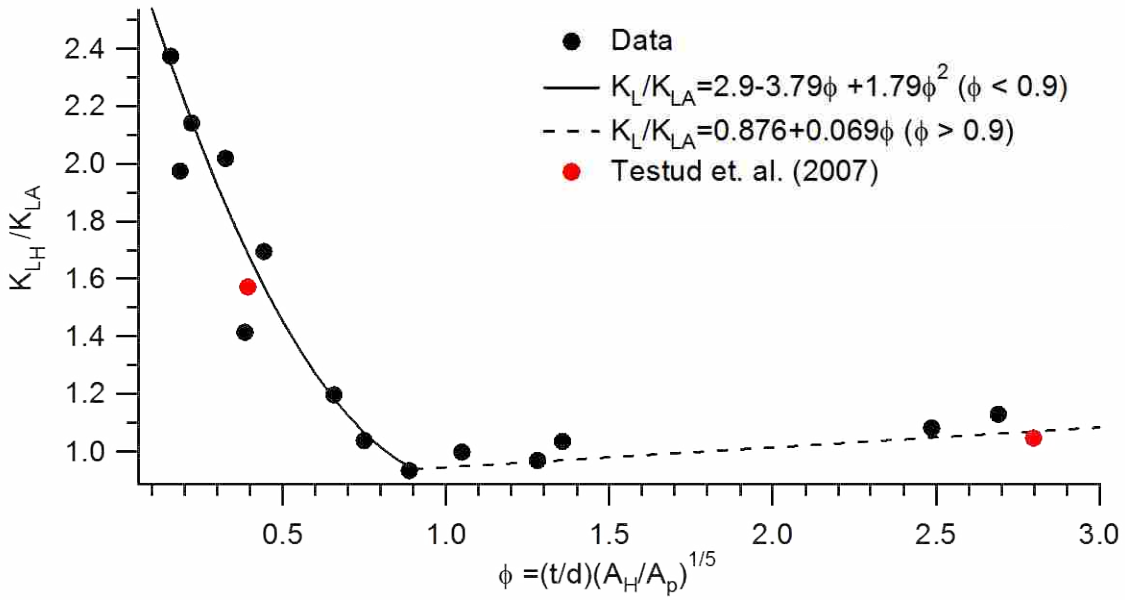

Figure 39: The ratio of the actual loss coefficient over the theoretical loss coefficient, K_{LH}/K_{LA}, vs. ϕ for 14 baffle plates along with data taken by Testud et. al. (2007) as shown in the figure legend.

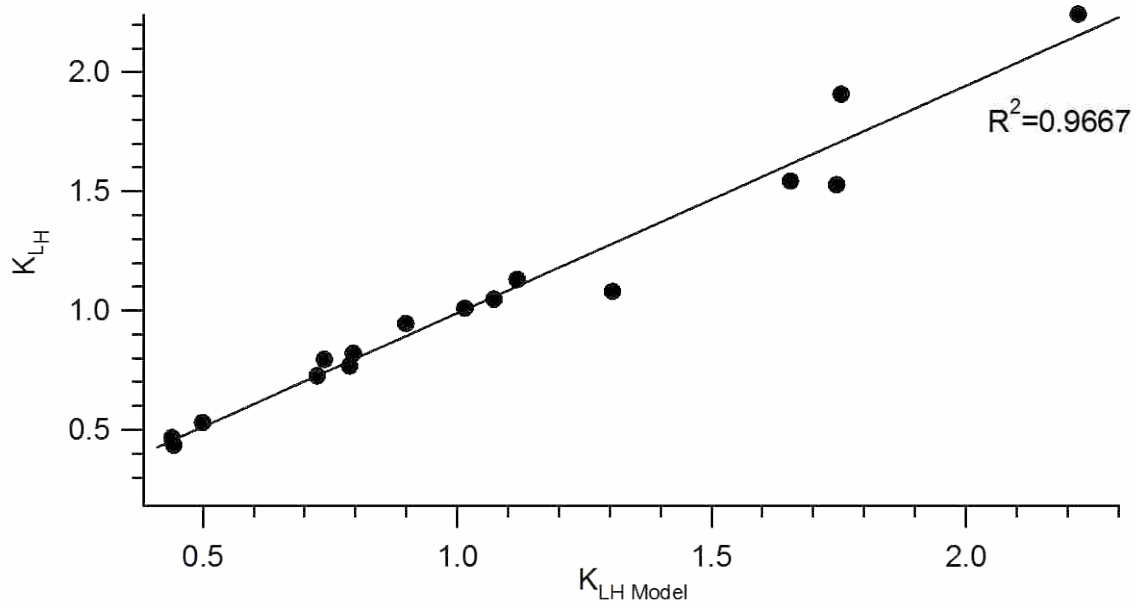

Figure 40: The actual loss coefficient, K_{LH}, vs. the modeled K_{LH} of Eq. (6.1). The goodness of fit is shown with an R^2 value of 0.967.

6.2 Incipient and Critical Cavitation Numbers

The incipient and critical cavitation numbers, σ_i and σ_c, are design limits of cavitation as illustrated in Figure 38. As discussed in section 2.4.2 a study by Tullis [15] showed that the cavitation number for orifices are dependent upon the size scaling effects as shown in equations (6.5) and (6.6). The model for size scale effect, *SSE*, developed by Tullis [15] is shown in equations (6.7) and (6.8). A model was developed based on the baffle plates of this study for the incipient and critical cavitation numbers with the size scale effects (σ_i^* and σ_c^*) as a function of the discharge coefficient. The models are given in equations (6.9) and (6.10). The discharge coefficient, c_d, (defined in equation (6.11)) is a function of the loss coefficient based off of the pipe velocity, K_{Lp} as defined in equation (6.12). This model shows that the variation in cavitation

inception is primarily due to the loss coefficient and the size scale effects. This model was developed by a linear regression analysis of the data where a curve was fit to the data.

$$\sigma_i = \frac{\sigma_i^*}{SSE} \tag{6.5}$$

$$\sigma_c = \frac{\sigma_c^*}{SSE} \tag{6.6}$$

$$SSE = \left(\frac{D}{d}\right)^Y \tag{6.7}$$

$$Y = 0.3K_{L_p}^{-0.25} \tag{6.8}$$

$$\sigma_i^* = -944c_d^4 + 1375c_d^3 - 663c_d^2 + 136c_d - 5.7 \tag{6.9}$$

$$\sigma_c^* = -685c_d^4 + 1026c_d^3 - 499c_d^2 + 102c_d - 4.3 \tag{6.10}$$

$$c_d = \frac{1}{\sqrt{K_{L_p}+1}} \tag{6.11}$$

$$K_{Lp} = K_{LH}\left(\frac{A_H}{A_p}\right)^{-2} \tag{6.12}$$

Figure 41 and Figure 43 show plots of the incipient and critical cavitation numbers with the sizes scale effects (σ_i^* and σ_c^*) versus the discharge coefficient, c_d, for the 13 baffle plates the models were developed from. The 2.54 cm diameter hole with 4 baffle holes (labeled as A2 in Table 1) was not used in the models due to hole spacing being larger than the pipe section causing added effects to cavitation inception that were not explored in this work. Also shown in the figure is data for one baffle plate that was used by Testud et. al. [13]. As illustrated the data of Testud et. al. show excellent agreement with the present data and proposed model. The data point with the open marker is a baffle plate that had slight rounding of the holes due caused by the manufacturing of the plate, and is included to illustrate the effect of rounding the baffle holes and will be discussed further below. This data point illustrates that the models developed are for sharp edged baffle plates only. From this figure it can be seen that there are two general trends to the data. Above a discharge coefficient $c_d \approx 4.0$ both σ_i^* and σ_c^* increase linearly with c_d. This region corresponds to baffle plates that are relatively thick as was discussed in section 5.1 in regards to the loss coefficient, with a discharge coefficient below $c_d \approx 4.0$ both σ_i^* and σ_c^* increase exponentially to an asymptotic value of $\sigma_i^* = 5$ and $\sigma_c^* = 4$ respectively. In general the model follows the trend of acquired data over the entire range of baffle plates explored.

Figure 42 and Figure 44 are plots that show the goodness of the model, where the measured σ_i^* and σ_c^* is shown versus the modeled σ_i^* and σ_c^*. A linear regression analysis yields an R^2 value of 0.997 and 0.978, respectively. This demonstrates that two models for σ_i^* and σ_c^* are robust models that can be used to accurately predict σ_i and σ_c based off of the geometry and the loss coefficient, that can be predicted from the model in the previous section.

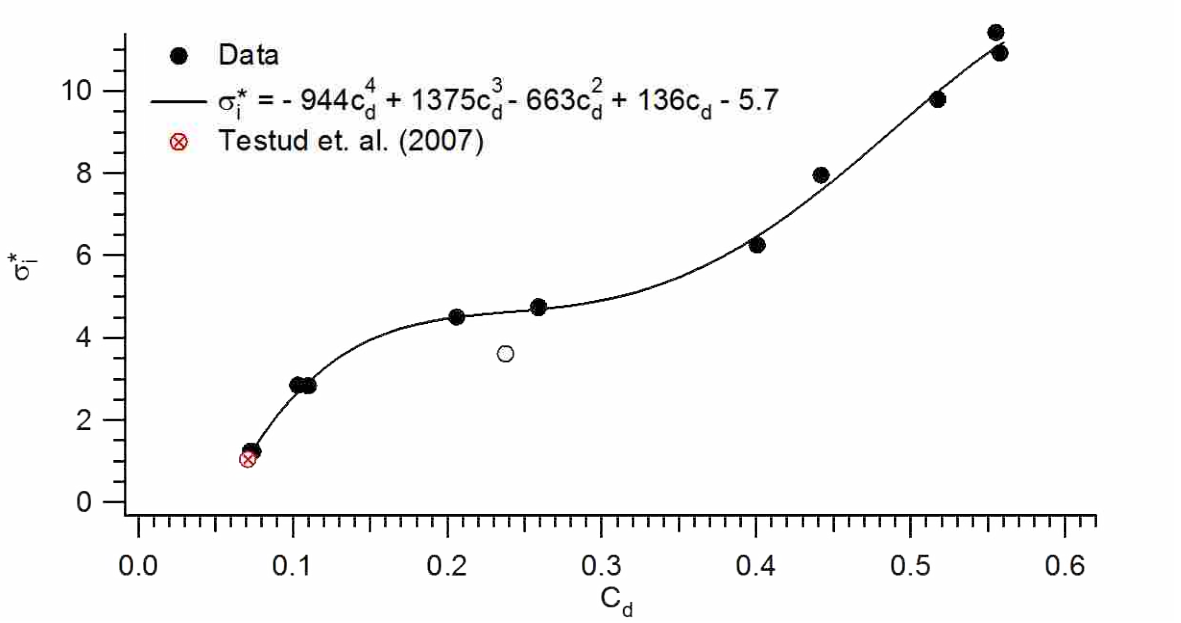

Figure 41: The incipient cavitation number with size scale effects, σ_i, vs. the discharge coefficient, c_d for 13 baffle plates. Data taken by Testud et. al. (2007) [13] is also shown. The open data point is a baffle plate that had slight chamfers for each of the baffle holes.

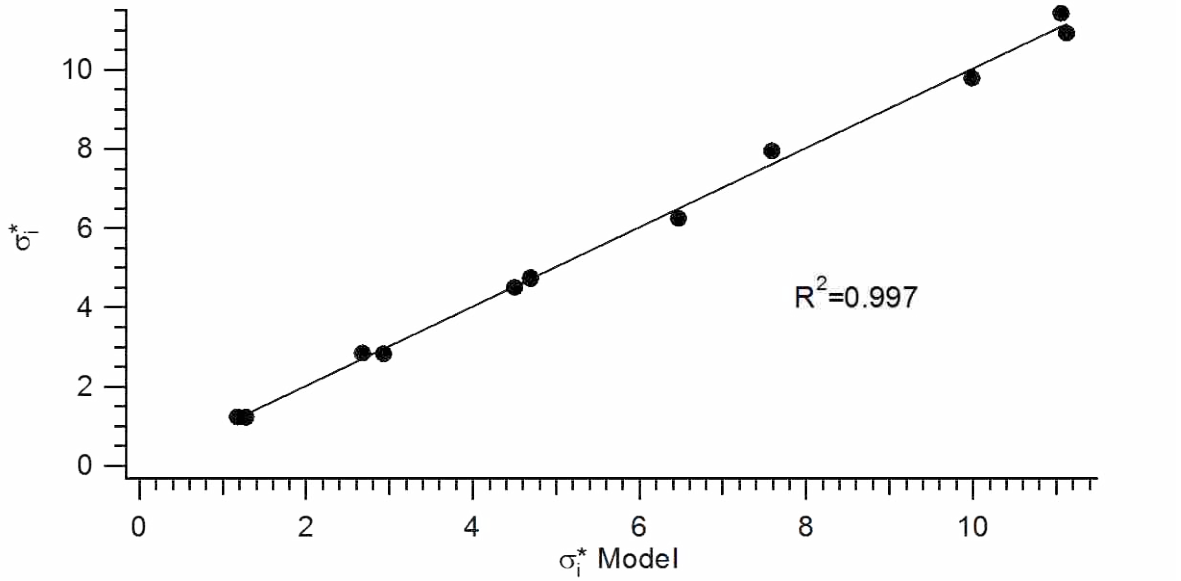

Figure 42: A plot of the actual incipient cavitation number with size scale effects, σ_i^*, vs. the developed model of Eq. (6.9) with an R^2 value equal to 0.997 as shown in figure.

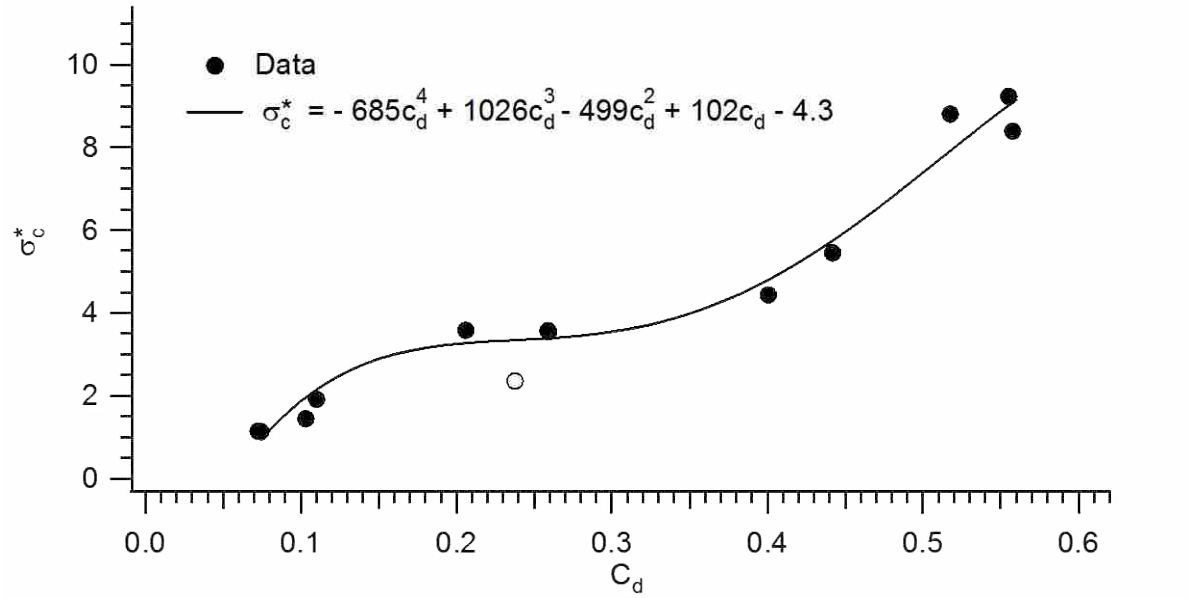

Figure 43: The critical cavitation number with size scale effects, σ_c^*, vs. the discharge coefficient, c_d for 13 baffle plates. The open data point is a baffle plate that had slight chamfers for each of the baffle holes.

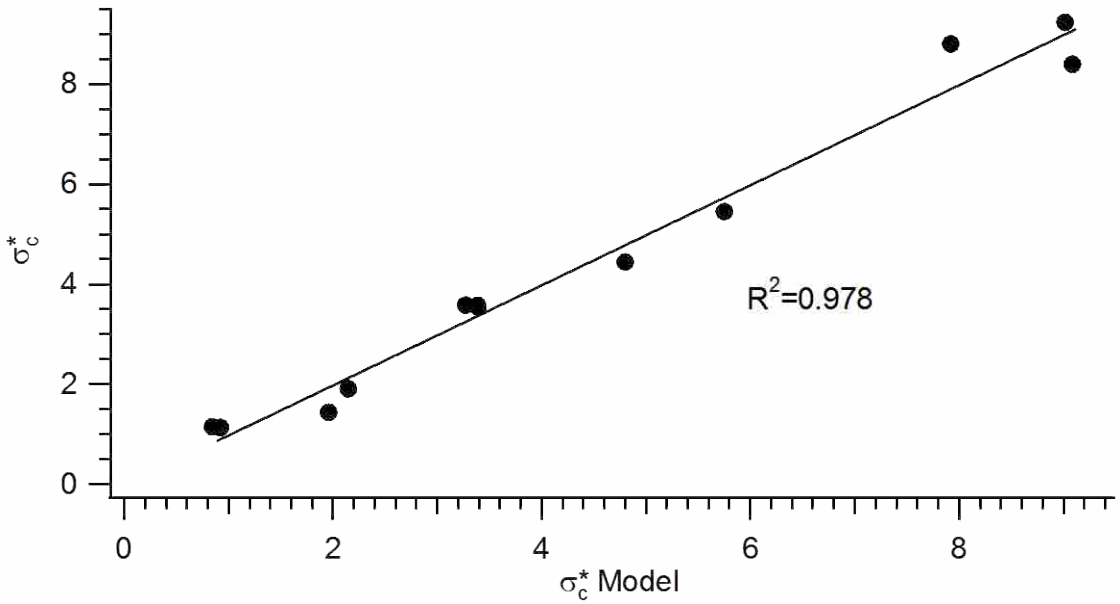

Figure 44: A plot of the actual critical cavitation number with size scale effects, σ_c^*, vs. the developed model of Eq. (6.10) with an R^2 value equal to 0.978 as shown in figure.

Figure 45 shows the incipient cavitation number with size scale effects, σ_i^*, versus the discharge coefficient, c_d, for the 13 baffle plates shown in Figure 41. Also shown on this figure

are data acquired by Testud et. al. (2007) [13], data from Tullis et. al. (1980) [9] for multi-hole orifice plates with rounding of the baffle holes at a radius of 0.9525 cm for the inlet of each hole, and data from Tullis (1989) [15] for a sharp edged single hole orifice. The open circle data point is again the outlier caused by a baffle plate that had slight chamfer for each of the baffle holes. This plot reveals the influence of rounding, and multiple holes. It can be seen that a multi-hole orifice plate has larger σ_i^* overall as compared to the single hole orifice. With increased rounding of a hole the baffle plate approaches the single hole orifice plate solution. The model that was developed as described above does not account for the effects of rounding the baffle holes. Further work will be needed to account for the effect of round the baffle holes.

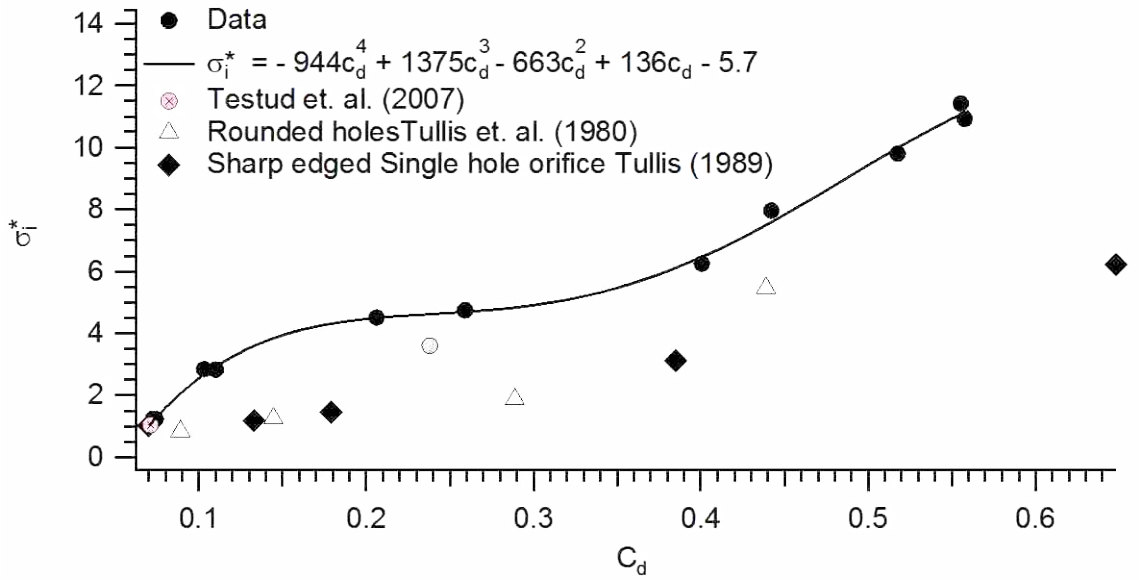

Figure 45: The incipient cavitation number with size scale effects, σ_i^*, vs. the discharge coefficient, c_d for 13 baffle plates. Data taken by Testud et. al. (2007) [13], data from Tullis et. al. (1980) [9] for multi-hole orifice plates with rounding of 0.9525 cm for the inlet of each hole, and data from Tullis (1989) [15] for a single hole orifice is also shown. The open circle data point is an outlier caused by a baffle plate that had slight chamfers for each of the baffle holes.

The models that were developed above for the incipient and critical cavitation points allow a designer to determine when cavitation will occur and when the flow has reached full cavitation. Conversely, the designer can utilize the models to determine the correct geometry of a baffle plate that will allow for the flow to stay below the undesirable cavitating range at specific flow rates.

6.3 A' at Critical and Incipient Cavitation

The RMS of the pipe wall acceleration, A', is used to characterize the vibrations of the pipe. The models developed for A' levels at incipient and critical cavitation points allow a designer to understand the loading that a pipe will experience at these design limits. The A' value at incipient and critical cavitation levels are illustrated in Figure 38. Equations (6.13) and (6.14) provide the models developed for the non-dimensionalized A' levels at the point of incipient and the point of critical cavitation. The non-dimensionalized A' values ($A_i'^*$ and $A_c'^*$) are defined in equations (6.15) and (6.16) and the β_i and β_c values are defined in equations (6.17) and (6.18). These models were developed by performing a multi-variable linear regression analysis of the data, were β_i and β_c were produced from this analysis.

$$ln(A_i'^*) = 0.038\,(ln(\beta_i))^3 - 0.45\,(ln(\beta_i))^2 + 0.039\,ln(\beta_i) - 8.86) \tag{6.13}$$

$$ln(A_c'^*) = 0.028\,(ln(\beta_c))^3 - 0.33(ln(\beta_c))^2 - 0.35\,ln(\beta_c) - 6.74 \tag{6.14}$$

$$A_i^{'*} = \frac{A_i^{'} d}{v_{H_i}^2} \tag{6.15}$$

$$A_c^{'*} = \frac{A_c^{'} d}{v_{H_c}^2} \tag{6.16}$$

$$\beta_i = \sigma_i \left(\frac{t}{d}\right)^{1.8} \left(\frac{A_H}{A_p}\right)^{-0.6} \tag{6.17}$$

$$\beta_c = \sigma_c \left(\frac{t}{d}\right)^{1.8} \left(\frac{A_H}{A_p}\right)^{-0.6} \tag{6.18}$$

Figure 46 and Figure 48 are plots of the natural logarithm of the non-dimensionalized A' value at the incipient and critical cavitation points ($A_i^{'*}$ and $A_c^{'*}$) versus the natural logarithm of β_i and β_c for the baffle plates used. For the $A_c^{'*}$ model only 12 plates were used since the range of velocities for plate D1 of Table 1 was not high enough to obtain the critical cavitation value. This figure shows that there is a local maximum of vibrations around ln(β) = 0. In general these models follow the trend of acquired data over the entire range of baffle plates explored.

Figure 47 and Figure 49 are plots that show the goodness of the model, where the measured $A_i^{'*}$ and $A_c^{'*}$ is shown versus the modeled $A_i^{'*}$ and $A_c^{'*}$. A linear regression analysis yields a R^2 value of 0.964 and 0.984, respectively. This demonstrates that two models for $A_i^{'*}$ and $A_c^{'*}$ are robust models that can be used to accurately predict $A_i^{'*}$ and $A_c^{'*}$ based off of the geometry and the σ_i and σ_c values, that can be determined from the models in the previous section.

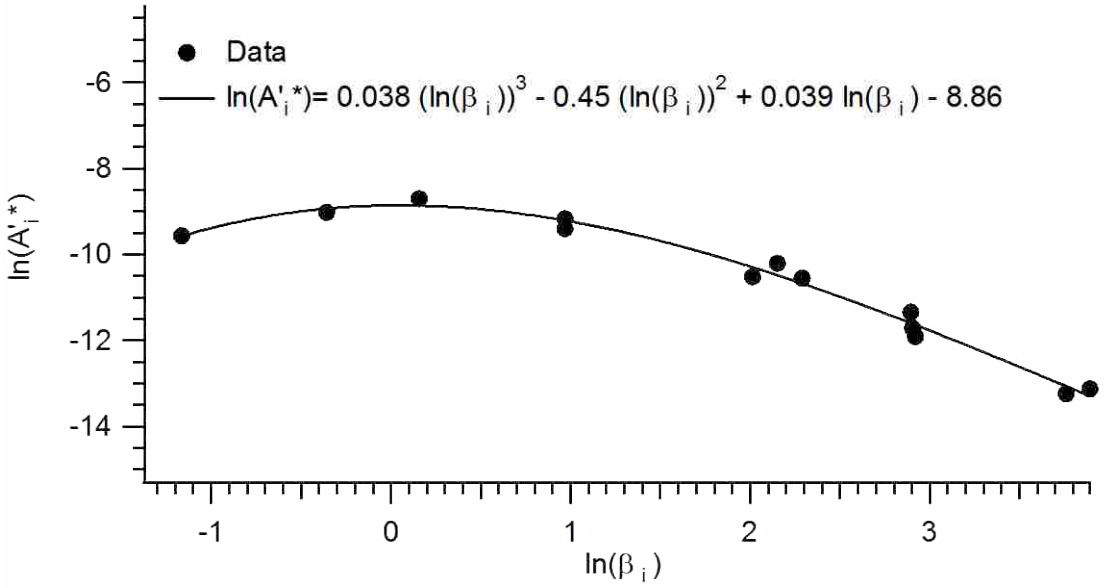

Figure 46: $ln(A_i^{'*})$ as a function of β_i for 13 baffle plate.

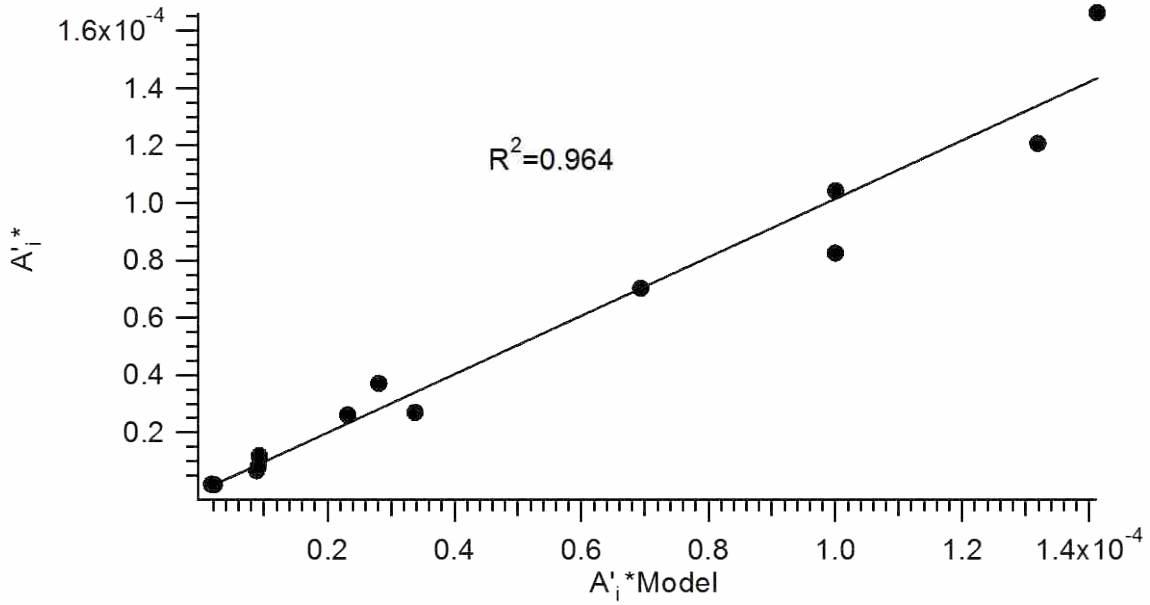

Figure 47: A plot of the actual $A_i^{'*}$ vs. the model developed in Eq. (6.13) with an R^2 value equal to 0.964 as shown in figure.

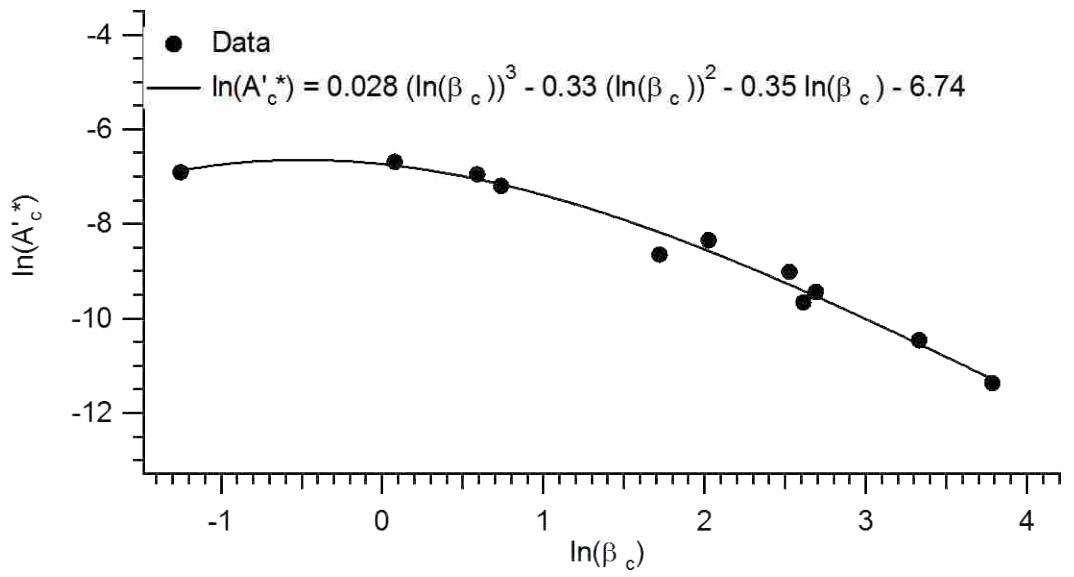

Figure 48: $ln(A_c^{'*})$ as a function of β_c for 12 baffle plate.

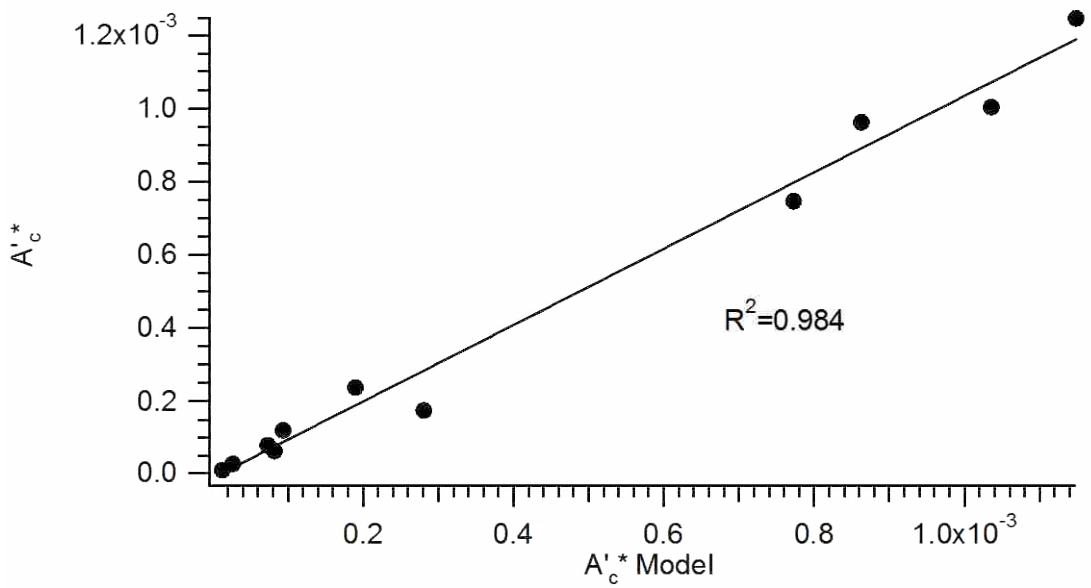

Figure 49: A plot of the actual $A_c^{'*}$ vs. the model developed in Eq. (6.14) with an R^2 value equal to 0.984 as shown in figure.

The models developed in this section for $A_i^{'*}$ and $A_c^{'*}$ allow a designer to now determine the loading for a fatigue analysis to design for the fatigue life of a pipe section for the entire

incipient cavitation regime (the red line in Figure 38). This is because the points (σ_i, $A_i^{'*}$) and (σ_c, $A_c^{'*}$) from Figure 38 can be solved for and the A' versus σ curve between these two points is linear on a log-log scale. This allows for prediction of the cavitation induced vibration between these two important points.

6.4 **The Incipient and Critical Velocities**

The incipient and critical velocities (v_{pi} and v_{pc}) are the average pipe velocities at the point of cavitation inception and critical cavitation. The purpose for obtaining the model of the v_{pi} and v_{pc} is so that the A' can be determined. The models that were developed in section 6.3 were for $A_i^{'*}$ and $A_c^{'*}$, the non-dimensionalized A' levels that were normalized by the baffle hole velocities. The models that were developed for v_{pi} and v_{pc} are given in equations (6.19) and (6.20). The value ψ is defined in equation (6.21) which is a parameter that includes both c_d and t/d influences. This variable was produced from the multi-variable linear regression analysis that was performed to create the models. As can be seen both v_{pi} and v_{pc} are linear functions of ψ.

$$v_{pi} = 8.65\,\psi + 0.11 \tag{6.19}$$

$$v_{pc} = 10.64\,\psi + 0.1 \tag{6.20}$$

$$\psi = c_d \left(\frac{t}{d}\right)^{0.15} \tag{6.21}$$

Figure 50 and Figure 51 provide plots of v_{pi} and v_{pc} versus ψ for the same 13 baffle plates as Figure 41. This plot shows that in general the model follows the trend of acquired data over the entire range of baffle plates explored.

Figure 52 and Figure 53 are plots that show the goodness of the model, where the measured v_{pi} and v_{pc} is shown versus the modeled v_{pi} and v_{pc} . A linear regression analysis yields a R^2 value of 0.9811 and 0.985, respectively and demonstrates that two models for v_{pi} and v_{pc} are robust models that can be used to accurately predict v_{pi} and v_{pc} based off of the geometry and the c_d, that can be solved from the loss coefficient model developed in section 6.1. Again, these models allow that the A' level at the incipient and critical cavitation points can be determined and are needed so that the A' levels through the non-cavitating regime can be determined for as discussed in the next section.

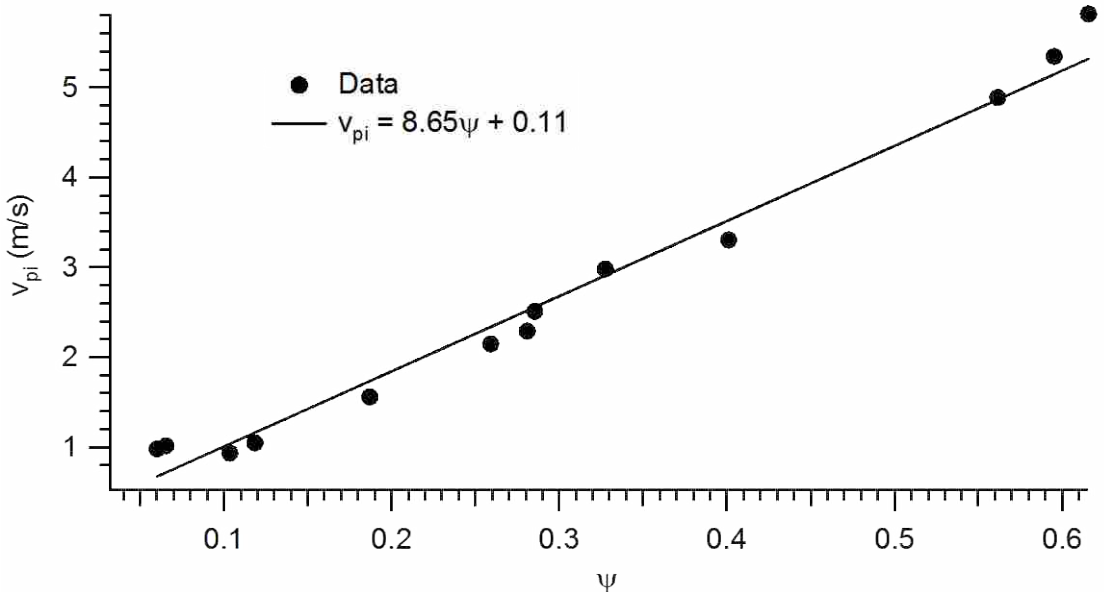

Figure 50: The pipe velocity at critical cavitation, v_{pi}, vs. ψ for 13 baffle plates.

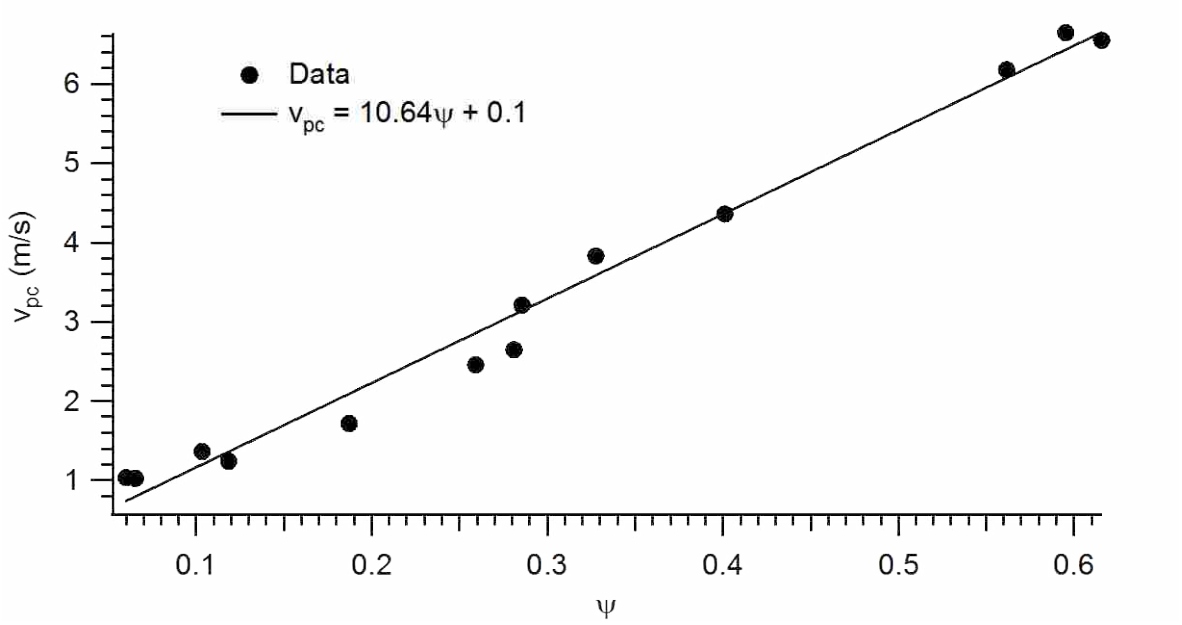

Figure 51: The pipe velocity at critical cavitation, v_{pc}, vs. ψ for 13 baffle plates.

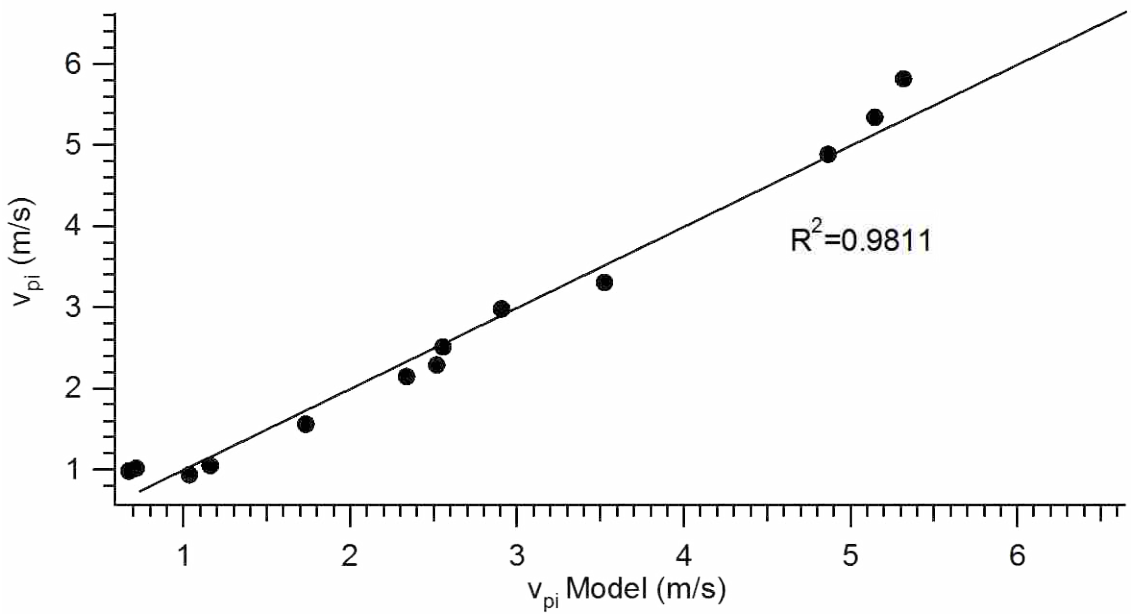

Figure 52: A plot of the actual v_{pi} vs. the model developed in Eq. (6.19) showing an R^2 value equal to 0.981 as shown in figure.

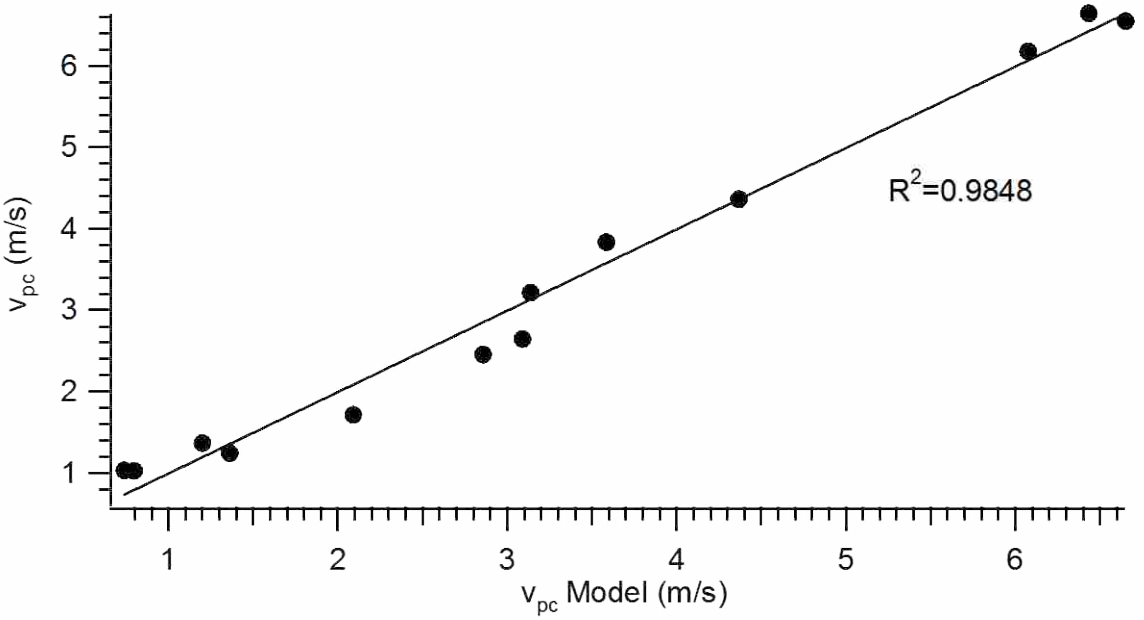

Figure 53: A plot of the actual v_{pc} vs. the model developed in Eq. (6.20) showing an R^2 value equal to 0.985 as shown in figure.

6.5 **Slope for Non-Cavitating Regime**

The flow induced vibrations of a pipe is not limited to cavitation alone. When the flow is not cavitating vibrations of a pipe wall occur from turbulence, as was discussed in section 6.2. For a designer, a model of the turbulent induced vibrations from a baffle plate is needed for analysis when cavitation is not occurring in a flow. To develop models of the turbulent induced vibrations a model of the slope of the non-cavitating regime, m, (this is the slope of the black line in Figure 38) is developed. By knowing this slope, the A' levels through the non-cavitating regime can be determined. This is due to the fact that the point (σ_i, A') is known by using the models of the previous sections. This allows for the development of a non-cavitating turbulent induced model. The model that was developed is shown in equation (6.22) where m^* is defined

in equation (6.23) and ε is defined in equation (6.24). Both m^* and ε are produced from the multi-variable linear regression analysis that was used to create the model.

$$m^* = 1.2 - 0.72\,exp(-252\varepsilon) - 0.38\,exp(-1840\varepsilon) \tag{6.22}$$

$$m^* = \frac{m}{2\,ln\left(\frac{A_H}{A_p}\right) - 0.4} \tag{6.23}$$

$$\varepsilon = \left(\frac{d}{D}\right)\left(\frac{t}{d}\right)^{0.4}\left(\frac{A_H}{A_p}\right)^{2.5} \tag{6.24}$$

Figure 54 is a plot of m^* versus ε for the same 13 baffle plates of Figure 50 where cavitation was observed. In general the model follows the trend of acquired data over the entire range of baffle plates explored.

Figure 55 show the goodness of the model, where the measured m^* is shown versus the modeled m^*. A linear regression analysis yields an R^2 value of 0.976, and demonstrates that the model for m^* is a robust models that can be used to accurately predict the slope of the black line in Figure 38 based off of the geometry of the baffle plate. Again, this model allows for prediction of vibration levels throughout the entire turbulent regime.

The models developed in the above sections can now be used to predict a figure similar to Figure 38 for any sharp edged baffle plate geometry. A discussion on how to do so is discussed in Appendix A. Creating a plot of this nature provides the desired A' levels to be known for all flow rates up to the critical design limit for any sharp edged baffle plate geometry.

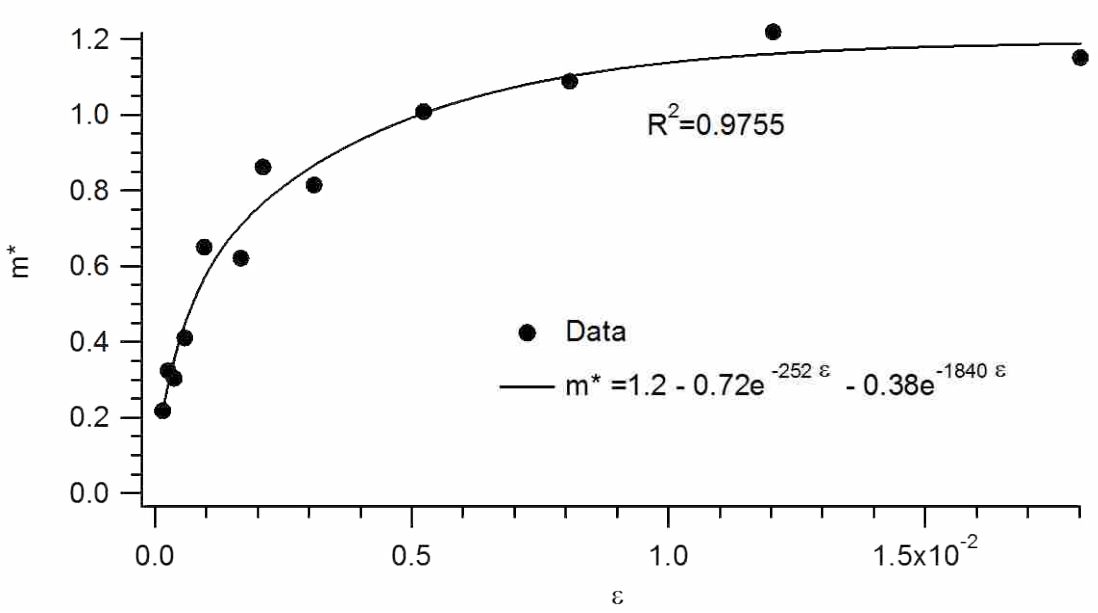

Figure 54: A plot of *m as a function of *ε* for 13 baffle plates**

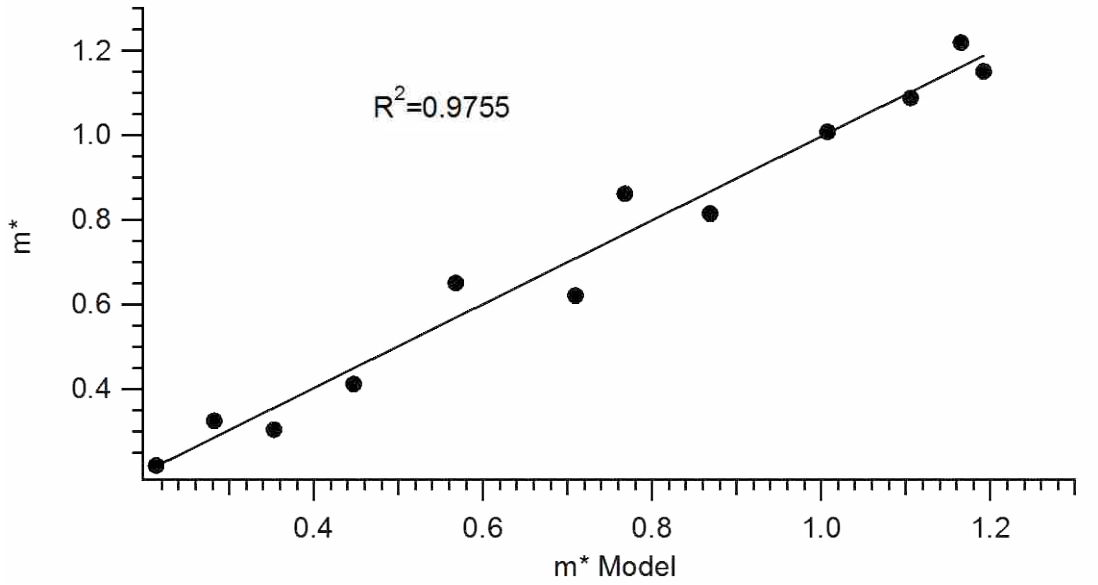

Figure 55: A plot of the actual *m value vs. the model developed in Eq. (6.22) showing an R^2 value equal to 0.976 as shown in figure.**

6.6 **Attenuation of Vibration**

The models developed in the previous sections are used to predict the vibration levels that occur at three diameters downstream from the baffle plate. Because the vibration levels caused from the flow through the baffle plate attenuated downstream as discussed in section 5.3, a model for this attenuation also was developed. Equation (6.26) shows the model that was developed for the attenuation distance. The model is a function of both the baffle hole velocity, v_H, and the baffle hole velocity at the point of cavitation inception, v_{Hi}. v_{Hi} can be obtained by knowing v_{pi} from the model discussed in section 6.4 and by using the continuity equation shown in equation (6.25).

$$v_{Hi} = v_{pi}\left(\frac{A_p}{A_H}\right) \tag{6.25}$$

$$\frac{x}{D} \cong \begin{cases} 20\ to\ 30, & v_H/v_{Hi} < 1 \\ 120\dfrac{v_H}{v_{Hi}} - 75, & 1 \leq \dfrac{v_H}{v_{Hi}} \geq 1.5 \\ 105\ to\ 110, & v_H/v_{Hi} > 1.5 \end{cases} \tag{6.26}$$

Figure 56 shows the *x/D* location where the vibration levels attenuate downstream of the baffle plate as a function of the ratio of the baffle hole velocity over the baffle hole velocity at cavitation inception, v/v_{Hi}, for a given plate. In the figure the attenuation distance was defined to be the *x/D* location where $A_2^{'*}$ had decayed to 1.5 times the $A_2^{'*}$ level of the non-baffle plate condition at the same pipe velocity. $A_2^{'*}$ is again defined in equation (6.27). This figure shows that with exception of a few outliers the general trend of the attenuation of vibrations

downstream of a baffle plate. When cavitation is not occurring $v_H/v_{Hi} \leq 1.0$ the attenuation of vibrations occurs no greater than 20 to 30 *x/D* locations. When cavitation is occurring $v_H/v_{Hi} \geq 1.0$ and $v_H/v_{Hi} \leq 1.5$ the *x/D* location of the attenuation of vibrations increase dramatically with increased v_H/v_{Hi} where $v_H/v_{Hi} \geq 1.5$ the *x/D* location of the attenuation of vibrations occurs no greater than 105 to 110. This model allows for an estimate for how the A' attenuated downstream.

$$A_2^{'*} = \frac{A^{'} D}{v_p^2} \tag{6.27}$$

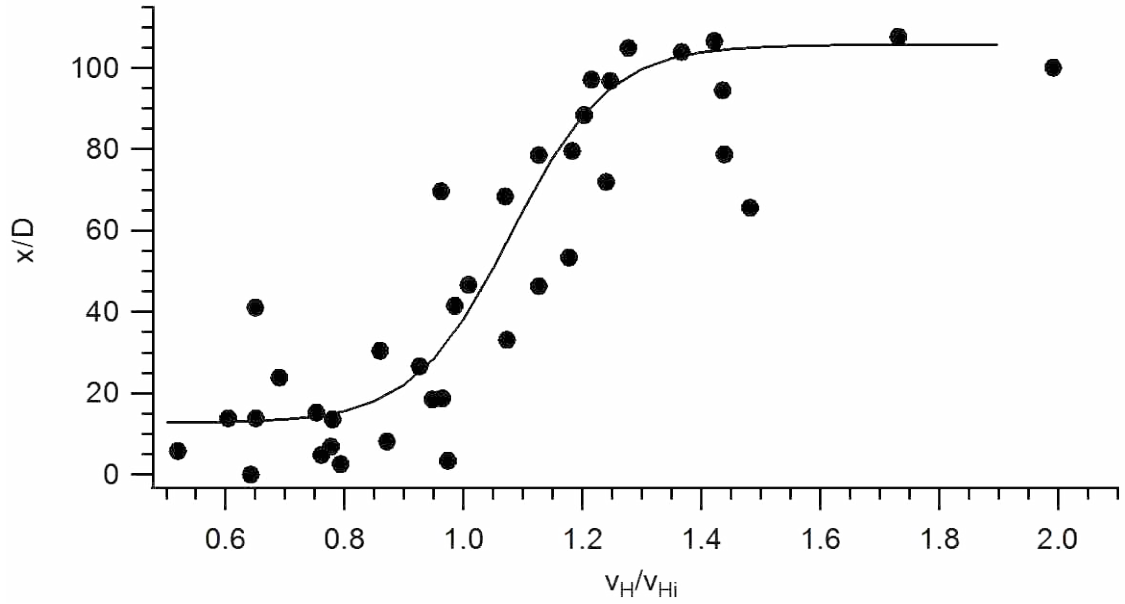

Figure 56: The attenuation of vibration levels downstream of the baffle plate, *x/D*, vs. *Re*/*Re*$_i$.

7 CONCLUSIONS

7.1 Summary of Results

A study on the cavitation and turbulent induced pipe vibrations caused by 16 sharp edge baffle plates was conducted. Cavitation and turbulent induced pipe vibrations were characterized as a function of the geometry of the baffle plates. The following key findings of this work are listed below:

- The baffle plate loss coefficient was determined to be a function of both the through area ratio and thickness to diameter ratio, and the number of baffle holes.
- Cavitation inception occurs at higher fluid velocities with increased thickness to diameter ratio where the baffle hole velocity varies from nominally 7 m/s to 13 m/s from a t/d ratio of 0.25 to 3.3 for $A_H/A_p = 43.8\%$.
- Cavitation inception occurs at higher fluid velocities with increased through area ratio where the baffle hole velocity varies from nominally 9.5 m/s to 13 m/s from a A_H/A_p ratio of 10.9% to 43.8% for $t/d = 1.7$.
- Cavitation inception is a function of the radius of curvature of the baffle holes and rounding can delay cavitation inception.
- Vibration levels increase with decreased plate thickness to hole diameter ratio by about an order of magnitude for a range of t/d of 0.25 to 3.3,
- Vibration levels doubled with a decrease in A_H/A_p ratio from 43.8% to 10.9%.

- The attenuation of vibration levels when the flow is non-cavitating occurs at increasing flow rates up until nominally 20-30 diameters regardless of the flow velocity.
- The attenuation of vibration levels within the cavitating regime dramatically increases with increased flow rate from nominally 20 to 100 diameters. At average baffle fluid velocities above 1.5 times the incipient baffle fluid velocity, the attenuation distance is nominally 100-110 diameters
- Models predicting the loss coefficient, incipient and critical cavitation numbers, and the RMS of the pipe wall acceleration, A', from non-cavitating flow to the critical cavitation level, have been developed

7.2 **Recommendations**

The recommendations for future work are as follows:

- Testing of actual valves and trims to evaluate how they perform relative to the developed models.
- Explore the effects of rounding the baffle hole.
- Further validation of models with baffle plates for larger discharge coefficients that were not explored.
- Further validation of models with varying pipe diameters.

REFERENCES

[1] S.H. Bush, "Failure Mechanisms in Nuclear Power Plants Piping Systems," *Journal of pressure vessel technology*, vol. 114, no. 4, pp. 389-395, November 1992.

[2] Mao Qing, Zhang Jinghui, Luo Yushan, Wang Haijun, and Duan Quan, "High-Level Vibration and Noise Analysis of Nuclear Pipes with Orifice," in *Transactions of the 17th Internation Confrence on Structural Mechanics in Reactor Technology*, Prague, Czech Republic, August 17-22, 2003, pp. O02-6.

[3] National Transportation Safety Board, "Pipeline Accident Brief," NTSB/PAR-04/01, Pipeline accident number: PB2004-916501, July 4, 2002.

[4] David C. Wilcox, *Turbulence Modeling for CFD 3rd*.: DCW Industries, Inc., 2006.

[5] Matthew T. Pittard, Robert P. Evans, R. Daniel Maynes, and Jonathan D. Blotter, "Experimental and Numerical Investigation of Turbulent Flow Induced Pipe Vibration in Fully Developed Flow," *Review of Scientific Instruments*, vol. 75, pp. 2393-2401, July 2004.

[6] Robert P. Evans, Jonathan D. Blotter, and Alan G. Stephens, "Flow Rate Measurements Using Flow-Induced Pipe Vibration," *Transactions of the ASME*, vol. 126, pp. 280-285, March 2004.

[7] Andrew Thompson, "Experimental Charactarization of Flow Induced Vibration in Turbulent Pipe Flow," Brigham Young University, Provo, Master's Thesis 2009.

[8] Andrew S. Thompson, Daniel Maynes, Thomas Shurtz, and Jonathan D. Blotter, "Experimental Characterization of Flow Induced Vibration in Fully Developed Turbulent Pipe Flow," in *Proceedings of the ASME Fluids Engineering Summer Meeting*, August 2009, pp. 1771-1778.

[9] J. Paul Tullis, James J. Powers III, Paul F. Shiers, and Whitney W. Hall, "Perforated Plates as Hydraulic Energy Dissipators," in *Computer and Physical Modeling in Hydraulic Engineering*, August 1980, pp. 62-73.

[10] F. Numachi, M. Yamabe, and R. OBA, "Cavitation Effect on the Discharge Coefficient of the Sharp-Edged Orifice Plate," *Journal of Basic Engineering*, vol. 82, pp. 1-11, March 1960.

[11] P. A. Kolodzie and Matthew Van Winkle, "Discharge Coefficients Through Perforated Plates," *AICHE Journal*, vol. 3, pp. 305-312, September 1957.

[12] Bruce R. Munson, Donald F. Young, and Theodore H. Okiishi, *Fundamentals of Fluid Mechanics 5th*.: John Wiley & Sons, 2006.

[13] P. Testud, P. Moussou, A. Hirschburg, and Y. Auregan, "Noise Generated by Cavitating Single-hole and Multi-hole Orifices in a Water Pipe," *Journal of Fluids and Structures*, vol. 23, pp. 163-189, February 2007.

[14] J. Paul Tullis, M. ASCE, and Rangachari Govindarajan, "Cavitation and Size Scale Effects for Orifices," *ASCE Journal of Hydraulics Division*, vol. 97, pp. 417–430, March 1973.

[15] J. Paul Tullis, *Hydraulics of Pipelines Pumps, Valves, Cavitation, Transients*.: John Wiley & Sons, 1989.

[16] S. C. Li, *Cavitation of Hydraulic Machinery*.: Imperial College Press, 2000.

[17] Yves Lecoffre, *Cavitation Bubble Trackers*.: AA Balkema Publishers, 1999.

[18] J. Paul Tullis, "Cavitation Guide for Control Valves," *US Nuclear Regulatory Commission*, April 1993.

[19] Mao Qing, Zhang Jinghui, Luo Yushan, Wang Haijun, and Duan Quan, "Experimental Studies of Orifice-induced Wall Pressure Fluctuations and Pipe Vibration," *Internation Journal of Pressure Vessels and Piping*, vol. 83, pp. 505-511, March 2006.

[20] John Lawson and John Erjavec, *Modern Statistics for Engineering and Quality Improvement*. Pacific Grove, CA: Wadsworth Group, 2001.

[21] Richard S. Figliola and Donald E. Beasley, *Theory and Design for Mechanical Measurements* , 4th ed. Danvers, MA: John Wiley and Sons, Inc., 2006.

APPENDIX A. INSTRUCTIONS ON USE OF MODELS

To illustrate how to properly use the developed models the following example is provided.

Example:

If a baffle plate with a hole size of 0.634 cm with thickness of 0.67 cm and number of holes of 112 was designed for a 10.16 cm pipe with a working fluid of water, what would be the acceleration levels for a range of cavitation numbers up to the critical design limit?

Solution:

First the loss coefficient will be needed and can be found using equations (6.1)-(6.4).

$$\phi = \left(\frac{t}{d}\right)\left(\frac{A_H}{A_p}\right)^{\frac{1}{5}} = 1.01 \tag{A. 1}$$

$$K_{L_A} = \left(1 - 2\left(\frac{A_p}{A_H}\right) + 2\left(\frac{A_p}{A_H}\right)^2\left(1 - \frac{1}{\alpha} + \frac{1}{2\alpha^2}\right)\right)\left(\frac{A_H}{A_p}\right)^2 = 0.47 \tag{A. 2}$$

$$\boxed{K_{L_H} = (0.876 + 0.069\phi)K_{L_A} = 0.44} \tag{A. 3}$$

Now knowing the loss coefficient the discharge coefficient can be obtained so as to find the values for the incipient and critical cavitation numbers. These values can be obtained using equations (6.5)-(6.12).

$$K_{L_p} = K_{L_H}\left(\frac{A_H}{A_p}\right)^{-2} = 2.33 \tag{A. 4}$$

$$c_d = \frac{1}{\sqrt{K_{L_p} + 1}} = 0.55 \tag{A. 5}$$

$$\sigma_i^* = -944c_d^4 + 1375c_d^3 - 663c_d^2 + 136c_d - 5.7 = 10.91 \tag{A. 6}$$

$$\boxed{\sigma_i = \frac{\sigma_i^*}{SEE} = 5.55} \tag{A. 7}$$

$$\sigma_c^* = -685c_d^4 + 1026c_d^3 - 499c_d^2 + 102c_d - 4.3 = 8.85 \tag{A. 8}$$

$$\boxed{\sigma_c = \frac{\sigma_c^*}{SEE} = 4.51} \tag{A. 9}$$

With the incipient and critical cavitation numbers determined the A'^* at the incipient and critical cavitation values can be obtained using equations (6.13)-(6.18).

$$\beta_i = \sigma_i \left(\frac{t}{d}\right)^{1.8} \left(\frac{A_H}{A_p}\right)^{-0.6} = 10.1 \quad \text{(A. 10)}$$

$$A_i^{'*} = ex\,p(0.038\,ln(\beta_i)^3 - 0.45\ ln(\beta_i)^2 + 0.039\,ln(\beta_i) - 8.86) = 2.24\text{x}10^{-5} \quad \text{(A. 11)}$$

$$\beta_c = \sigma_c \left(\frac{t}{d}\right)^{1.8} \left(\frac{A_H}{A_p}\right)^{-0.6} = 8.19 \quad \text{(A. 12)}$$

$$A_c^{'*} = exp(0.028\,ln(\beta_c)^3 - 0.33\ ln(\beta_c)^2 - 0.35\,ln(\beta_c) - 6.74) = 1.71\text{x}10^{-4} \quad \text{(A. 13)}$$

By solving for v_{Hi} and v_{Hc} using equations (6.19)-(6.21), $A_i^{'}$ and $A_c^{'}$ can be found using equations (6.15) and (6.16).

$$\psi = c_d \left(\frac{t}{d}\right)^{0.15} = 0.55 \quad \text{(A. 14)}$$

$$v_{pi} = (8.65\,\psi + 0.11) = 4.9\ \text{m/s} \quad \text{(A. 15)}$$

$$v_{Hi} = v_{pi} \left(\frac{A_H}{A_p}\right)^{-1} = 11.24\ \text{m/s} \quad \text{(A. 16)}$$

$$\phi = \left(\frac{t}{d}\right)\left(\frac{A_H}{A_p}\right)^{\frac{1}{5}} = 1.01 \quad \text{(A. 17)}$$

$$v_{pc} = (10.64\,\psi + 0.1) = 5.99\ \text{m/s} \quad \text{(A. 18)}$$

$$v_{Hc} = v_{pc}\left(\frac{A_H}{A_p}\right)^{-1} = 13.74\ \text{m/s} \tag{A. 19}$$

$$\boxed{A_i^{'} = \frac{A_i^{'*} v_{Hi}^2}{d} = 0.45} \tag{A. 20}$$

$$\boxed{A_c^{'} = \frac{A_c^{'*} v_{Hc}^2}{d} = 5.09} \tag{A. 21}$$

Figure 57 shows the design limits that have been solved for on a plot of A' versus σ. By knowing $A_i^{'}$, $A_c^{'}$, and the cavitation numbers at both the incipient and critical values, $A^{'}$ is now known for the entire incipient cavitation regime (The red line in Figure 57). This is because we know that the $A^{'}$ within the region between the incipient and critical cavitation values is linear with σ on a log-log scale. An equation for this section can now be developed, where m_2 is the slope of the line and y_2 is the y-intercept.

$$ln(A^{'}) = m_2\, ln(\sigma) + y_2 \tag{A. 22}$$

$$m_2 = \frac{ln(A_c^{'}) - ln(A_i^{'})}{ln(\sigma_c) - ln(\sigma_\text{i})} = -11.65 \tag{A. 23}$$

$$y_2 = ln(A_i^{'}) - slope_2\, ln(\sigma_i) = 19.17 \tag{A. 24}$$

$$\boxed{ln(A') = -11.65\, ln(\sigma) + 19.17, \qquad \sigma_i \leq \sigma \leq \sigma_c} \tag{A. 25}$$

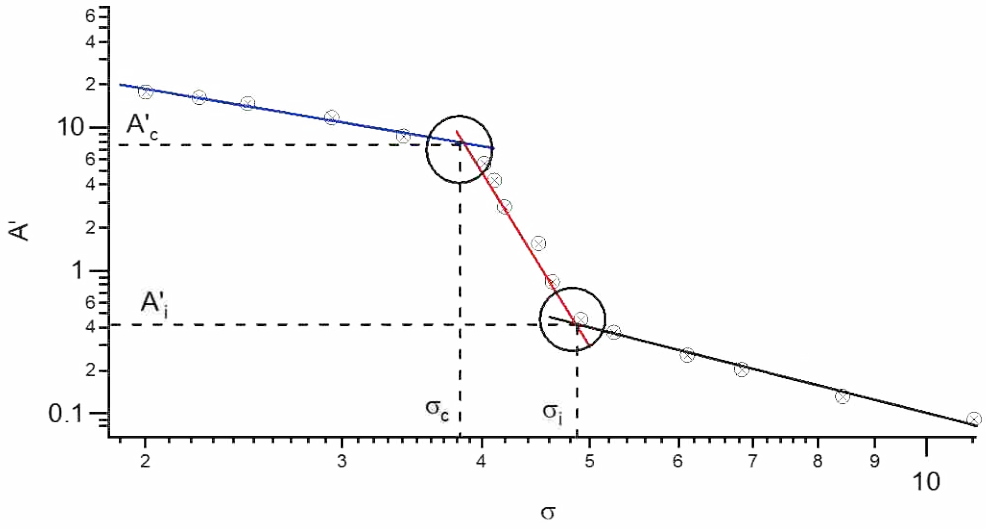

Figure 57: Plot of sigma vs. A' showing the two design limits that have been solved from the example problem in section 4.7

To obtain the A' for the non-cavitating regime equations (6.22)-(6.24) are used where the slope, m, is determined as follows.

$$\epsilon = \left(\frac{d}{D}\right)\left(\frac{t}{d}\right)^{0.4}\left(\frac{A_H}{A_p}\right)^{2.5} = 0.008 \tag{A. 26}$$

$$m^* = 1.2 - 0.72\, exp(-252\varepsilon) - 0.38\, exp(-1840\epsilon) = 1.1 \tag{A. 27}$$

$$\boxed{m = m^*\left(2\, ln\left(\frac{A_H}{A_p}\right) + 0.4\right) = -2.27} \tag{A. 28}$$

An equation can now be developed for A' as a function of σ for the non-cavitating regime (black line in Figure 57) by using the slope, m, and the incipient point solved for above to find the y-intercept, y.

$$y = -ln(A_i^{'}) - m\, ln(\sigma_i) = 3.09 \tag{A. 29}$$

$$\boxed{\ln(A^{'}) = -2.27\ln(\sigma) + 3.09, \qquad \sigma \le \sigma_i} \tag{A. 30}$$

A model of $A_H^{'}$ up to the critical cavitation point has now been developed and can be seen below. In Figure 58 a plot of A' versus σ is shown comparing the actual measured data against the model that was developed.

$$\boxed{\ln(A^{'}) = \begin{cases} -2.27\ln(\sigma) + 3.09, & \sigma \le \sigma_i \\ -9.72\, ln(\sigma) + 15.32, & \sigma_i \le \sigma \le \sigma_c \end{cases}} \tag{A. 31}$$

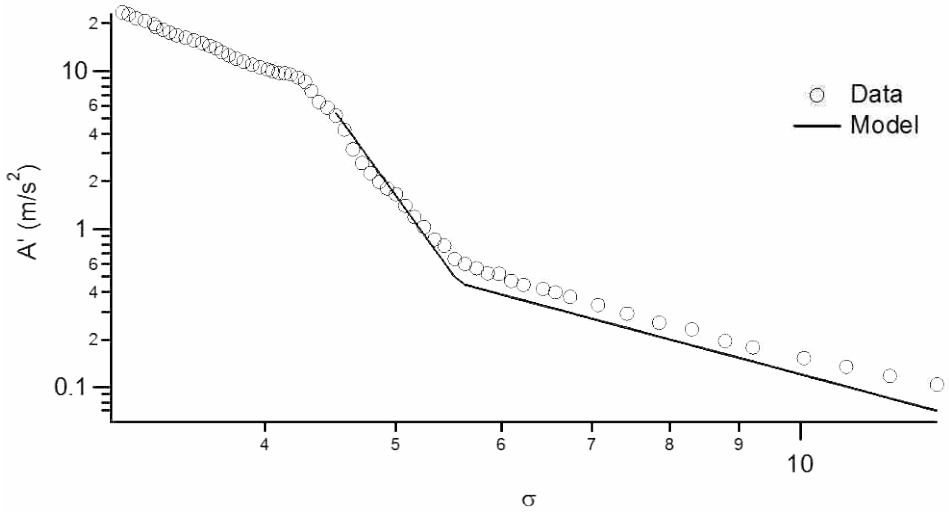

Figure 58: Plot of A' vs. σ comparing experimental results to a model that was developed in equation (A.31) for a baffle plate with d=0.634 t=0.67 and n=112.

APPENDIX B. KEY PARAMETERS FOR ALL BAFFLE PLATES CONSIDERED

Table 4: Key parameters for all baffle plates considered

d (m)	t (m)	# holes (-)	K_{Lp} (-)	σ_i (-)	A'_i (m/s^2)	v_{Hi} (m/s)	σ_c (-)	A'_c (m/s^2)	v_{Hc} (m/s)
2.520	0.660	7	5.23	4.745	0.226	6.875	3.37	8.747	8.835
2.535	0.645	4	33.69	2.74	0.376	5.635	2.25	6.209	6.35
1.267	0.663	28	4.12	5.135	0.376	7.59	3.515	7.617	10.015
1.264	0.660	14	22.53	3.385	0.426	7.185	2.685	3.694	7.91
1.267	0.310	7	180.52	1.04	0.449	8.995	0.955	7.118	9.48
1.267	0.643	7	189.35	1.05	1.143	9.33	0.97	8.732	9.424
0.636	0.648	156	0.39						
0.635	0.665	112	2.22	5.525	0.514	11.165	4.245	7.451	14.12
0.649	0.652	57	13.9	3.1	0.355	9.23	2.315	3.006	10.555
0.634	0.649	28	93.11	2.18	0.429	8.56	1.1	25.454	12.52
0.317	0.511	624	0.45						
0.323	0.513	448	2.24	4.905	0.355	11.84	3.965	5.383	14.725
0.322	0.556	224	13.92	2.77	0.381	10.155	2.09	2.731	11.735
0.315	0.516	112	81.65	2	0.202	9.73	1.35	5.142	11.54
0.158	0.503	1793	2.73	3.71	0.226	13.365	3.335	1.659	15.055
0.159	0.536	896	16.67	1.945	0.145	11.405	1.27	3.838	14.595

APPENDIX C. MATLAB CODE FOR POST PROCESSING

```
clear; close;
clc
clear filename
n = 10; % number of files
%

%
intro = 'F:\g Pipe flow vibration research\Raw Time Series Data With RMS
Coversions\Cavitation\4in40\half_in 10_quarter_thick_baffle\';
%
%
samples = 50000;
time = 1/5000;
%
ii=[1,1,3,3,5,5,7,7,9,9,11,11,13,13,15,15,17,17,19,19,21,21,23,23,25,25,27,27
,29,29,31,31,33,33,35,35,37,37,39,39,41,41,43,43,45,45,47,47,49,49,51,51,53,5
3,55,55,57,57,59,59,61,61];

for i = 1:n
           istring = int2str((i+9));
%               istring = int2str(i/2+19);
%                 istring = int2str((i+14));
%              istring = int2str(i+14);
      istring=int2str(i+24);
         if i==ii(i)
        filename(i).name = strcat(intro,istring,'hz');
         else
             filename(i).name = strcat(intro,istring,'5hz');
         end


    Data = load(filename(i).name);


    filename(i).tyme=Data(:,1);
    filename(i).ua1=Data(:,2);
    filename(i).ua2=Data(:,3);
    filename(i).v1=Data(:,4);
    filename(i).v2=Data(:,5);
    filename(i).disp1=Data(:,6);
    filename(i).disp2=Data(:,7);
    filename(i).flow=Data(:,8);

    filename(i).pup=Data(:,11);
```

```
    filename(i).pdown=Data(:,12);
    filename(i).soundpres=Data(:,13);
    clear Data

%     RMS values

        filename(i).ua1rms=sqrt(mean(filename(i).ua1.^2));
        filename(i).ua2rms=sqrt(mean(filename(i).ua2.^2));

        filename(i).vel1rms1000=sqrt(mean(filename(i).v1.^2))*1000;
        filename(i).vel2rms1000=sqrt(mean(filename(i).v2.^2))*1000;

        filename(i).disp1rms1000=sqrt(mean(filename(i).disp1.^2))*1000;
        filename(i).disp2rms1000=sqrt(mean(filename(i).disp2.^2))*1000;

        filename(i).flowrms = sqrt(mean(filename(i).flow.^2));




        filename(i).puprms = sqrt(mean(filename(i).pup.^2));
        filename(i).pdownrms = sqrt(mean(filename(i).pdown.^2));

        filename(i).soundpresrms = sqrt(mean(filename(i).soundpres.^2));

  i
p=10:19;
end
RMS = zeros(n,17);
for i = 1:n
        RMS(i,1) = p(i);
        RMS(i,2) = filename(i).ua1rms;
        RMS(i,3) = filename(i).ua2rms;
        RMS(i,4) = filename(i).vel1rms1000;
        RMS(i,5) = filename(i).vel2rms1000;
        RMS(i,6) = filename(i).disp1rms1000;
        RMS(i,7) = filename(i).disp2rms1000;
        RMS(i,9) = filename(i).flowrms;

        RMS(i,13) = filename(i).puprms;
        RMS(i,15) = filename(i).pdownrms;
        RMS(i,17) = filename(i).soundpresrms;
end



fil=strcat(intro,'RMS10tests.txt');
save(fil, 'RMS', '-ASCII');
```

APPENDIX D. MATLAB CODE FOR ATTINUATION DATA

```
clear;
clc;
close;
clear filename
n = 13; % number of files
%

%
intro = 'E:\g Pipe flow vibration research\Raw Time Series Data With RMS
Coversions\xovred\4in40\quarter_in_10_baffle\23\';
%
%
samples = 50000;
time = 1/5000;
%
pp=[1,2,3,5,7,10,12,14,16,18,19,21,23,24,25,26,27,28,29,30,31,32,33,34,36,37]
;
for i = 1:n
    istring = int2str(pp((i*2)-1));
    jstring = int2str(pp((i*2)));
    filename(i).name = strcat(intro,'A2_',istring,'_A1_',jstring);


    Data = load(filename(i).name);

    filename(i).tyme=Data(:,1);
    filename(i).ua1=Data(:,2);
    filename(i).ua2=Data(:,3);
    filename(i).v1=Data(:,4);
    filename(i).v2=Data(:,5);
    filename(i).disp1=Data(:,6);
    filename(i).disp2=Data(:,7);
    filename(i).flow=Data(:,8);
    filename(i).p1=Data(:,9);
    filename(i).p1f=Data(:,10);
    filename(i).pup=Data(:,11);
    filename(i).pdown=Data(:,12);
    filename(i).soundpres=Data(:,13);


%    RMS Calculation


     filename(i).ua1rms=sqrt(mean(filename(i).ua1.^2));
```

```
    filename(i).ua2rms=sqrt(mean(filename(i).ua2.^2));

    filename(i).vel1rms1000=sqrt(mean(filename(i).v1.^2))*1000;
    filename(i).vel2rms1000=sqrt(mean(filename(i).v2.^2))*1000;

    filename(i).disp1rms1000=sqrt(mean(filename(i).disp1.^2))*1000;
    filename(i).disp2rms1000=sqrt(mean(filename(i).disp2.^2))*1000;

    filename(i).flowrms = sqrt(mean(filename(i).flow.^2));

    filename(i).p1rms = sqrt(mean(filename(i).p1.^2));



    filename(i).p1frms = sqrt(mean(filename(i).p1f.^2));
    filename(i).puprms = sqrt(mean(filename(i).pup.^2));
    filename(i).pdownrms = sqrt(mean(filename(i).pdown.^2));

    filename(i).soundpresrms = sqrt(mean(filename(i).soundpres.^2));

  i

end
RMS = zeros(n*2,10);
RMS(:,1)= pp.*12./4.026;
for j = 1:n
    i=j*2-1;

        RMS(i:i+1,2) = [filename(j).ua2rms,filename(j).ua1rms]';
        RMS(i:i+1,4) = [filename(j).vel2rms1000,filename(j).vel1rms1000]';
        RMS(i:i+1,5) = [filename(j).disp2rms1000,filename(j).disp1rms1000]';
        RMS(i:i+1,7) = [filename(j).flowrms,filename(j).flowrms]';
        RMS(i:i+1,8) = [filename(j).puprms,filename(j).puprms]';
        RMS(i:i+1,9) = [filename(j).pdownrms,filename(j).pdownrms]';
        RMS(i:i+1,10) = [filename(j).soundpresrms,filename(j).soundpresrms]';

end



fil=strcat(intro,'RMS1212testxx.txt');
save(fil, 'RMS', '-ASCII');

clc
clear
plate='sixteenth_in_43_baffle';
intro = strcat('F:\g Pipe flow vibration research\Raw Time Series Data With
RMS Coversions\xovred\ave_data\',plate,'\');

iii=15

p=[37,46,56,65]
```

```
XD=[11,13,11.25,24+7/8,23+1/2,35,24,24,24+1/2,23+1/4,11+3/4,16+1/4,10,24+1/2,
11+3/4,12+3/8,11+1/4,13,11+7/8,11+1/2,12,12+3/8,11+7/8,12,23+1/2,11+1/2];
xd(1)=XD(1);
for i=1:length(XD)-1
    xd(i+1)=xd(i)+XD(i+1);
end
xd=xd.*2.54./10.16;
d=[2.529,2.535,1.267,1.264,1.267,1.267,0.6358,0.6352,0.649,0.6338,0.3168,0.32
25,0.3223,0.3148,0.1583,0.15925];
N=[7,4,28,14,7,7,156,112,57,28,624,448,224,112,1793,896];
NN=N(iii);
dd=d(iii);
ending = '_m_s_RMS.txt';

n=length(p);
for i = 1:n
    clear c x t y h start
    istring = int2str(p(i));
    filename(i).name = strcat(intro,istring,ending);


    Data = load(filename(i).name);
 xx(:,i)=xd;
 ams1(:,i) = Data(1:end,2);
  flow(:,i)= Data(1:end,3);
 vf(:,i)=flow(:,i)./(pi/4*0.1016^2);
vH(:,i)=flow(:,i)./(pi/4*dd^2/100^2*NN);
 mmm=load(strcat(intro,'dbexp_yo_a1_t1_a2_t2.txt'));

end
Mvf=mean(vf)';
for i=1:n
ams(:,i)=ams1(:,i)./(Mvf(i).^2)*.1016;
end

for j=1:n
yo(j)=mmm(j,1);
aa1(j)=mmm(j,2);
tt1(j)=mmm(j,3);
aa2(j)=mmm(j,4);
tt2(j)=mmm(j,5);

ppp(:,j)=(yo(j)+aa1(j)*exp(-tt1(j)*xx(:,j))+aa2(j)*exp(-
tt2(j)*xx(:,j))./(Mvf(j)^2)*.1016;
sse=sum((ams(1:end,j)-ppp(1:end,j)).^2);
sst=sum((ams(1:end,j)-mean(ams(1:end,j))).^2);
RR(j)=abs(sst-sse)/sst;
Ma(:,j*2-1)=(xx(:,j));
Ma(:,j*2)=(ppp(:,j));
end
Mvf=mean(vf)';
st=0:.001:xx(end,1);
for i=1:n
```

```
    base(:,i)=  (0.0058.*Mvf(i).^2)./(Mvf(i)^2)*.1016;

    yll(:,i)=(yo(i)+aa1(i)*exp(-tt1(i)*st)+aa2(i)*exp(-
tt2(i)*st))./Mvf(i)^2*.1016;
end


for i=1:n
TTT=find(yll(:,i)<=yll(end,1)*1.5);
if yll(end,i)>yll(end,1)*1.5
    AT(i)=66666;
    ttt(i)=6666;
else
AT(i)=st(TTT(1));
ttt(i)=yll(TTT(1),i);
end
end

figure(1)
semilogy(xx,ams,'o')
hold on
semilogy(st,yll)
semilogy(AT,ttt,'p k','MarkerSize',15)
hold off
xlabel('x/D')
ylabel('(A''D)/v_p')
title(plate)
matrix=[AT',ttt', mean(vf)',mean(vH)',RR']
fillle=strcat(intro,'sss2sX_D_Atinuation.txt');
fil=strcat(intro,'Curve_fit.txt');
save(fil, 'Ma', '-ASCII');
save(fillle, 'matrix', '-ASCII');
```